# Finite element modelling of fibre matrix debonding and frictional sliding and their effects on neighbouring fibres

**European Wind Energy Master Thesis**

Eric Thomas Folmar

TU Delft

# Finite element modelling of fibre matrix debonding and frictional sliding and their effects on neighbouring fibres

European Wind Energy Master Thesis

Thesis Report

by

Eric Thomas Folmar

to obtain the degree of Master of Science
at the Delft University of Technology
to be defended publicly on August 13, 2024 at 10:00

*Thesis committee*:

| | |
|---|---|
| Chair: | Dr. Daniël Peeters |
| Supervisors: | Dr. Boyang Chen |
| | Dr. Bent F. Sørensen |
| | Dr. Kristine Munk Jespersen |
| External examiner: | Dr. Torben K. Jacobsen |
| Place: | Technical University of Denmark |
| Project Duration: | November, 2023 - July, 2024 |
| Student number: | 5702119 |

An electronic version of this thesis is available at `http://repository.tudelft.nl/`.

Faculty of Aerospace Engineering · Delft University of Technology

## Abstract

This thesis explores finite element modelling of fibre-matrix debonding and frictional sliding in Abaqus, with particular attention given to their influence on neighbouring fibres. It aims to improve model accuracy through advanced simulations and validation methods. A literature review underscores the need for robust finite element models in predicting composite material behaviour in fatigue. Theoretical equations for validating the finite element model are developed.

Single-fibre and multi-fibre models are utilised, with the former being used primarily for validation and the latter being used to simulate various realistic cases. Results demonstrate successful validation and provide insights into the effects of friction along the debond interface on stress concentrations in neighbouring fibres. Key findings indicate that reducing interfacial friction increases crack tip energy release rates, leading to stress fields that could potentially cause fractures in neighbouring fibres near the debond crack tip.

## Acknowledgements

There are many people who have helped me greatly through my time pursuing the European Wind Energy Master and through the completion of this thesis, from professors to classmates to friends and family. While I cannot mention all of them here, there are several individuals whom I would like to thank specifically for their support. First, my sincere gratitude goes out to my supervising team of Drs. Bent F. Sørensen, Boyang Chen, and Kristine Munk Jespersen. Dr. Sørensen was instrumental in helping me find a topic for my thesis, and his theoretical expertise in composite materials has contributed massively to this present work. Dr. Chen has been extremely accommodating and helpful, joining my team virtually from Delft and helping me navigate the complexities of a dual-degree thesis while also contributing invaluable Finite Element Method experience. Dr. Jespersen was exceedingly helpful in helping me to get acquainted with the DTU Abaqus computing systems, guiding me through countless bugs and integration issues in the process. My additional thanks go out to her for giving me as much useful feedback as possible up until the day she began her maternity leave. Finally, I would like to thank my parents, Dan Folmar and Vicki Mekler, for setting me up for success my entire life and for encouraging me to become the best possible version of myself, both academically and personally. I would not be where I am today without their unwavering support.

# Contents

# List of Figures

# List of Tables

# 1 Introduction

In recent decades, composite materials have become ever more important, especially in the aerospace and wind energy industries. By combining strong fibres with a lightweight matrix, manufacturers are able to create materials and structures that offer high strengths exactly where they are needed at a fraction of the weight of conventional materials such as steel. However, the full potential of composites has yet to be realised.

In addition to achieving high strengths and low densities, composite materials have been shown to have increased fatigue resilience [1]. This capability is of vital importance in both the aviation and wind energy industries, which rely on structures that frequently undergo stress cycles. Unfortunately, fatigue damage progression in composites has proven difficult to accurately model. This lack of understanding limits the extent to which manufacturers can safely exploit the true extent of composites' fatigue resilience, and it makes it harder to develop new composites with further improved fatigue behaviour [1].

This thesis project attempts to improve the body of knowledge concerning fatigue damage progression through modelling the phenomenon at the fibre scale using the Finite Element Method (FEM). Specifically, it attempts to demonstrate the effects of a broken and partially debonded fibre on stress concentrations in neighbouring fibres during a loading/unloading/reloading cycle, with special attention given to the influence of friction along the fibre-matrix interface and the fibre volume fraction.

The model built for this project builds upon many analytic and numerical models that have come before, which will be discussed in the literature review in chapter 2. Next, in chapter 3, the specific research questions to be investigated will be defined. Chapters 4 and 5 will discuss the theoretical methodology and the set up of the model, respectively. In chapter 6, a single-fibre model used for validation purposes will be introduced, and the results from simulating the single-fibre pull-out test will be presented and compared with analytical solutions. Chapter 7 will contain the simulation results from an expanded full multi-fibre model, exploring the behaviour of both the broken fibre and its closest neighbouring fibre through the loading/unloading/reloading cycle for a range of debond zone friction coefficients and fibre volume fractions. Finally, chapter 8 will contain discussion of the results, as well as conclusions and potential areas of interest for future research.

# 2 Literature Review

An extensive literature review has been conducted in order to determine the current state of the art in composite fatigue modelling and, by extension, to identify areas where further research would be beneficial to advance the understanding of composite fatigue damage progression. This literature review will first examine existing analytical and empirical models for composite fatigue damage progression, especially those that account for the role of sticking friction and forward/reverse slip in damage arrest and continuation. Next, it will examine the current state of finite element models concerning composite materials and the techniques used to construct these models, noting the limitations of existing models. Finally, the review will identify the role of this thesis in advancing the current body of knowledge concerning fatigue in composite materials.

## 2.1 Theory and Analytical/Empirical Models

Composite materials are notoriously difficult to model and analyse compared to conventional materials, and researchers have long struggled with the problem of predicting fatigue damage in composites. Vassilopoulos writes, "Unfortunately, although the physics of fatigue are the same, the fatigue behaviour of composite materials is different to that of metallic ones. Fatigue failure of composites is challenging to analyse, as many damage mechanisms interact" [2]. Thus, the majority of models for composite fatigue rely on empirical data rather than an understanding of the micromechanical damage progression mechanisms. Fatigue life diagrams, such as this one from Gamstedt and Talreja [3] shown in Figure 1, which is based an earlier diagram from Talreja [4], can be generated using this empirical data.

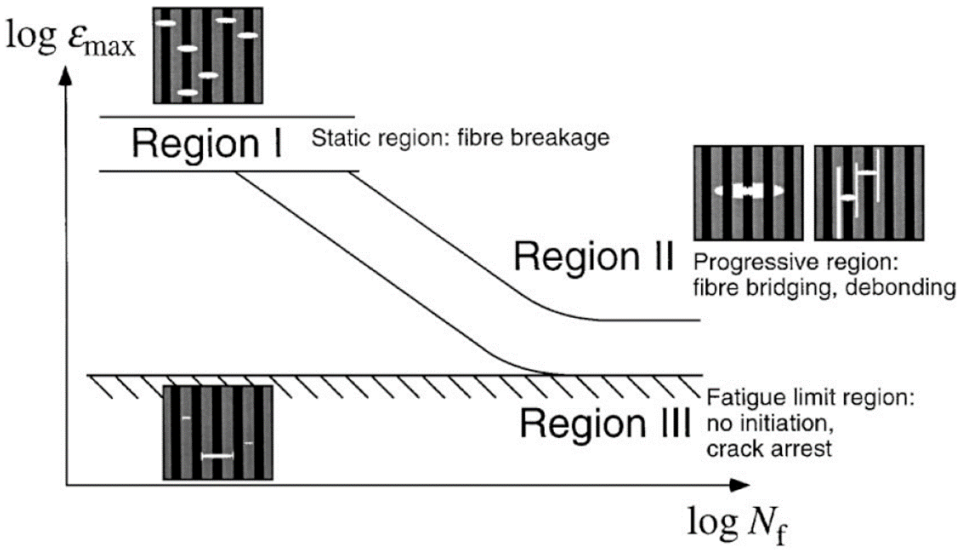


Figure 1: Fatigue Life Diagram of Longitudinal Composites in Tension-Tension Fatigue [3]

As can be seen in Figure 1, in Region II, where peak strain $\varepsilon_{max}$ is sufficient to cause damage progression but low enough so as not to cause rapid non-progressive failure, fatigue damage progresses via matrix cracking and debonding of the fibre from the matrix [3]. Essentially, as the debond length grows at a broken fibre, the stress field in the matrix increases, leading to cracking in nearby fibres and thereby enabling damage progression.

Experimental data from van den Heuvel, Peijs, and Young [5] supports this view. Using Raman spectroscopy, the strain in fibres neighbouring broken and partially debonded fibres was measured. Higher strain values were found at locations near the location of fibre fracture. Specifically, three stress concentrations were observed; one corresponding with the fibre break, and two corresponding with the ends of the debond zone, as is illustrated by Figure 2 [5].

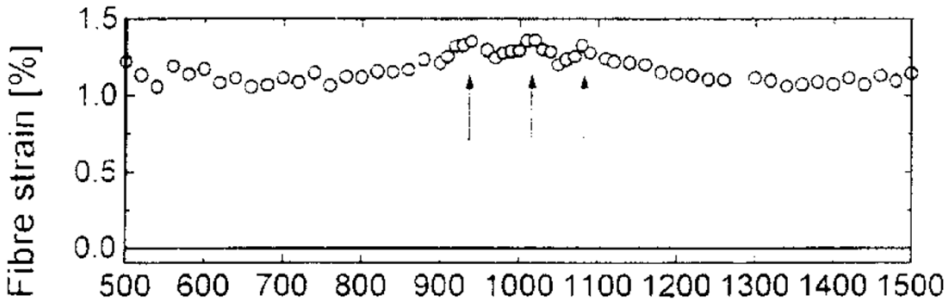


Figure 2: More Detail of the Area Around x = 1000 $\mu$m Showing the Strain Profile of Fibre 4, i.e. a Neighbouring Fibre at an Interfibre Spacing of 1.0$\phi$ [5]

However, in Region III as defined by Figure 1, the debond length does not become long enough to produce the necessary stress field to induce fracture of the neighbouring fibre. Figure 3 from Gamstedt and Talreja [3] shows the debond length as a function of the number of cycles for four different broken fibres under Region 3 loading as found experimentally; as can be seen, the crack growth eventually stops, resulting in an infinite fatigue life.

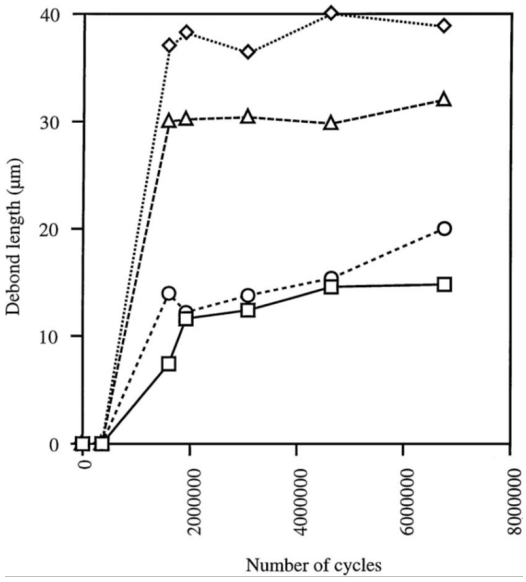


Figure 3: Debond Propagation from a Single Fibre Break in Region III in CF/Epoxy ($\varepsilon$ = 0.89%) [3]

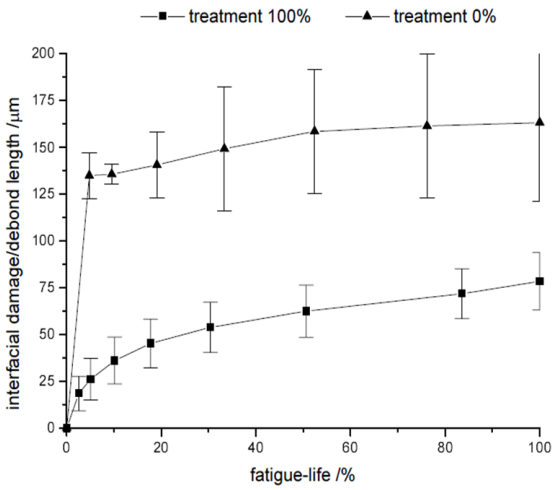


Figure 4: Influence of Fibre-Matrix Adhesion on the Interfacial Damage Zone (Debond Length) in Model Composites Containing Fibres with Two Different Surface Treatment Levels at an Inter-Fibre Spacing of 3 Fibre Diameters ($\sigma_{\max}$ = 80%$\sigma_u$) [6]

Goutianos and Peijs [6] used polarised-light microscopy to measure debond length over time under cyclical loading. In this study, debond zone growth was also found to slow down or halt after a large number of cycles, as can be seen in Figure 4.

More recently, Sørensen and Goutianos [7] have further investigated the existence of a fatigue limit in composite materials by developing a micromechanical model considering the effects of sticking friction. It was found that in the presence of sticking friction in the debond zone, "there will be no change in the crack tip stress intensity factors during cyclic loading. Cyclic crack growth of the debond crack will then stop" [7]. Essentially, fatigue damage progression can halt even after one or more fibre breaks. This finding aligns with the results found by Gamstedt and Talreja as well as Goutianos and Peijs. However, the paper also notes that were the fibre/matrix friction to decrease due to the erosion of asperities during cyclic slipping, it would lead to a lower fatigue limit [7].

As part of their analysis, Sørensen and Goutianos use the following equation to estimate the maximum stress induced in neighbouring fibres as a result of a debond crack tip stress field [7]:

$$\hat{\sigma}_f^K = \sigma_f^K\big|_{\max} = 0.435\frac{E_f}{E_m}\sqrt{\frac{\mathscr{G}_c^i \bar{E}_*}{d^*}}, \tag{1}$$

where $\hat{\sigma}_f^K$ represents the stress in the fibre induced by the stress field, $E_f$ is the Young's modulus of the fibre, $E_m$ is the Young's modulus of the matrix, $\mathscr{G}_c^i$ denotes the interfacial fracture energy, $\bar{E}_*$ is the bimaterial Young's modulus, and $d^*$ is the distance between two adjacent fibres [7].

Sørensen et al. [1] expanded upon this research by investigating in Region II as defined by Figure 1, where fatigue damage does progress. However, this progression can be quite slow, with a large number of cycles in between individual fibre fractures. To explain this behaviour, Sørensen et al. propose a micromechanical model for fatigue damage progression "based on the assumption that the interfacial frictional sliding shear stress decreases during repeated forward/reverse slip" [1] due to the erosion of asperities. "Since the cyclic debond length, $l_d$, depends on the frictional sliding shear stress, $\tau_s$, a decrease in $\tau_s$ leads to an increase in the debond length $l_d$" [1]. When $l_d$ has increased to a sufficient length, the crack tip stress field can cause cause neighbouring fibres to fracture. The micromechanical model for fatigue damage growth rate $\frac{da}{dN}$ developed by Sørensen et al. [1] is described by the following equation:

$$\frac{da}{dN} = \frac{\Delta a^*}{\mathcal{N}^*} = \sqrt{\frac{\sqrt{3}\pi}{2V_f}}\frac{r}{\mathcal{N}^*}\ , \tag{2}$$

where $\mathcal{N}^*$ denotes the average number of cycles needed for the next row of fibres to break, $\Delta a^*$ is the growth distance per failed fibre row, $N$ is the number of applied load cycles, $r$ represents the fibre radius, and $V_f$ is the fibre volume fraction [1].

## 2.2 Visualisation of Fatigue Damage Progression

Jespersen and Mikkelsen [8] used an X-ray CT scanner to monitor the progression of fatigue damage over the course of sustained cyclic loading of a glass fibre composite coupon. Their results allow for the direct observation of the progression of individual fibre fractures in three dimensions; two examples showing this progression are provided in Figure 5. As can be seen in the figure, successive fibre fractures do not always occur in a straight line, suggesting that some of the fractures occur due

to stress concentrations associated with debond crack tips rather than fibre fractures themselves, aligning with the results of van den Heuvel, Peijs, and Young [5].

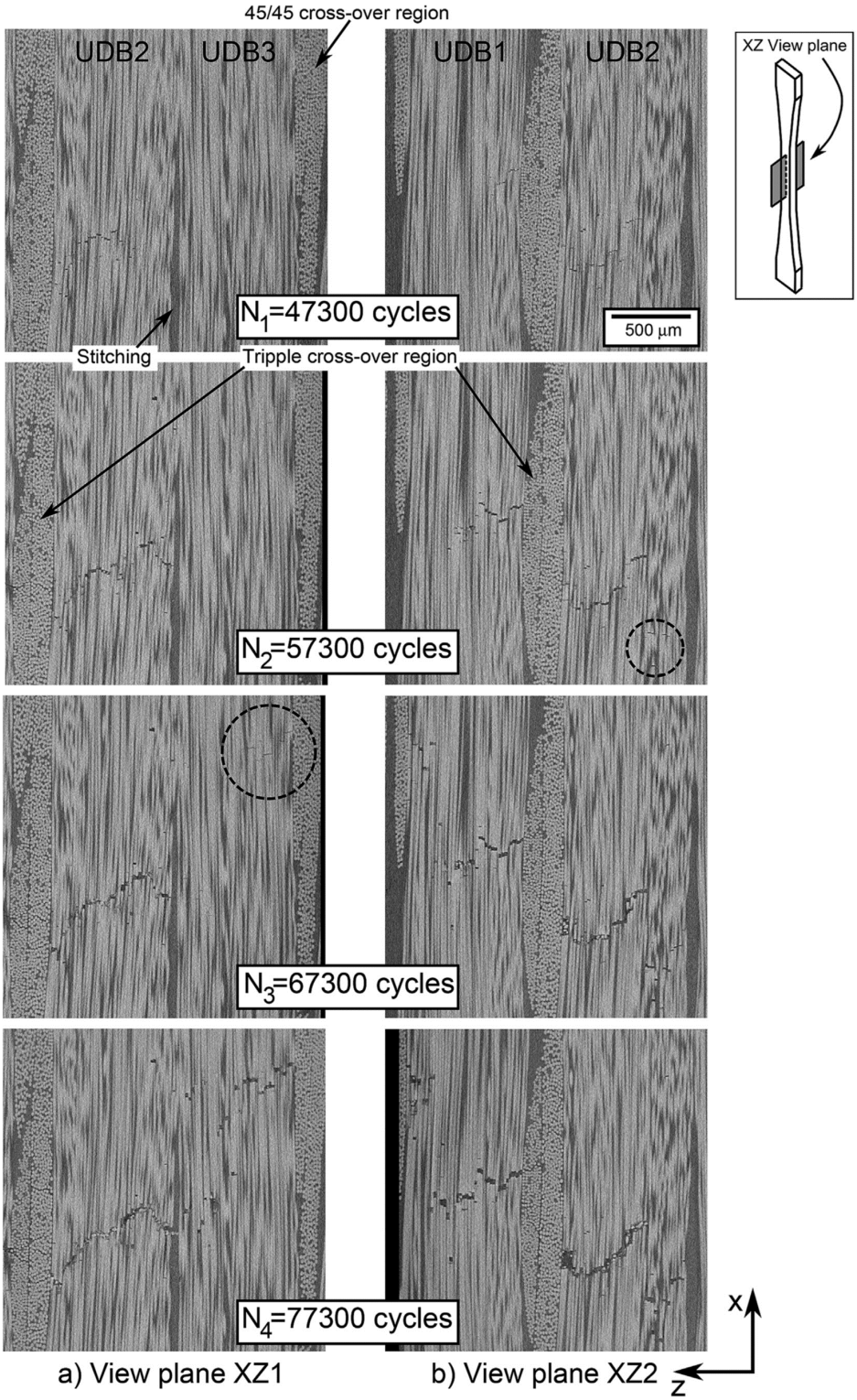


Figure 5: Two Chosen Examples of How the Damage Progresses in the Considered Volume [8]

## 2.3 Finite Element Models

Van den Heuvel et al. [9] created a finite element model to compare with the Raman spectroscopy data of van den Heuvel, Peijs, and Young [5]. The mesh they used is shown below in Figure 6.

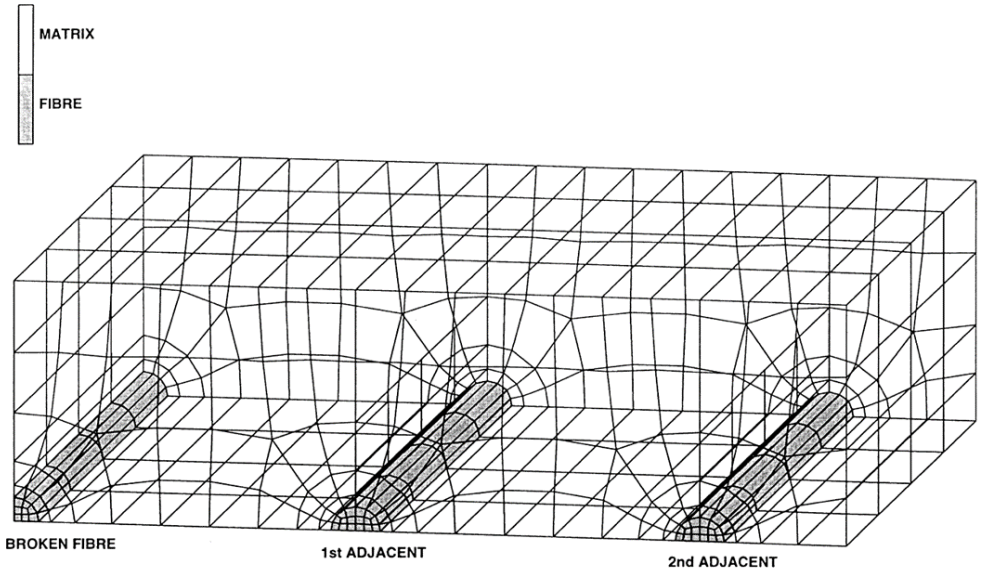


Figure 6: Schematic Representation of the Mesh Used (Not to Scale) [9]

The results from the finite element analysis were found to agree well with the Raman spectroscopy results, as is illustrated in Figure 7, thereby demonstrating the capabilities of FEM to accurately model composite mechanics, specifically stress transfer from a broken fibre to an intact neighbouring fibre.

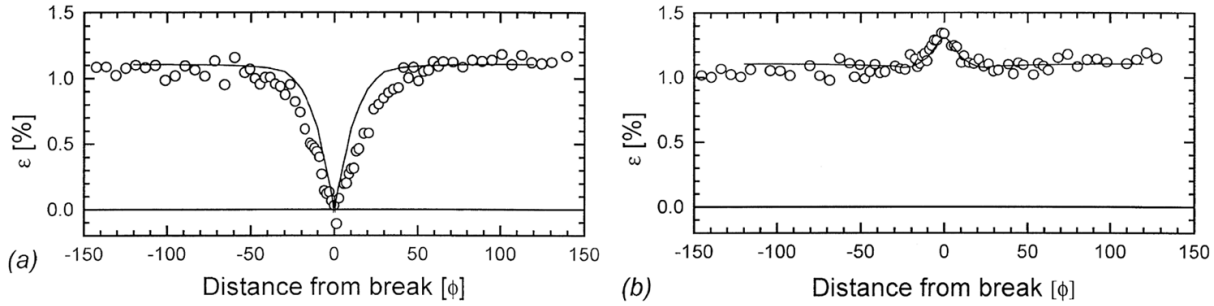


Figure 7: Comparison of FE Calculations to Experimentally Obtained Raman Data for a Carbon/Epoxy Model Composite in the Case of a (100:0) Matrix. (a) Strain Profile of a Broken Fibre and (b) Strain Profile of its Adjacent Fibre Positioned at an Inter-Fibre Spacing of 0.8f [9]

Breite et al. [10] performed a comparative study of six different models for longitudinal tensile failure of unidirectional composites, including a Finite Element - Imposed Stress Model (FEISM). It was found that of the six models, "FEISM is the only model that predicts the maximum stress concentrations in the intact fibres to occur away from the fibre break plane" [10]. This result

suggests that special attention will need to be given in this present work to validating the location of maximum stress concentrations in neighbouring fibres.

Zhuang et al. [11] modelled debond crack growth from a fibre break using hexagonal fibre packing. An interesting technique for defining the boundary conditions of the model was used that was noted to be potentially useful in this present work.

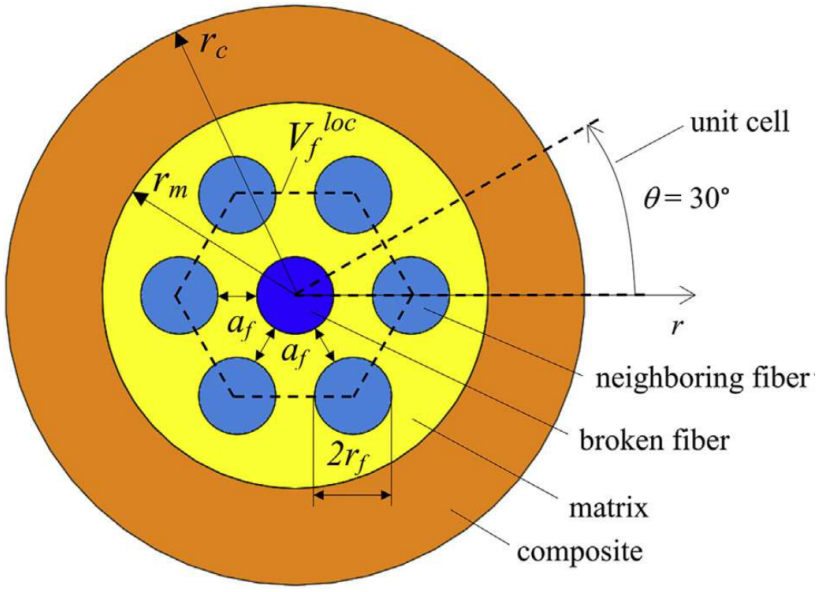


Figure 8: Cross-Section of the Hexagonal Model and Extraction of the Unit Cell [11]

As can be seen in Figure 8, a homogenised composite material was defined in order to create a uniform boundary condition that would simulate the properties of the composite material as a whole far away from the broken fibre. It could be useful to use a similar homogenised material to help impose boundary conditions on the left and right sides of the FEM model for the present work as shown in Figure 12, where true symmetry does not exist. However, this step was ultimately not taken for this project, as it was decided that imposing zero x-displacement would be sufficient.

## 2.4 Role of this Thesis

This project aims to build from the work conducted by Sørensen et al. [1], attempting to simulate the physical mechanisms by which erosion of asperities and reduction of friction can lead to increasing crack tip energy release rates, thereby imposing critical stress concentrations on neighbouring fibres and enabling fatigue damage progression. While models have been created that predict fatigue damage progression, there is still much unknown about the physical mechanics that explain why this damage progression occurs in the way that it does.

Using finite element modelling, this thesis will attempt to produce a model that will be useful not only for the predicting composite behaviour for construction/manufacturing purposes, but also for aiding in the design of new composite materials with improved performance in fatigue.

# 3 Research Questions

The primary research question that this thesis attempts to answer is:

**What is the mechanism by which fatigue damage progresses from fibre to fibre?**

This question can be broken down into several sub-questions. By answering these sub-questions, a better understanding of the answer to the primary question will be achieved. The sub-questions are as follows:

1. **How does debonding of a broken fibre affect the stress field in a neighbouring fibre?**
    a. What is the effect of debond length?
    b. What is the effect of fibre spacing (fibre volume fraction)?
    c. What is the effect of interfacial friction acting along the debonded fibre/matrix interface?
2. **What is the criterion for failure of a neighbouring fibre?**
    a. Why do successive fibre breaks often occur in different planes?
    b. What accounts for the large number of cycles in between successive fibre failures?
3. **How does the mechanism of friction reduction through asperity erosion affect the debond length?**
    a. What is the effect of reduction of interfacial friction on the debond crack tip stress field of the broken fibre during loading, unloading, and reloading?
    b. How does the debond length change with changes in interfacial friction?
    c. How does sticking friction lead to debond crack growth arrest?

These questions served as a guide to the progression of this thesis project, and their answers are discussed in Chapter 8.

# 4 Theoretical Content

This project relies heavily on the Finite Element Method (FEM), which is a numerical means by which to solve a physical system by breaking it down into small, discrete elements via creation of a mesh. Each element has its own associated system of equations and boundary conditions; all of these equations are consolidated into a global system of equations that is numerically solved to resolve the system and determine values of interest such as stresses, strains, deformations, and more. As FEM is extremely widely used and well known, its operating principles will not be discussed further. The software tool that will be used for this research is Abaqus, which is a popular finite element analysis software suite.

In order to accurately model fibre-matrix debonding, especially when determining the stress conditions associated with a given debond length, fracture mechanics theories must be employed. Budiansky, Hutchinson, and Evans [12] developed a model for debonding in composite materials that uses an energy balance to determine crack growth based on the potential energy loss associated with the crack opening. Their equation for determining potential energy loss, shown below, could provide a useful framework for including the effects of friction on the debond length, since it includes a term $\xi_F$ for frictional energy dissipation, which cancels out when equating the potential energy loss with the total crack growth energy dissipation.

$$\pi_1 - \pi_2 = \frac{1}{2}\int_V (\sigma_1 - \sigma_2) : (\varepsilon_1 - \varepsilon_2)\,\mathrm{d}V + \xi_F \tag{3}$$

In Equation 3, $\pi_1$ and $\pi_2$ are the potential energies of the system states before and after crack growth. $\sigma_1$ and $\sigma_2$ are the stress tensors, and $\varepsilon_1$ and $\varepsilon_2$ are the strain tensors for these states. $V$ is the volume of the body, and $\xi_F$ is the frictional energy dissipation.

Alternatively, the Virtual Crack Closure Technique (VCCT) could be employed to effectively calculate the crack tip energy release rate while including the effects of friction in the finite element simulation. VCCT is a method to calculate the strain energy release rate of a crack or a delamination based on the forces and displacements obtained from a finite element analysis, based on the assumption that the energy released by a small crack extension is equal to the energy required to close the crack behind the crack tip [13]. This method is a popular choice for fracture analysis of composite materials and structures. Figure 9 shows a schematic representation of VCCT as applied to a two-dimensional mesh [13].

The VCCT, otherwise known as the Modified Crack Closure Method, is built upon the Two-Step Crack Closure Method, with the added assumption that "a crack extension of $\Delta a$ from $a + \Delta a$ (node $i$) to $a + 2\Delta a$ (node $k$) does not significantly alter the state at the crack tip" as shown in Figure 9 [13]. However, this assumption is not valid when including the effects of friction along the debond interface. Therefore, to accurately model the debond crack, the Two-Step Crack Closure Method must be used. Unfortunately, although the VCCT is built into Abaqus, the Two-Step Crack Closure Method is not, which means that implementing it would require extensive Python scripting that was deemed too complex for this Master's thesis. While the Two-Step Crack Closure Method would arguably produce the most accurate results and certainly merits consideration for future use in the context of fibre-matrix debonding, a more straightforward method was chosen for use in this project.

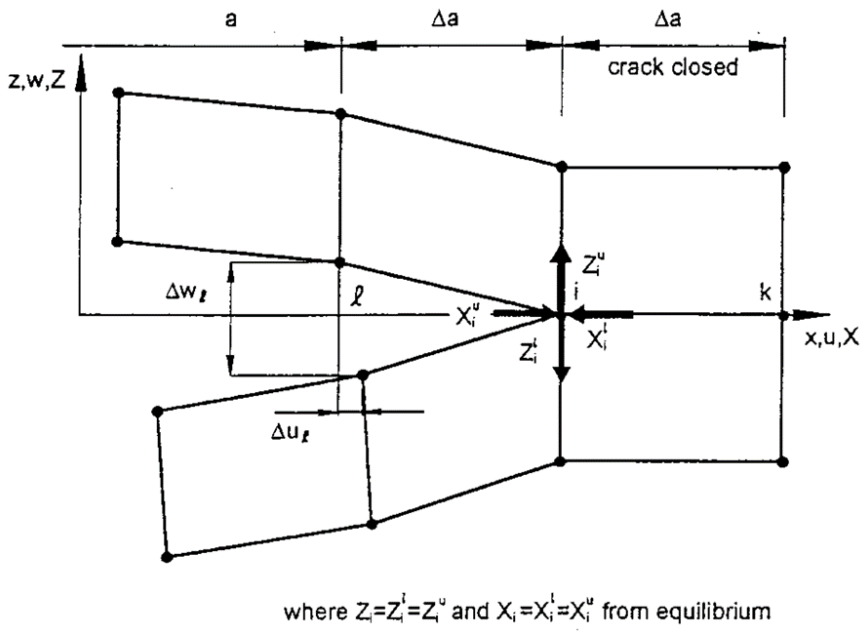


Figure 9: Modified Crack Closure Method (One-Step VCCT) [13]

Instead of using the VCCT, it was decided to calculate the crack tip energy release rate via the J-integral, which is a fundamental concept in fracture mechanics and was first formulated by J. R. Rice in 1968 [14]. Calculation of the J-integral involves integrating along a contour $\Gamma$ that begins on one side of a crack and ends on the other, as is shown in Figure 10, to determine the crack tip energy release rate $G$. In theory, the J-integral is path-independent, meaning that its value will be the same for any $\Gamma$ chosen. However, when including the effects of friction along the crack faces, the J-integral value will increase with the length of the frictional interface that is included in $\Gamma$. However, if this length is held constant, the J-integral provides useful results for comparing between various simulation cases. Therefore, J-integral results are used for $G$ values in this thesis, and the variation of the J-integral values with respect to the length of the frictional interface included in $\Gamma$ is plotted and discussed in section 6.4.

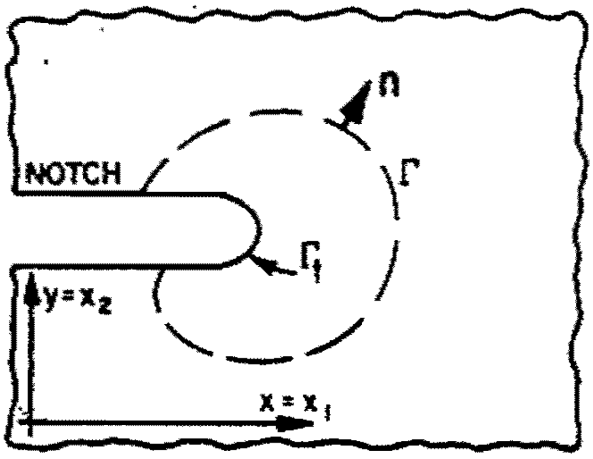


Figure 10: Flat Surfaced Notch in Two-Dimensional Deformation Field (All Stresses Depend Only on x and y). $\Gamma$ Is Any Curve Surrounding the Notch Tip; $\Gamma_t$ Denotes the Curved Notch Tip [14]

The equation for the J-integral is given as Equation 4, with its key components explained below [14].

$$J = \int_{\Gamma} \left( W dy - \mathbf{T} \cdot \frac{\partial \mathbf{u}}{\partial x} ds \right) \tag{4}$$

- $\Gamma$ : Any contour around the crack tip.
- $W$ : The strain energy density, given by the integral of the stress tensor components with respect to the strain tensor components.
- $\mathbf{T}$ : The traction vector on the contour $\Gamma$, representing the internal forces acting on the contour.
- $u$ : The displacement vector.
- $ds$ : A differential element along the contour $\Gamma$.

## 4.1 Equations for Analytic Validation of Abaqus Model

An important step in this project is the analytic validation of the FEM model, which is discussed in section 6.2. For this validation, analytical solutions for single-fibre pull-out derived from Hutchinson and Jensen's models will be used [15]. The equations for S22 in the fibre upstream of the crack tip, S22 in the fibre in the slip zone, and crack tip energy release rate as a function of applied load are introduced here as Equations 5, 6, and 7, respectively [15].

In this section, the following nomenclature will be used:

- $\sigma_f^+$: Fibre stress far upstream of the crack tip.
- $\sigma_f^-$: Downstream fibre stress in the full slip zone.
- $E_f$: Young's modulus of the fibre.
- $E_m$: Young's modulus of the matrix.
- $E_c$: Effective Young's modulus of the entire composite.
- $x^*$: Position in the full slip zone.
- $\bar{\sigma}_c^M$: Applied macroscopic stress in the composite.
- $\bar{\sigma}_f$: Applied stress in the downstream fibre free end.
- $\tau_s$: Shear stress at the fibre-matrix interface.
- $\Delta\varepsilon^T$: Thermal strain difference between the fibre and matrix due to temperature change.
- $G_{IIc}^i$: Mode II energy release rate at the crack tip.
- $V_f$: Fibre volume fraction.
- $r$: Radius of the fibre.
- $l_d$: Fibre-matrix interface debond length.

The analytic solution for the constant fibre stress far upstream of the crack tip is given by Equation 5:

$$\sigma_f^+ = \frac{E_f}{E_c}\left\{-\Delta\varepsilon^T \cdot (1 - V_f)\, E_m + \bar{\sigma}_c^M\right\} \tag{5}$$

The analytic solution for the fibre stress in the slip zone as a function of the distance from the fibre fracture location is given by Equation 6:

$$\sigma_f^- (x^*) = \bar{\sigma}_f - 2 \cdot \tau_s \cdot \frac{x^*}{r} \tag{6}$$

The analytic solution for the energy release rate at the crack tip during full slip as a function of the applied stress to the broken end of the fibre is given by Equation 7:

$$G_{IIc}^i (\bar{\sigma}_f) = E_f \cdot r \cdot \frac{E_c}{(1 - V_f)\, E_m}\left[\frac{1}{2} \cdot \frac{(1 - V_f)\, E_m}{E_c}\left\{\frac{\bar{\sigma}_f}{E_f} + \Delta\varepsilon^T\right\} - \frac{\tau_s}{E_f}\frac{l_d}{r}\right]^2 \tag{7}$$

# 5 Methodology and Model Definition

The experimentation in this project was conducted via FEM models built in Abaqus and run on the DTU Wind Energy Abaqus cluster, which operates on Linux/SLURM. Abaqus is a high-fidelity finite element solver which has already proven its reliability through extensive employment in both academia and industry, and it has the capability to simulate the phenomena that were investigated in this project, including frictional sliding along the fibre-matrix interface, fibre-to-fibre stress transfer, and crack tip energy release.

## 5.1 Single-Fibre Model

Before construction of the full multi-fibre model, a simpler model including only one fibre was constructed in order to validate the Abaqus results against analytic solutions for single-fibre pull out, to perform a mesh convergence study, to determine the necessary distance upstream of the crack tip such that end effects would not influence the crack behaviour, and to establish a uniform building block for use in construction of the larger model. Furthermore, this model already provides interesting results that illustrate the progression of frictional sticking and sliding under a gradually increasing load. A 3D visualisation of the single-fibre model is shown in Figure 11.

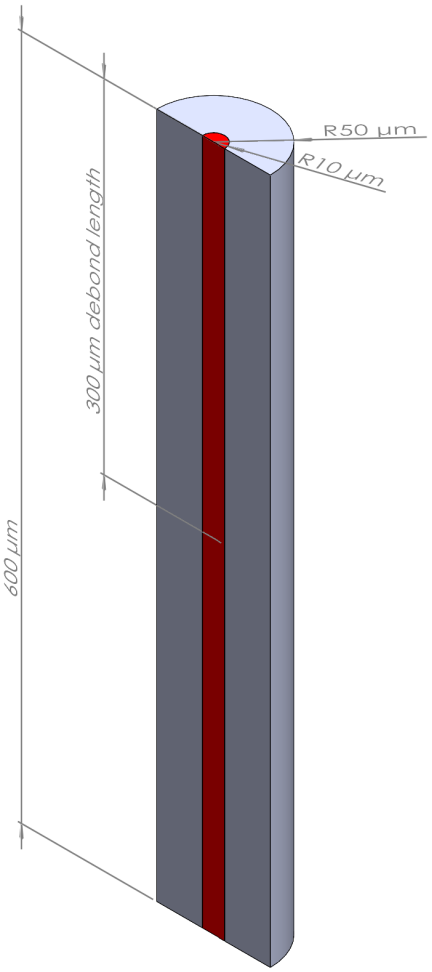


Figure 11: 3D Representation of Single-Fibre Model

The model consists of a debond cylinder, comprising a halfway-debonded fibre of radius 10 $\mu$m surrounded by a 1 $\mu$m thick layer of matrix, and a 39 $\mu$m thick layer of matrix that surrounds the debond cylinder and is tied to the matrix in the debond cylinder. By constructing the model in such a manner, it is possible to reuse the debond cylinder in the multi-fibre models for fibre volume fractions of up to 70%.

## 5.2 Multi-Fibre Model

The model was then expanded to include neighbouring fibres so that the effects on those fibres of the stress field propagating from the broken fibre could be investigated. This model could be modified to simulate varying coefficients of friction along the debonded fibre-matrix interface, varying fibre volume fractions, and varying debond lengths, although the effects of changing the debond length were not investigated during this project.

A sketch of how the model fits into the context of a composite specimen undergoing progressive fatigue damage has been created in SOLIDWORKS and is shown below in Figure 12. Figure 13 shows a three-dimensional depiction of the finite element model. In both figures, the red cylinders represent broken, partially debonded fibres, and the green cylinders represent intact fibres. Note that for increased clarity, Figures 12 and 13 correspond to a much lower volume fraction than the cases that were actually simulated. Furthermore, the Abaqus models extend much farther along the y-axis than what is shown in Figure 13.

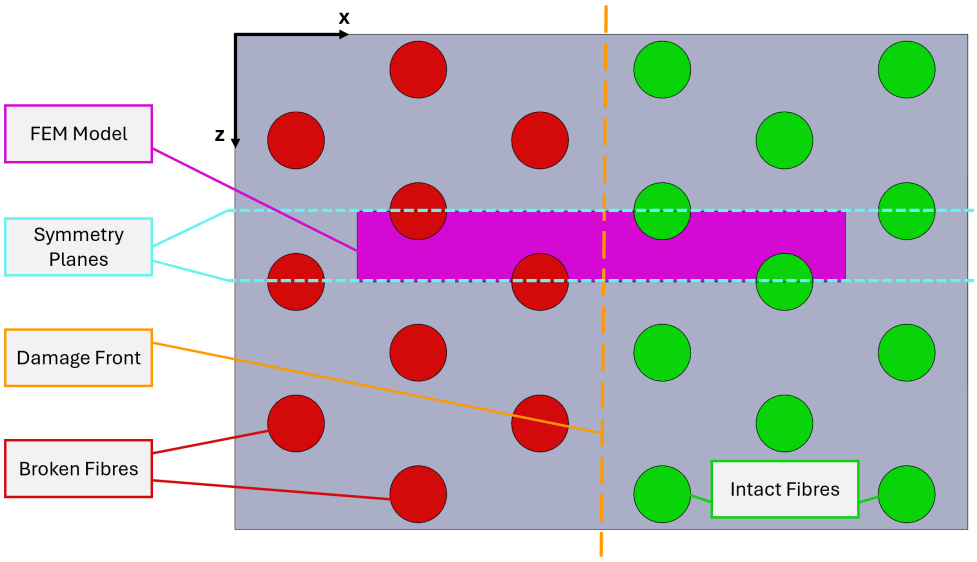


Figure 12: Sketch of Finite Element Model in Context (Not to Scale)

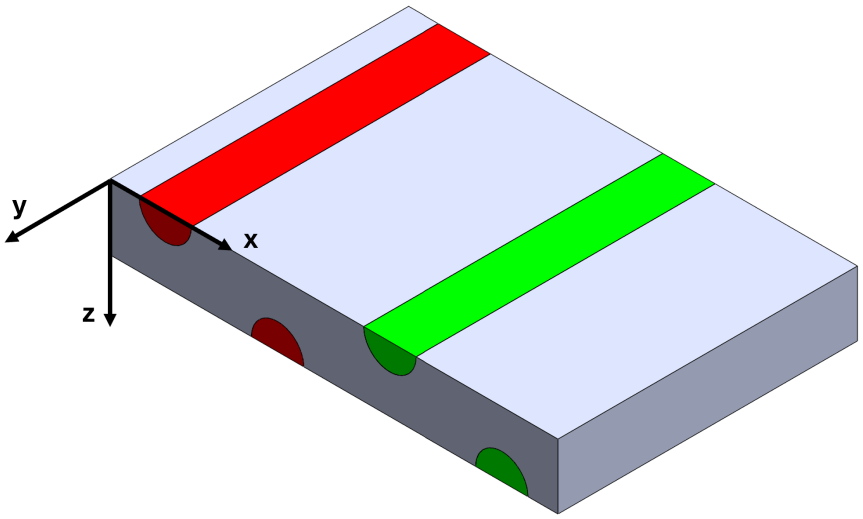


Figure 13: 3D Representation of Finite Element Model (Not to Scale)

The top and bottom faces of the model, as oriented in Figure 12, are true symmetry planes, and they were defined as such in the FEM model by imposing zero-displacement boundary conditions in the z-direction, which corresponds to the vertical axis in Figure 12. The left and right faces of the model are not true symmetry planes, as the model is not symmetric in the x-direction (the horizontal axis in Figure 12) due to the broken fibres on the left side of the model. Nonetheless, it was decided to impose zero displacement-boundary conditions in the x-direction to these faces, as this condition is more representative of the FEM model's constrained position within the larger composite specimen surrounding it. These faces can be thought of as local symmetry planes, and were the model to be expanded in the x-direction with the inclusion of more fibres, the left and right faces would increasingly approach true symmetry.

The front of the model as oriented in Figure 12 is defined as the fracture plane of the broken fibres. Therefore, a zero-displacement boundary condition in the y-direction was applied only to the matrix and the intact fibres, with the broken fibre ends left unconstrained. Loading was then uniformly applied to the opposite face of the model in the form of a 15 $\mu$m y-displacement boundary condition. The location of this loading face had to be far enough away from the debond crack tip so as to allow for the stress in the fibre to reach steady state upstream of the crack tip. Through analytic estimation of the fibre-to-matrix load transfer length followed by testing of many iterations of the single-fibre model, it was determined that a 600 $\mu$m model with a debond crack extending 300 $\mu$m (with the remaining 300 $\mu$m left bonded) would be sufficient to satisfy this requirement.

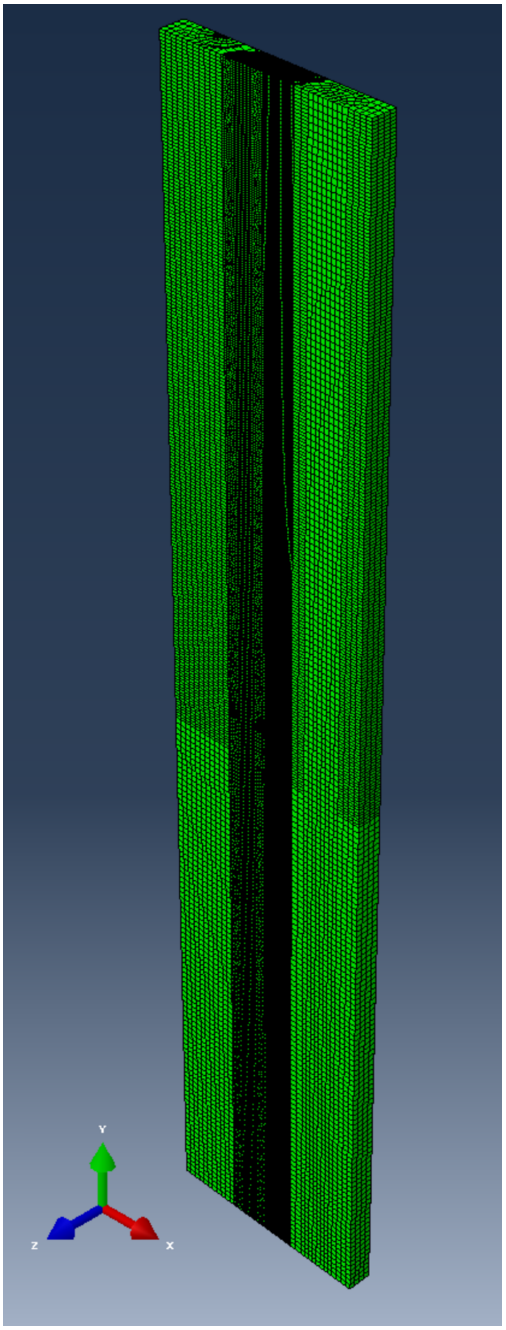


Figure 14: Multi-Fibre Model Mesh, Full Model View

## 5.3 Material Properties and Thermal Loading

A coefficient of friction was defined along the debonded fibre-matrix interface that could be varied across different simulations. In order to provide a normal force to allow for a frictional shear force, a thermal expansion coefficient of $6 \times 10^{-6}$ m/(m°C), which is typical for glass fibres, was defined in the model's fibre material properties, and a temperature increase of 500° C was applied to the entire model before the first loading step. Thus, the fibres were pressing against the matrix for the duration of the loading cycle, allowing for frictional forces.

It is important to note that the thermal conditions applied to this model do not match the conditions seen in actual composite manufacturing. In reality, the fibre and matrix would both cool down from the as-cured temperature and shrink during the cooling stage of the manufacturing process, with the matrix shrinking more than the fibre and thereby creating a normal force. However, attempting to replicate these conditions in Abaqus for the single-fibre model led to poor results that did not effectively highlight the role of friction. Therefore, it was decided to simplify the thermal loading by imposing expansion on the fibre via an exaggerated temperature increase and leaving the matrix material without any thermal expansion properties, allowing for increased control of the normal force on the debond interface and simplifying the thermal loading simulation step. For consistency, the thermal loading simulation parameters were kept the same when transitioning from the single-fibre model to the multi-fibre

model. The decisions made regarding the thermal loading step will be important to recall in the discussion of the results, which is found in Chapter 8.

Another simplification that was made when setting up the model was the decision not to include Poisson effects in either of the materials. Using a Poisson's ratio of zero decreases the complexity of the simulation loading step calculations while also making the comparison with analytical solutions easier.

Young's modulus for the matrix was defined as 3.1 GPa, and Young's modulus for the fibre was defined as 82 GPa.

## 5.4 Mesh Construction

Figure 14 shows the mesh that was used for the full multi-fibre model, which was constructed based on the single-fibre mesh convergence study discussed in section 6.1. As can be seen in Figure 14, the refinement of the mesh in the y-direction is increased over and slightly past the debond length, and the two middle fibres and the matrix between them also have a finer mesh than the outer fibres and surrounding matrix. The finer mesh close to the two central fibres can be more clearly seen in Figure 15, which shows the mesh from a top-down view.

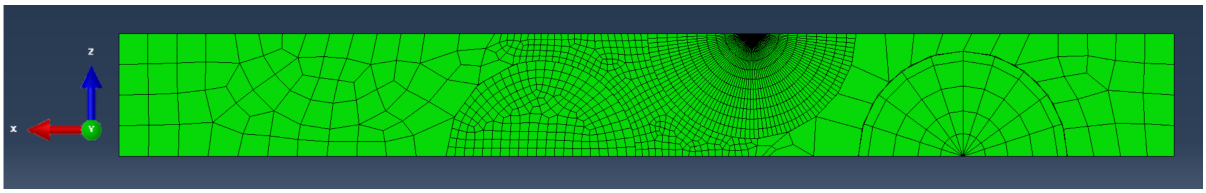


Figure 15: Multi-Fibre Model Mesh, Top View

Special care was taken in building the mesh surrounding the debond crack tip, since this region had to be optimised for calculation of the J-integral. Essentially, a circular tube of mesh had to be created, following the crack tip around the circumference of the fibre, as is illustrated in Figure 16. This tube was created through careful cell sectioning and mesh seeding in Abaqus, and the end of the tube along the front face of the model is shown in Figure 17.

As can be seen in Figure 17, the mesh surrounding the crack tip is by far the finest mesh of the model, and it allows for accurate calculation of the J-integral along 14 roughly circular contours. The mesh in the debond cylinder was left essentially unchanged from the single-fibre model to the multi-fibre model, with only negligible differences in the mesh generation process.

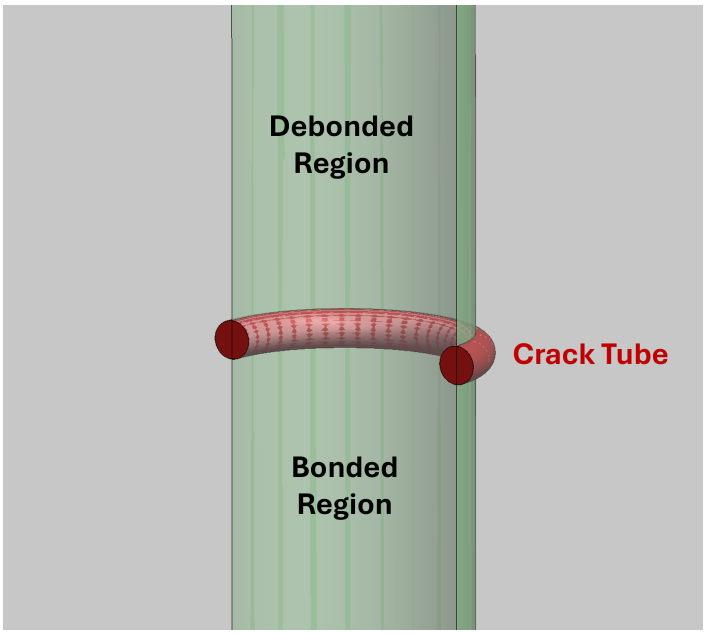


Figure 16: Illustration of the "Crack Tube" in the Context of a Fibre Surrounded by Matrix (Not to Scale)

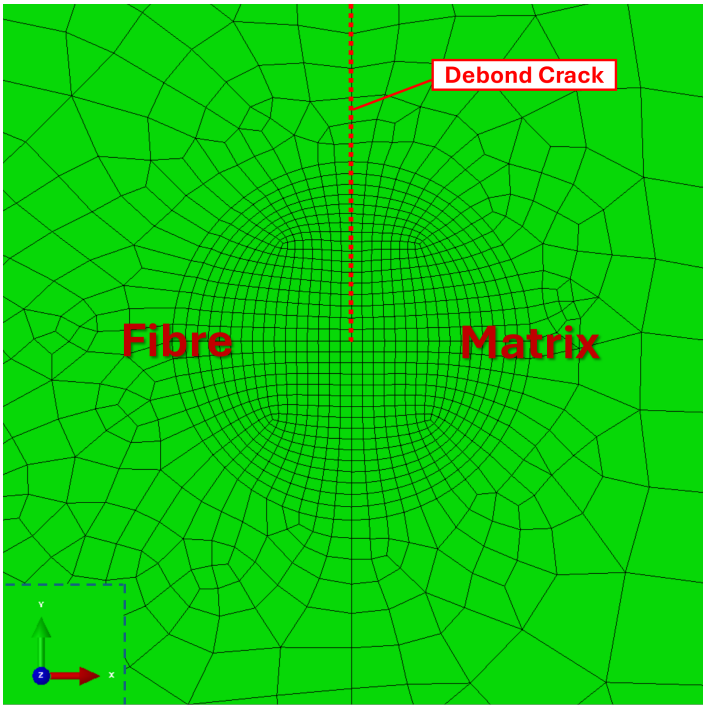


Figure 17: Debond Cylinder Model Mesh at Debond Crack Tip

## 5.5 Simulation Steps

Imposed displacement of the model occurred over three simulation steps to simulate the loading and unloading of a fatigue cycle. In the first step, the bottom face of the model was pulled 15 $\mu$m. In the second step, the bottom face was returned to its original position, and in the third step, the bottom face was again displaced 15 $\mu$m. Each step occurred over a minimum of 20 increments, allowing for the visualisation of the specimen's behaviour over time. In some cases where Abaqus could not solve an increment, increment size was temporarily reduced, resulting in some steps that took 23 increments to simulate.

It should be noted that loading the model via imposed displacement instead of force has the drawback of applying a slight compressive force to the model at the end of the unloading step, which is supposed to be free from external loading. This applied compression is discussed further at the end of section 7.1. However, this drawback was ultimately deemed negligible to the overall behaviour of the model and the desired results of the simulations.

# 6 Single-Fibre Model Results

This chapter begins with section 6.1, in which the testing to determine mesh convergence is presented, with four increasingly finer meshes being tested. In section 6.2, the results from the single-fibre Abaqus model are compared with the analytic solutions for the stress in the partially debonded fibre as a function of position along the fibre and for the energy release rate at the crack tip as a function of applied force. Next, in section 6.3, the axisymmetry of the single-fibre model is confirmed. Finally, in section 6.5, the behaviour of the single-fibre model under incremental loading will be further explored. The coefficient of friction along the fibre-matrix interface in the debond zone used for the single-fibre model is 0.50.

Note that while the full multi-fibre simulations were run over loading, unloading, and reloading steps, the single-fibre model was only run over a single loading step of 20 increments, as the initial loading step is most relevant when comparing with the analytic single-fibre pull-out solution. Further, a single loading step was sufficient for testing mesh convergence.

Figure 18 shows a cross-sectional view of the single-fibre model that was used for this portion of the analysis. This sketch provides useful context for the path plots that are to follow in this chapter and in chapter 7. Note that the path plots are plotted with respect to absolute distance, not position; the model's positive y-direction is actually defined as to the left in the context of Figure 18.

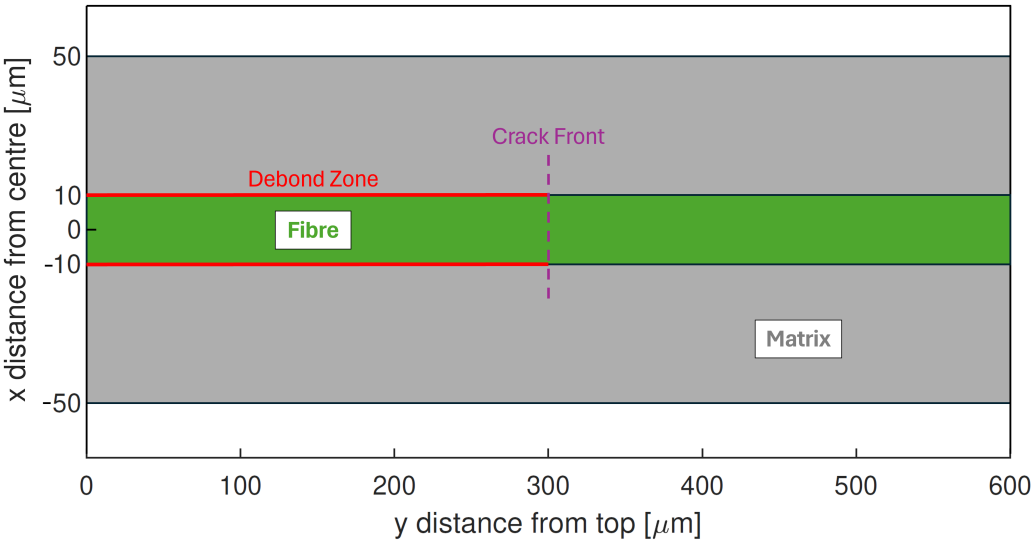


Figure 18: Cross Section of Single-Fibre Model

## 6.1 Mesh Convergence Study

Single-fibre simulations were carried out using four levels of mesh refinement in order to test for mesh convergence, with each mesh containing roughly eight times as many elements as the last, as the characteristic element length was roughly halved with each successive mesh. Path plots for CSHEAR2 and S22 (Figures 19 and 20), as well as a plot of energy release rate with respect to loading (Figure 21), were used to compare the results for the various meshes.

It should be noted that a slight error in the application of the thermal condition to the fibre was discovered following completion of the mesh convergence study. The temperature increase of 500° C was not applied to the one-element-thick (in the y-direction) segment of the debonded section of the fibre nearest to the debond crack tip. This error was corrected for all subsequent simulations, but it was decided not to redo the mesh convergence simulations, as each simulation is computationally expensive, and the error was deemed to be unlikely to affect mesh convergence.

For Figures 19 and 20, the plotted loading increment for each mesh type was chosen so that the fibre pulling forces for the four cases were as close to each other as possible. The loading conditions for the four mesh types tested are given in Table 1.

Table 1: Loading at Plotted Increment for Different Mesh Types

| **Mesh Type** | **Loading (N)** |
|---|---|
| Coarse | $6.92 \times 10^{-2}$ |
| Medium | $7.21 \times 10^{-2}$ |
| Fine | $7.31 \times 10^{-2}$ |
| Extra Fine | $7.30 \times 10^{-2}$ |

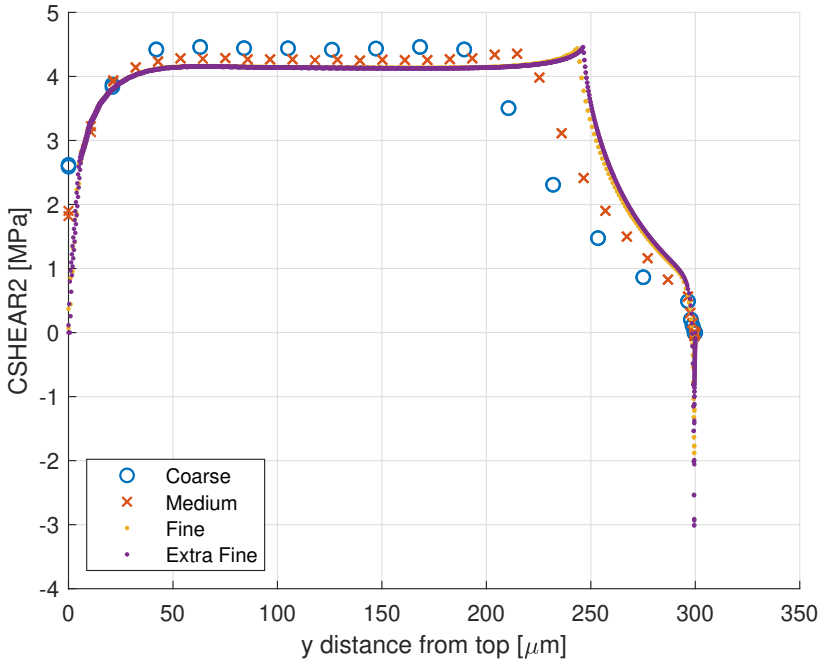


Figure 19: CSHEAR2, Mesh Convergence Study

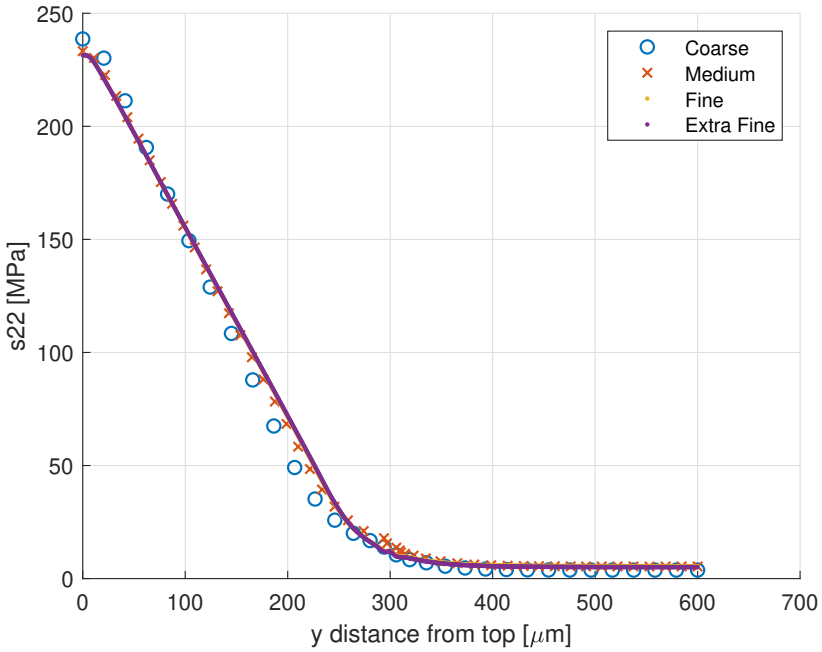


Figure 20: S22 Through Centre Path, Mesh Convergence Study

As can be seen in Figures 19 and 20, the Fine and Extra Fine meshes produce nearly identical results for CHSEAR2 and S22, suggesting convergence of the Fine mesh. The level of mesh refinement is also important for path plot resolution, in addition to accuracy. As can be seen most clearly in Figure 19, the Coarse and Medium meshes do not allow for sufficient resolution so as to properly view the intricacies of the path plots. The resolution of the Fine mesh, however, appears to be sufficient, as it is just as capable as the Extra Fine mesh when it comes to showing the shape of the CSHEAR2 curve.

For Figure 21, since the J-integral is not path-independent when including friction along the fibre-matrix interface, it was important to match the contour distances used for each of the mesh types. The contour distances used for the plotted J-Integral results for the four mesh types are given in Table 2. Here, the contour distance is defined as the distance from the crack tip to the point where the J-Integral contour intersects with the debonded fibre-matrix interface.

Table 2: Contour Distances Used for G Results for Different Mesh Types

| **Mesh Type** | **Contour Distance ($\mu$m)** |
|---|---|
| Coarse | 0.23599 |
| Medium | 0.23639 |
| Fine | 0.22104 |
| Extra Fine | 0.22852 |

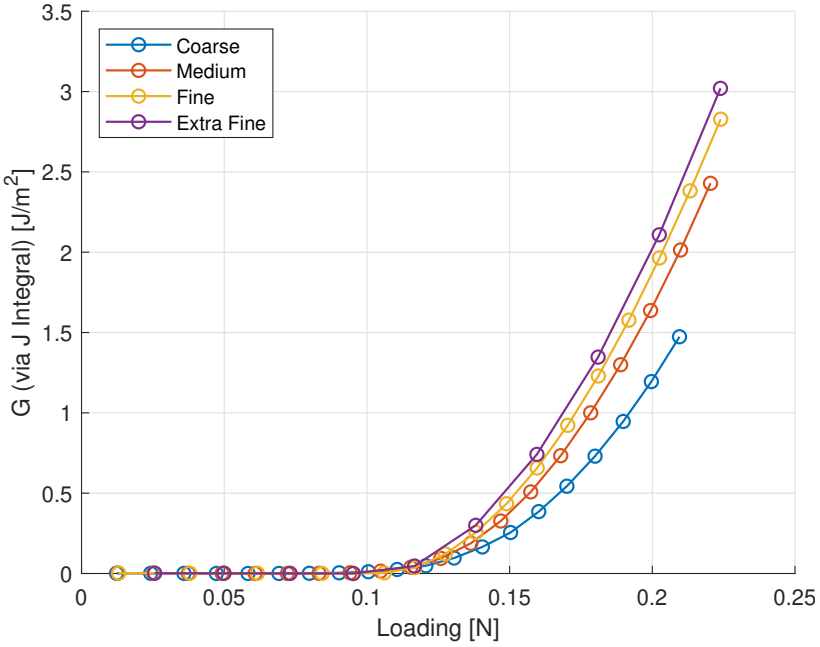


Figure 21: Energy Release Rate vs. Loading, Mesh Convergence Study

Figure 21 shows that although the Fine and Extra Fine meshes do not produce identical results, the difference between the curves decreases with each successive level of mesh refinement, suggesting that the mesh is converging. In any case, the Extra Fine mesh simulation was too computationally expensive to run on the Abaqus cluster, which meant that it had to be run on the more powerful DTU Sophia cluster, which requires more steps to run and post process simulations and which often has lengthy queues for job submissions. Furthermore, the clock time spent on each increment was significantly increased, so the simulation was run with ten rather than 20 loading increments.

Based on the results of the mesh convergence study and the computational expense involved in refining the mesh any further, the Fine mesh was chosen for use throughout the remainder of this project.

## 6.2 Validation of FEM Model with Analytical Solutions

In addition to ensuring mesh convergence, the single-fibre model was validated by comparing its results to analytical solutions for single-fibre pull-out derived from Hutchinson and Jensen's models [15], which are introduced in section 4.1. Specifically, results for S22 in the fibre along its length and crack tip energy release rate as a function of applied load were compared to their analytic solutions.

Figures 22, 23, and 24 show the Abaqus results for S22 in the fibre at loading increments 1, 9, and 20, respectively, overlaid with the analytic solutions for $\sigma_f^+$ and $\sigma_f^-$. In each case, S22 is plotted along the path through the centre of the fibre and along another path close to the outer surface of the fibre. Similar plots containing data for all of the loading increments are included in Appendix A.

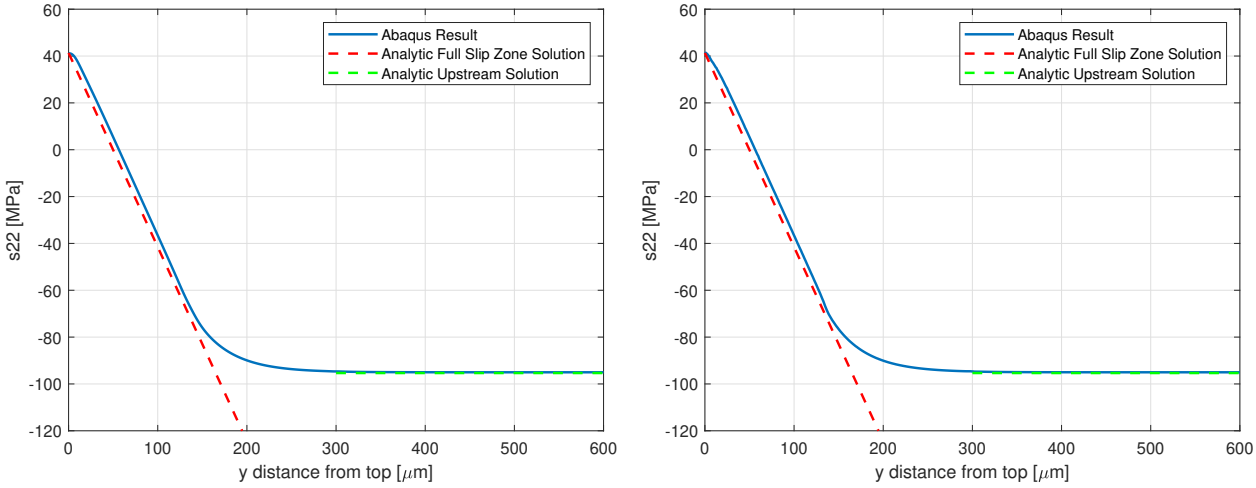


(a) Central Path (b) Outer Path

Figure 22: S22 Comparison with Analytic Solution, Increment 1 (Loading = $1.30 \times 10^{-2}$ N)

Figure 22 shows S22 in the fibre after the first loading increment, corresponding to a pulling force of $1.30 \times 10^{-2}$ N. At this moment, full slip has not been reached, so the S22 curve follows the downstream full-slip solution up until about 150 $\mu$m before reaching the upstream stress value at about 250 $\mu$m.

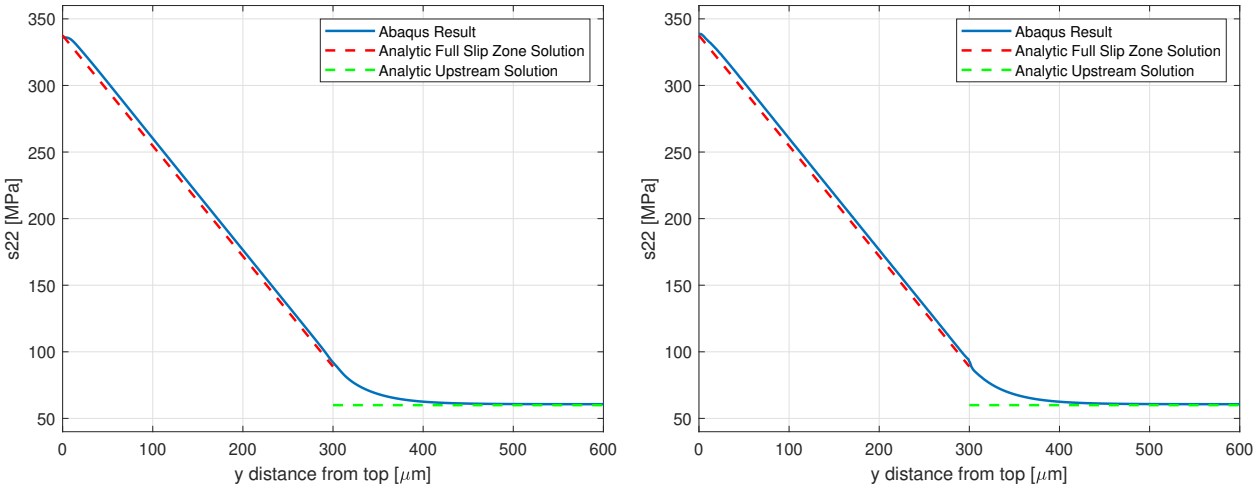


(a) Central Path (b) Outer Path

Figure 23: S22 Comparison with Analytic Solution, Increment 9 (Loading = $1.06 \times 10^{-1}$ N)

Figure 23 shows S22 in the fibre after the ninth loading increment, corresponding to a pulling force of $1.06 \times 10^{-1}$ N. This increment is the moment full slip is reached, as can be seen by the fact that the S22 curve follows the downstream full-slip solution for the entire debonded region (up to 300 $\mu$m).

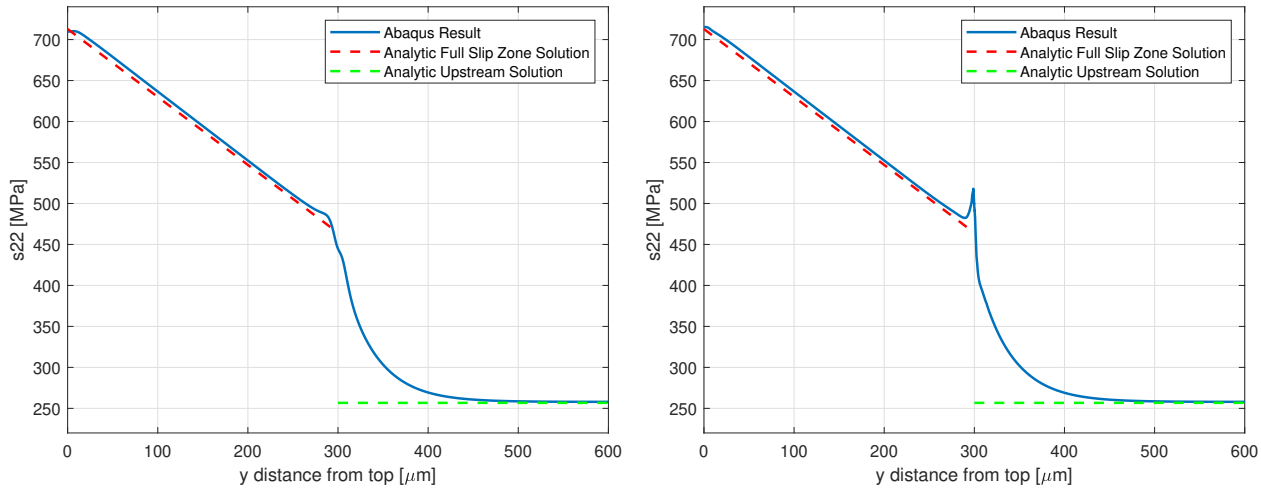


(a) Central Path (b) Outer Path

Figure 24: S22 Comparison with Analytic Solution, Increment 20 (Loading = $2.24 \times 10^{-1}$ N)

Figure 24 shows S22 in the fibre after the 20$^{\text{th}}$ and final loading increment, corresponding to a pulling force of $2.24 \times 10^{-1}$ N. By this point, the system has been loaded well past full slip. The S22 curve still follows the downstream full-slip solution for the entire debonded region, but after 300 $\mu$m, there is a sharp drop off before the curve reaches the upstream stress value at about 450 $\mu$m. In Figure 24b, the influence of the stress concentration at the crack tip on the stress in the outer region of the fibre can clearly be seen.

The crack tip energy release rate is plotted as a function of loading in Figure 25, again with curves for both the Abaqus results and the analytic solution. As the analytic curve is only valid for full slip, the left portion of the curve can be disregarded. Excepting this portion, the analytic curve lines up excellently with the Abaqus results, which show G rapidly increasing once full slip is achieved at a loading level of about 0.1 N.

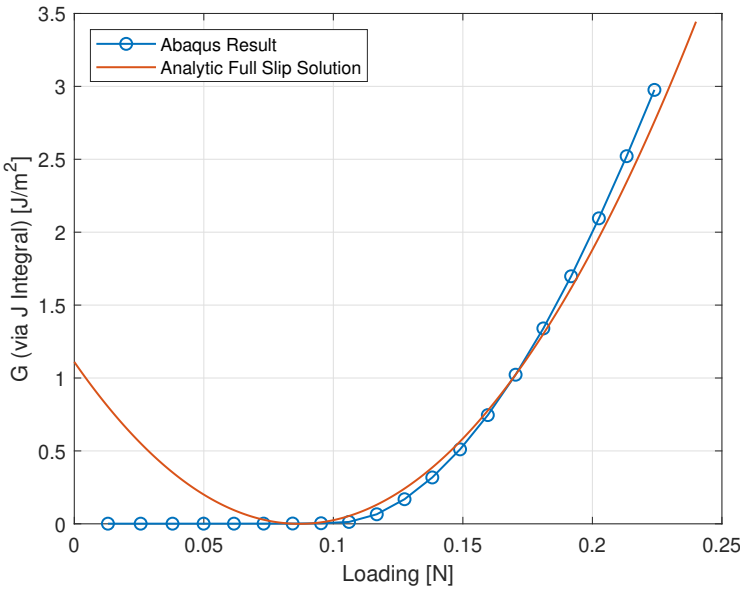


Figure 25: Energy Release Rate vs. Loading, Comparison with Analytic Solution (Calculated with a J-Integral Contour Distance of 0.32962 $\mu$m)

On the whole, as is illustrated by Figures 22 through 25, the single-fibre model Abaqus results correlate very strongly with the analytical solutions for single-fibre pull-out. Therefore, the single-fibre model can be considered to be analytically validated. As the multi-fibre model is based on the single-fibre model, it is considered to also be analytically validated by extension for the purposes of this project.

## 6.3 Testing for Axial Symmetry

As the single-fibre model is, in theory, axisymmetric, the results from Abaqus should not depend on their angular position around the central axis. Therefore, in order to ensure axial symmetry, the energy release rate vs. loading curve was plotted at seven angular positions, as can be seen in Figure 26.

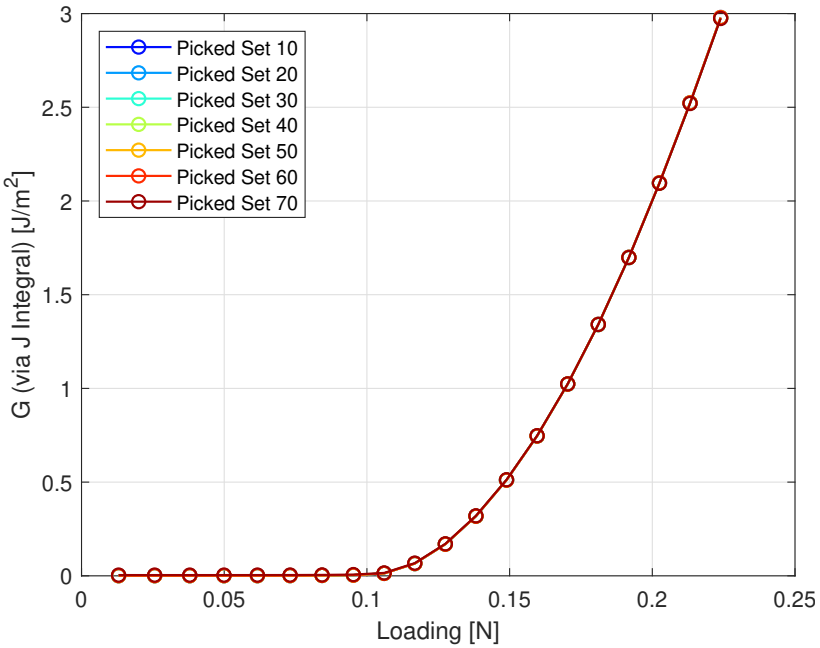


Figure 26: Energy Release Rate vs. Loading, Axial Symmetry Test (Calculated with a J-Integral Contour Distance of 0.32962 $\mu$m)

As Figure 26 illustrates, there is negligible variation between the seven curves plotted, indicating that the Abaqus model accurately captures the axial symmetry of the single-fibre configuration.

## 6.4 Checking for J-Integral Path Dependency

As was discussed in chapter 4, friction along the crack interface can affect J-integral calculations such that they are no longer path-independent. Therefore, in order to observe the path dependency of the of the J-integral results for the single-fibre model, the calculated value for $G$ was plotted with respect to the length of the crack enclosed in the $\Gamma$ contour for each loading increment in Figure 27. Figure 27a shows the raw data, while Figure 27b plots $G$ normalised with respect to the maximum value for each loading increment in order to better observe the shape of each curve.

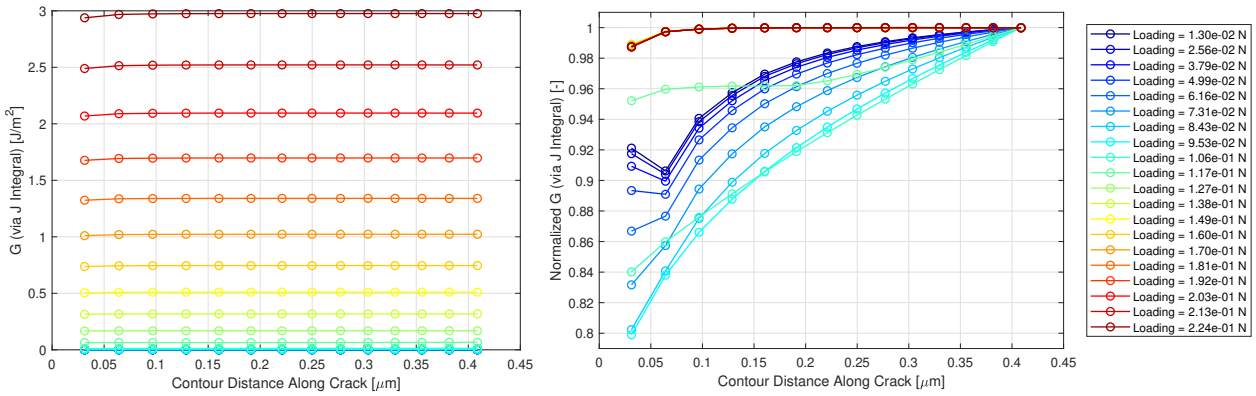


(a) Raw $G$ Values

(b) $G$ Values Normalised with Respect to the Maximum Value for Each Loading Increment

Figure 27: J-Integral Contour Dependency

Counterintuitively, Figure 27b shows that the contour dependency is actually higher for low loading values, and the curves flatten out as full slip is reached. However, when looking at Figure 27a, it can also be seen that $G$ rapidly increases after full slip is reached. The upward slope of the low-load curves might be an artefact of the application of thermal loading, as their actual values are extremely low, as is shown in Figure 27a. The increase in $G$ following full slip then completely overshadows these thermal effects. The apparent lack of contour dependency at high loading values is likely because the length of debond interface included in $\Gamma$ is very small and is also overshadowed by crack tip loading. While the shape of the curves in Figure 27b might merit further investigation, for the purposes of this project, the slight contour dependency at low values should not effect the results, especially when picking a constant contour length for evaluating the J-integral.

## 6.5 Single-Fibre Pull-Out Simulation

In the following section, the progression of the single-fibre model behaviour throughout the course of the simulated fibre pull-out loading step will be illustrated, and the model output data will be explained.

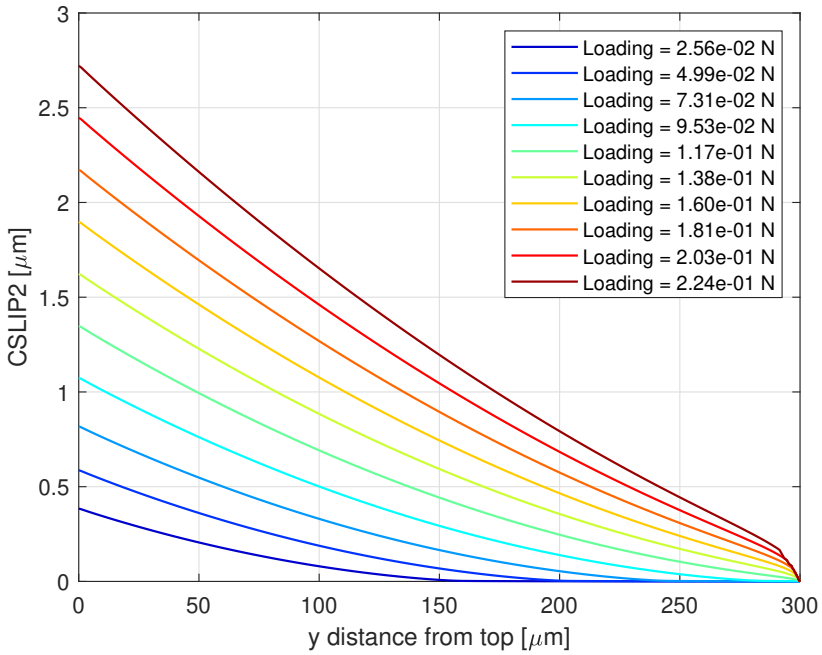


Figure 28: Interfacial Slipping Along Debond Interface, Single-Fibre Model

Figure 28 shows the interfacial slipping along the fibre-matrix debond interface for every other loading increment, with half of the increments removed from the figure for increased clarity. A positive CSLIP2 means that the fibre has slipped in the model's positive y-direction relative to the matrix. Blue colours correspond to the beginning of the loading step, while red colours correspond to the end of the loading step. This colouring convention will be followed for the remainder of this report when several loading increments are plotted together. For the loading step that is plotted in this section, red colours will therefore correspond to high loads. However, for the unloading plots that are included in Chapter 7, note that red colours will correspond to lower loads, as the plots always progress from blue to red with simulated time.

It can be seen in Figure 28 that full slip is achieved when loading reaches $1.17 \times 10^{-1}$ N, as the corresponding curve is the first curve to show non-zero slip for the entire length of the debond zone. Therefore, for the remaining plots in this section, the blue curves can be considered to correspond to partial slip, the green curves can be considered to correspond to the moment full slip is reached, and the orange and red curves can be considered to correspond to full slip behaviour.

Figures 29 and 30 both plot shear stress, and they both illustrate friction along the debond zone interface. Figure 29 directly plots the contact shear stress in the y-direction as output by Abaqus, which is defined as a stress on the debonded surface of the matrix. This stress component is entirely due to frictional forces. Figure 30 shows S12 in the fibre close to the debond interface, and it almost perfectly matches Figure 29, although the curves are inverted, as the shear stress in the fibre acts

in the opposite direction of the shear stress in the matrix. In the case of Figure 29, since the fibre is being pulled out of the matrix in the model's positive y-direction, the matrix is experiencing a positive CSHEAR2 exerted by the fibre.

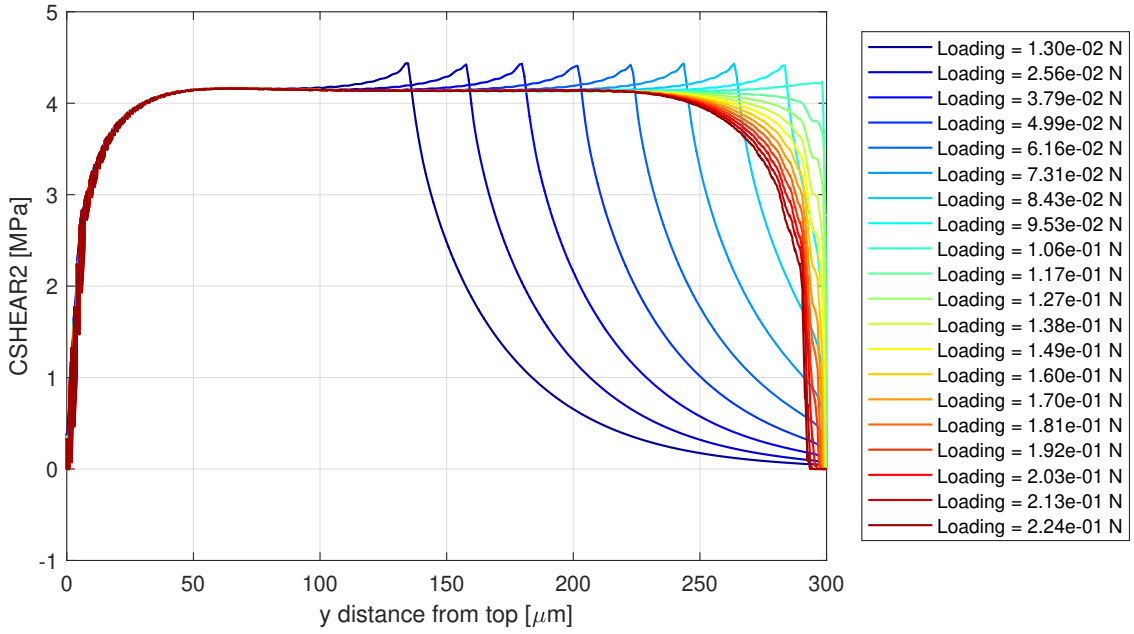


Figure 29: Interfacial Frictional Shear Stress Along Debond Interface, Single-Fibre Model

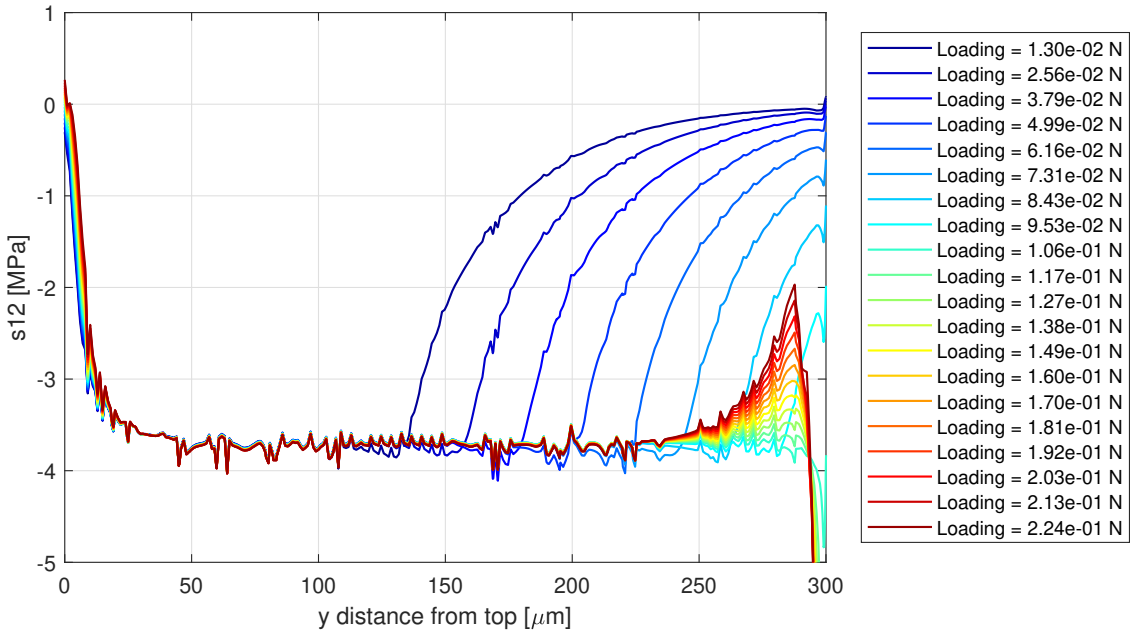


Figure 30: Fibre Shear Stress Through Outer Path, Single-Fibre Model, Cropped View

While Figures 29 and 30 show similar curves, the S12 values plotted in Figure 30 begin to rapidly increase in magnitude close to the crack tip as full slip is reached and exceeded. Figure 31 shows S12 plotted along the entire fibre length, and it provides a clearer picture of what is occurring at this point.

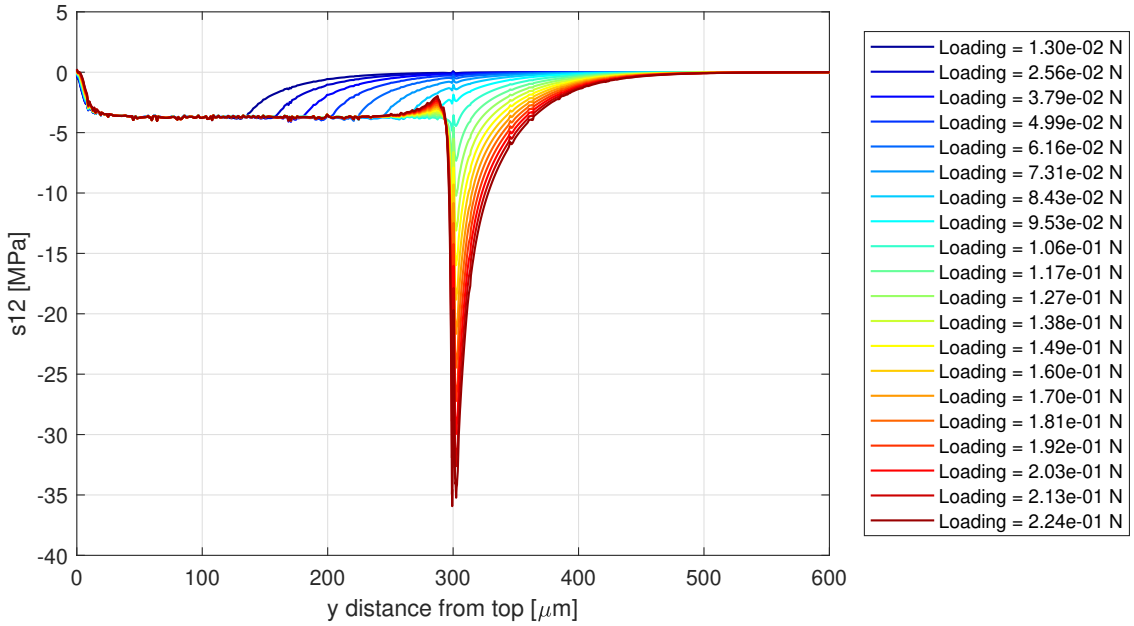


Figure 31: Fibre Shear Stress Through Outer Path, Single-Fibre Model, Full View

As can be observed in Figure 31, the magnitude of the shear stress in the fibre greatly increases at the crack tip after full slip is achieved. This behaviour can be explained as follows:

When the fibre is pulled, the stress at its tip is defined as the force divided by the cross-sectional area of the fibre, establishing a set value at the top. At the other end of the fibre, the stress value is also defined, since at this point, the strain in both the matrix and the fibre are equal and thus the upstream stress in the fibre $\sigma^+$ can be easily calculated as discussed in section 6.2. Therefore, a load transfer from the fibre to the matrix is necessary.

Before full slip is achieved, the frictional force is adequate to transfer the load from the fibre to the matrix, and the shear stress gradually diminishes to zero before reaching the crack tip. However, once full slip is reached, sliding occurs along the entire fibre-matrix interface, and since the frictional shear stress is constrained by the coefficient of kinetic friction, it is no longer sufficient to completely transfer the load from the fibre to the matrix.

After full slip, any remaining load that has not been transferred at the crack tip must be rapidly transferred once the fibre and matrix are bonded. The transferred load can essentially be defined by the area between the x-axis and the S12 curve, and the necessity to transfer a large amount of load over a very short distance results in the spike in S12 observed at the crack tip.

Figure 32 shows the axial stress S22 through the centre of the fibre. The steep decline that can be seen at the crack tip for the full-slip curves illustrates the effects of the increased rate of load transfer near the crack tip that is also apparent in Figure 31.

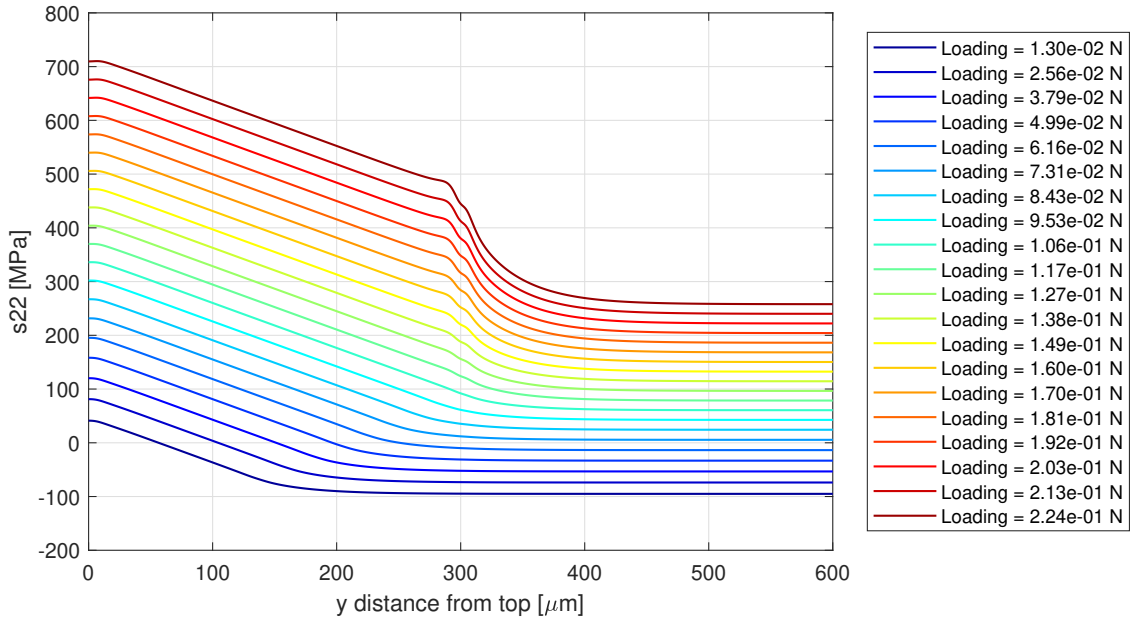


Figure 32: Fibre S22 Through Centre Path, Single-Fibre Model

In Figure 33, the axial stress S22 is again plotted, but this time along the outer path through the fibre that was used for the S12 plots. It can be seen that as loading continues past full slip, a small spike develops near the crack tip. While this result is interesting, further investigation into the mechanisms that create this spike is outside the scope of this project.

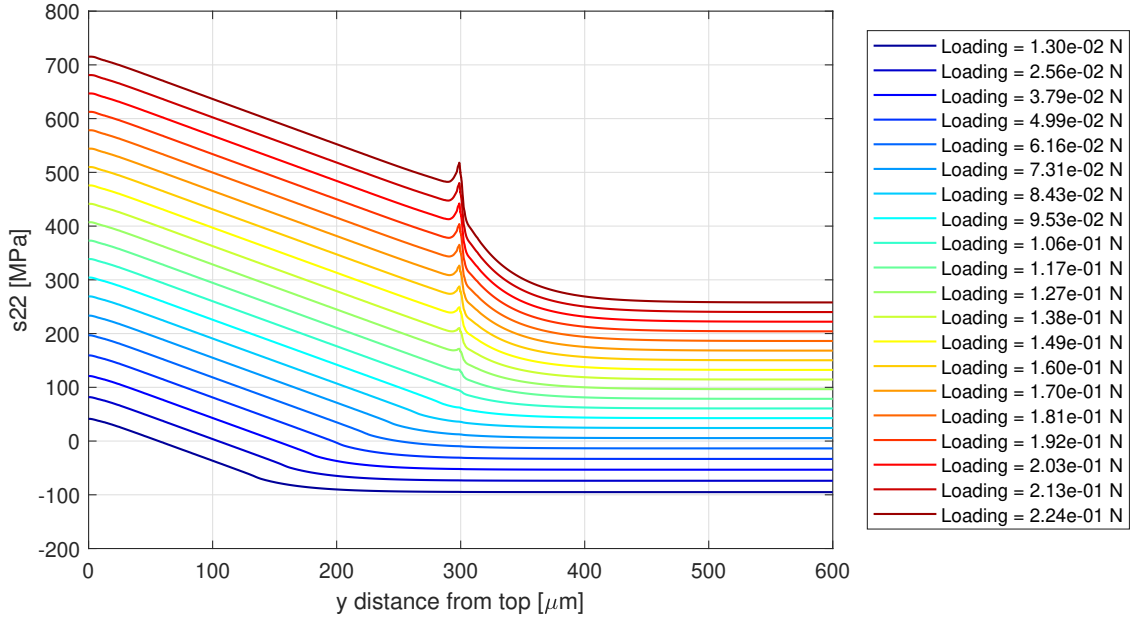


Figure 33: Fibre S22 Through Outer Path, Single-Fibre Model

# 7 Multi-Fibre Model Results

A total of nine multi-fibre simulations were run in Abaqus, varying fibre volume fraction and the coefficient of friction along the debond interface. The control case was run with 55% fibre packing and a coefficient of friction of 0.50. In addition to the control case, five different coefficients of friction were tested ranging from 0 to 1, and three different packing percentages were tested ranging from 25% to 70%.

## 7.1 Control Case Results

In this section, the full range of results from the control case simulations will be presented in order to illustrate the model behaviour throughout the loading process. For other cases, specific plots will be presented as relevant. The full results for each of the cases are included in appendices B and C. The behaviour of the broken fibre will first be presented, and the behaviour of the neighbouring fibre will follow.

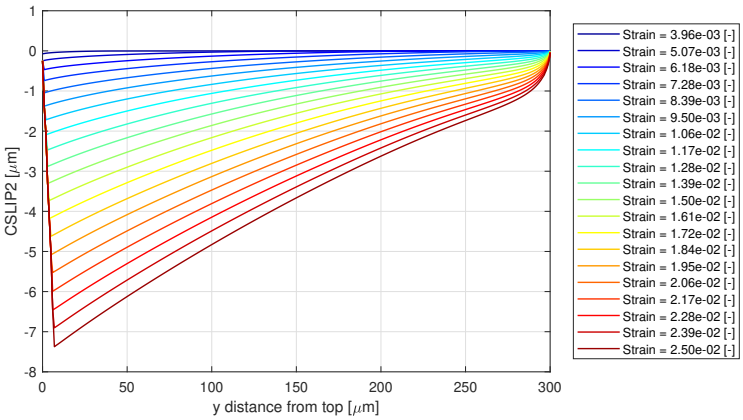


(a) Initial Loading Step

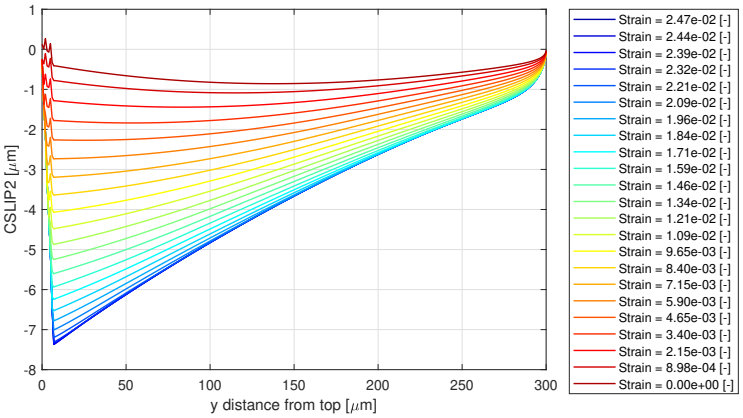


(b) Unloading Step

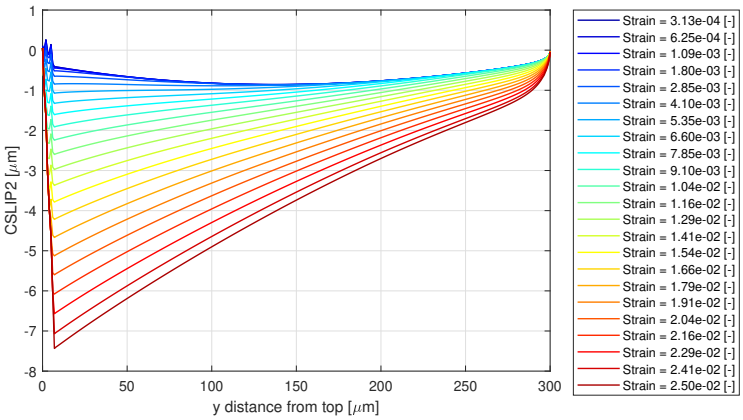


(c) Reloading Step

Figure 34: Interfacial Slipping Along Debond Interface, $\mu = 0.50$

Figure 34 shows the the interfacial slipping along the fibre-matrix debond interface throughout the loading, unloading, and reloading steps. Since the multi-fibre model is loaded by pulling on the bottom, bonded side of the model, the CSLIP2 values are negative, as the fibre is essentially being pulled in instead of being pulled out, as was the case for the single-fibre model. Note that the zero values on the left side of the plots are due to the fact that CSLIP2 cannot be calculated where the fibre has pulled into the matrix and there is no longer contact between the two. Figure 34a indicates that full-slip is achieved near a strain value of $1.17 \times 10^{-2}$. In Figure 34b, it can be seen that there is sufficient friction to prevent the fibre from returning to its original position, and the presence of significant reverse sticking is indicated by the bunching of curves along the path of the first increment.

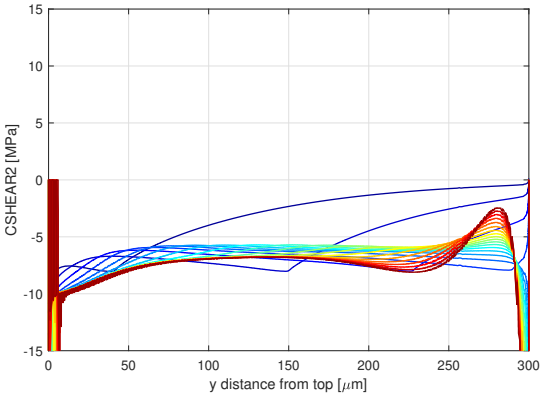


(a) Initial Loading Step

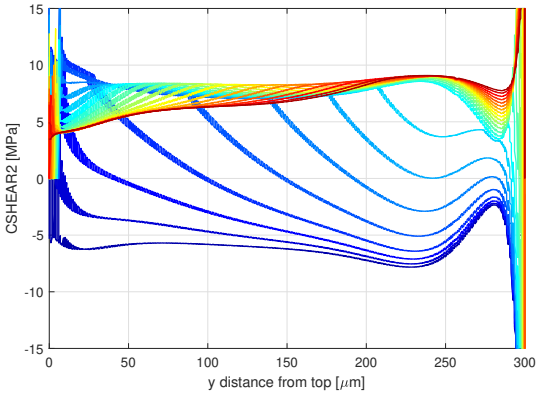


(b) Unloading Step

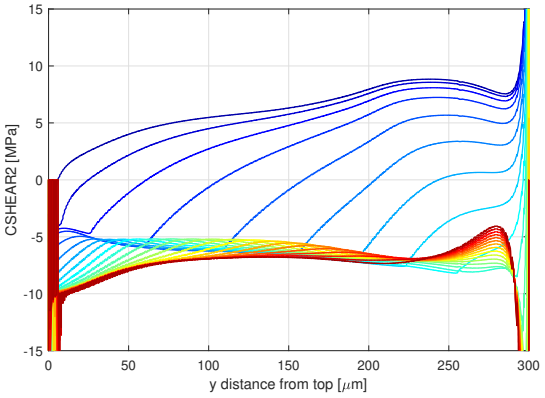


(c) Reloading Step

Figure 35: Shear Stress Along Debond Interface, $\mu = 0.50$

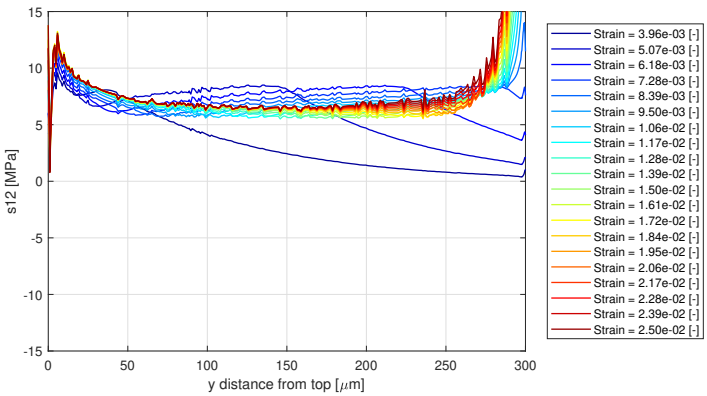


(a) Initial Loading Step

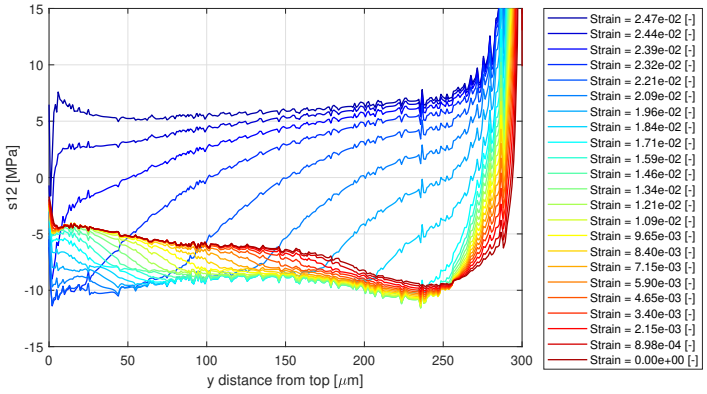


(b) Unloading Step

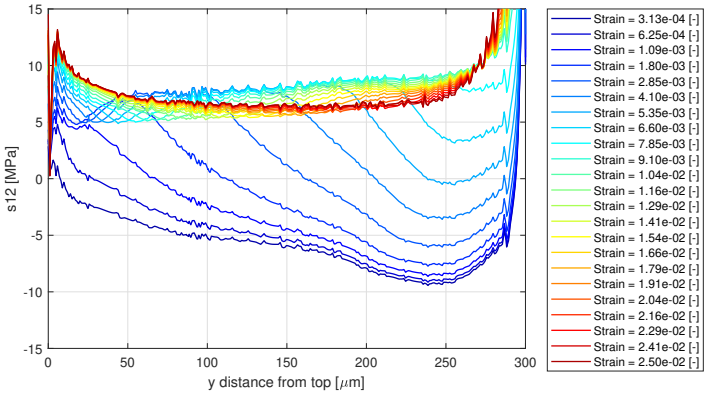


(c) Reloading Step

Figure 36: Broken Fibre Shear Stress Through Outer Path, $\mu = 0.50$, Cropped View

As in Figures 29 and 30, Figures 35 and 36 give the frictional contact shear stress and S12 in the fibre close to the debond interface, respectively. Note that again, the signs of the shear stress values (in the loading step) are the reverse of what they were for the single-fibre model due to the change in the loading procedure. Here, a negative CSHEAR2 value means that the fibre is trying to slip into the matrix, with the matrix resisting. As with Figures 29 and 30, Figures 35 and 36 are nearly mirror images of each other.

Focusing on the unloading step, residual negative CSHEAR2 values are observed in the early increments before a positive reverse slipping friction CSHEAR2 value is reached, with the fibre sliding back out of the matrix. Reverse sticking is indicated by curves with positive values that remain separate from the grouping of slipping friction curves, and it remains present through the eighth unloading increment.

In the reloading step, residual positive CSHEAR2 values are present before the curves eventually settle into the same full-slip path that occurred in the loading step, with full-slip occurring later in the reloading step than the loading step. However, the final shape of the full-slip curve is the same.

As before, when zooming out from Figure 36, it can be seen that S12 values spike dramatically near the crack tip, which is shown in Figure 37. Note that the magnitude of the S12 spike is much greater for the control multi-fibre model than for the single-fibre model, even though both impose the same coefficient of friction in the debond zone, alluding to some of the fundamental differences between the two models that will be discussed in chapter 8.

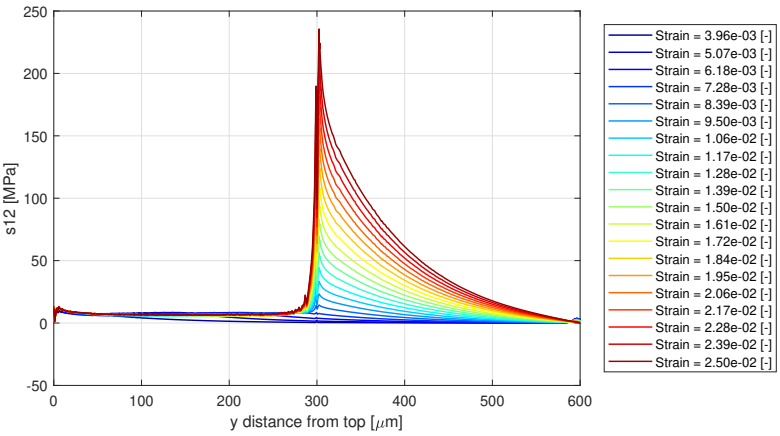


(a) Initial Loading Step

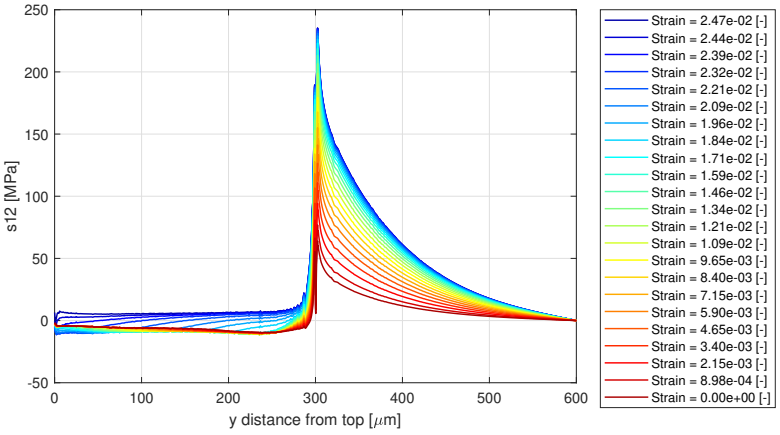


(b) Unloading Step

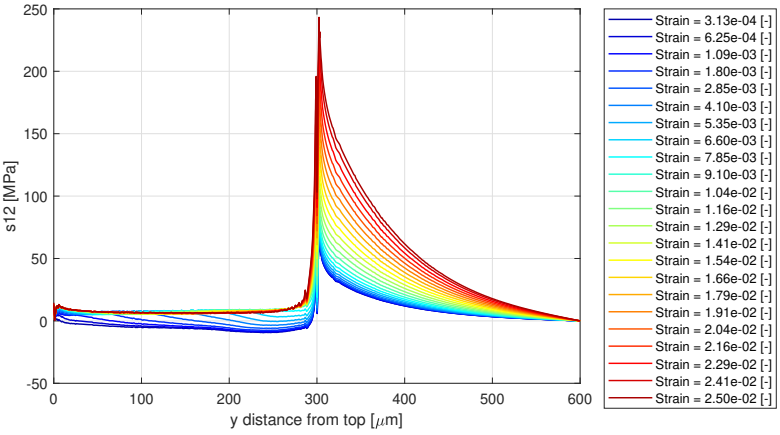


(c) Reloading Step

Figure 37: Broken Fibre Shear Stress Through Outer Path, $\mu = 0.50$, Full View

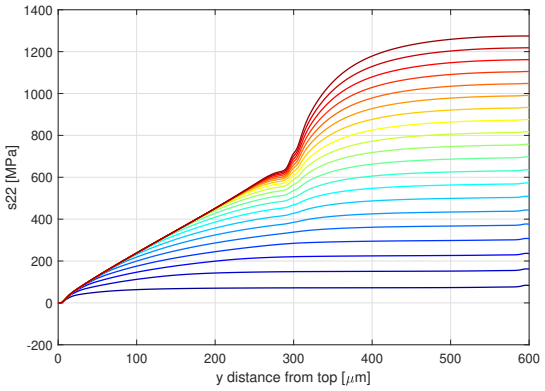


(a) Initial Loading Step

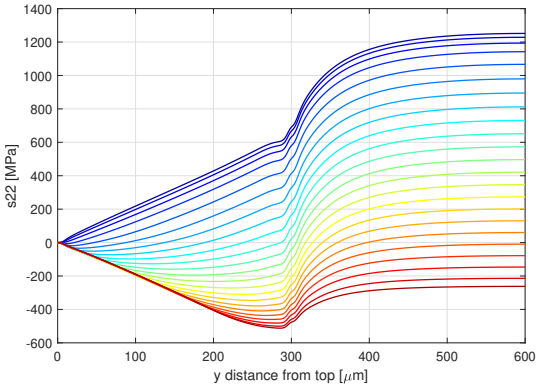


(b) Unloading Step

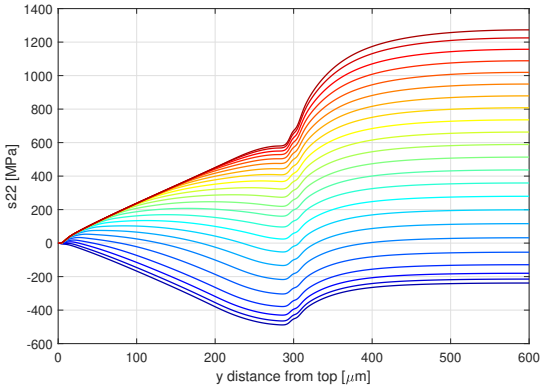


(c) Reloading Step

Figure 38: Broken Fibre S22 Through Centre Path, $\mu = 0.50$

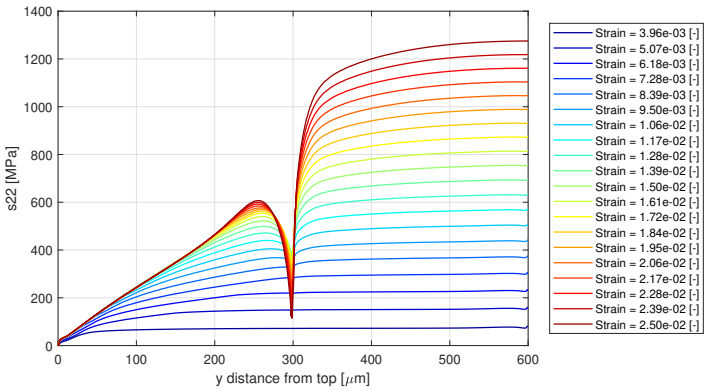


(a) Initial Loading Step

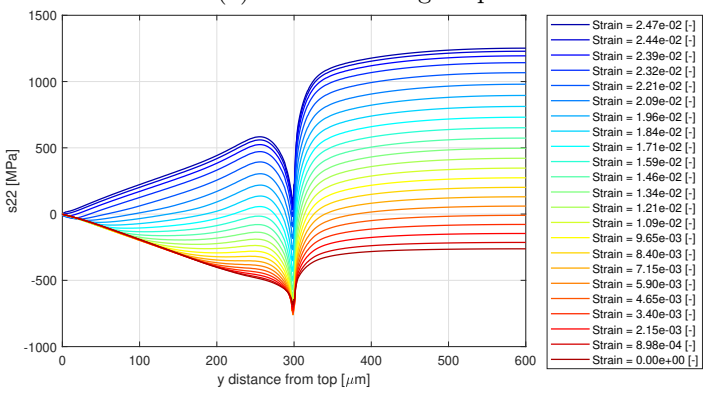


(b) Unloading Step

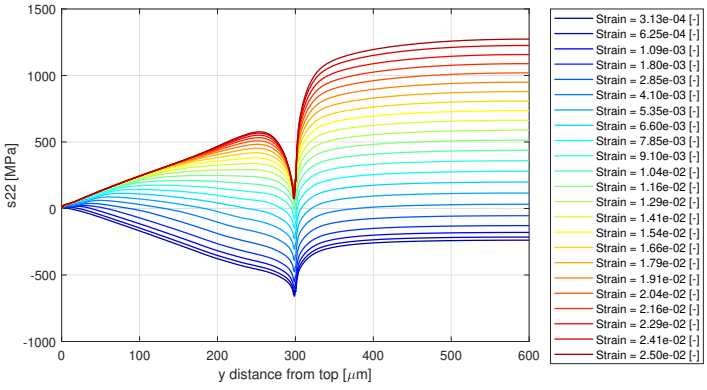


(c) Reloading Step

Figure 39: Broken Fibre S22 Through Outer Path, $\mu = 0.50$

Figures 38 and 39 show the axial stress in the broken fibre along the centre and outer paths, respectively, as in Figures 32 and 33. In Figure 38a, it can be seen that the slope of the S22 curve increases following the crack tip for the full-slip increments as was observed in the single-fibre model.

During unloading, shown in Figure 38b, the fibre transitions into compression, with the debonded portion seeing higher compressive stress values than the bonded portion, which makes sense when considering the effects of reverse sticking and slipping friction. The compression in the bonded portion is a result of the thermal loading procedure; this behaviour is discussed further at the end of this section.

The spike in S22 along the outer path near the crack tip that was observed in Figure 33 is again seen in Figure 39, and it is much more pronounced in the multi-fibre model. This spike represents an area of localised compression in the broken fibre, which is generally experiencing tension. This phenomenon is related to the stress fields around the crack tip, but again, its specific cause is not in the scope of this project. Notably, the spike propagates through the rest of the simulation steps, with its influence evidently being sustained by frictional effects.

Figure 40 shows the crack tip energy release rate $G$, as calculated via the J-integral, as a function of strain across the three loading/unloading steps. Note that in Figure 40b, the direction of the x-axis is flipped so that the three curves taken together illustrate the model's behaviour through time. The presence of reverse sticking during unloading is evidenced by the shallow slope of the $G$ curve at the beginning of the unloading step, as the driving force on the crack tip is not relieved until the fibre is able to slide back towards its original position.

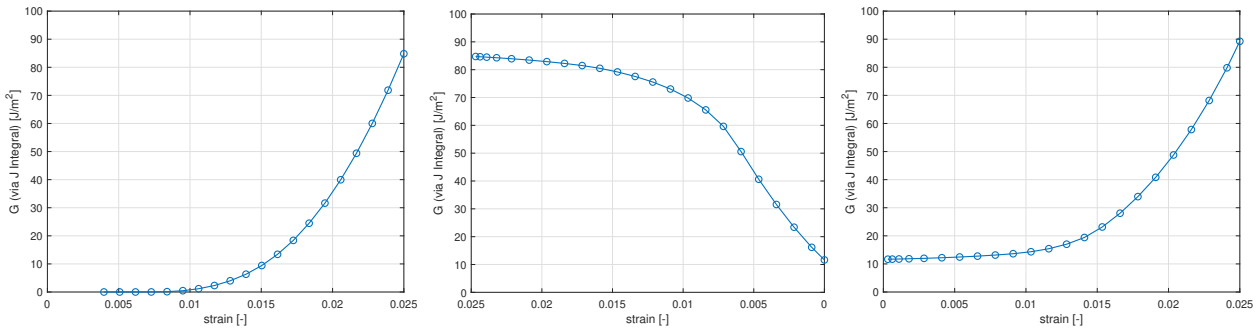


(a) Initial Loading Step (b) Unloading Step (c) Reloading Step

Figure 40: Energy Release Rate vs. Strain, $\mu = 0.50$

It has already been demonstrated how $G$ increases rapidly after full slip is reached. Now, the behaviour of the neighbouring fibre will be investigated, with special attention given to the effects of the stress field around the debond crack tip on the stress in the neighbouring fibre.

Figure 41 shows S22 along the surface of the neighbouring fibre for each loading increment. Note that the neighbouring fibre path plots in the fibre direction were all generated using a vertical path along the edge of the fibre intersecting the symmetry boundary plane of the model (at 0° as defined in Figure 44). The influence of the stress field surrounding the debond crack tip is immediately apparent, manifesting itself as a localised spike in the stress in the neighbouring fibre. However, under the prescribed thermal loading conditions with $\mu = 0.50$ and 55% fibre packing, the maximum stress in the fibre does not occur at this spike; rather, it occurs at the top of the model, closest to the location of the fracture of the broken fibre.

Figure 42 shows S12 in the neighbouring fibre along the same path. While the magnitude of the shear stress is generally much smaller than the magnitude of the axial stress, the influence of the crack tip stress field is much more evident here. While the spike in S12 near the crack tip is not an indication of likely fibre failure, it could be an indication of potential matrix failure. However, matrix failure is not the focus of this present work.

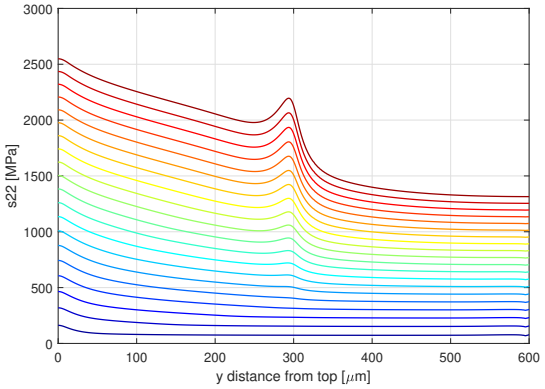


(a) Initial Loading Step

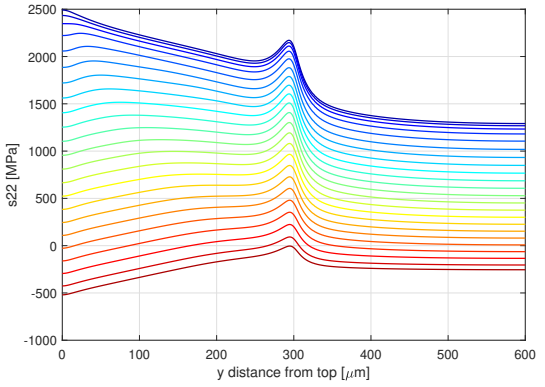


(b) Unloading Step

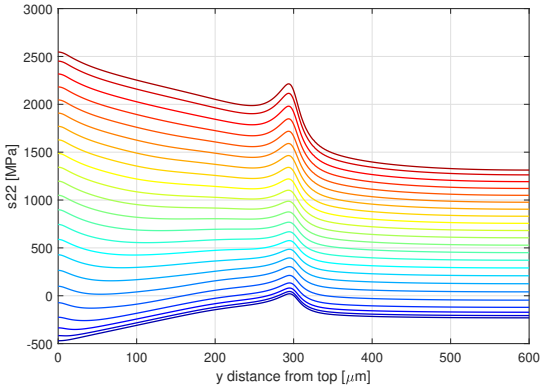


(c) Reloading Step

Figure 41: S22 at Surface of Neighbouring Fibre, $\mu = 0.50$

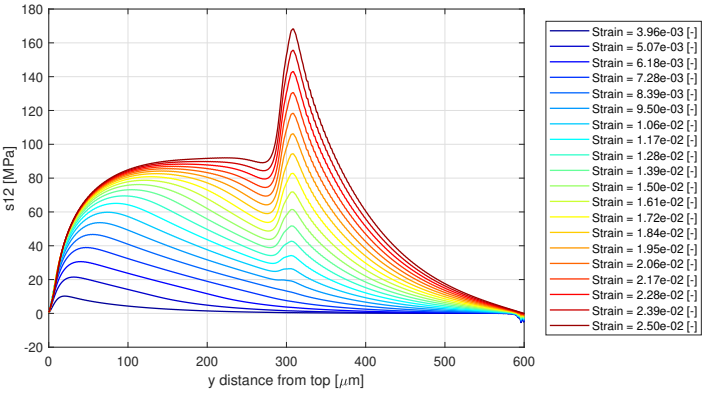


(a) Initial Loading Step

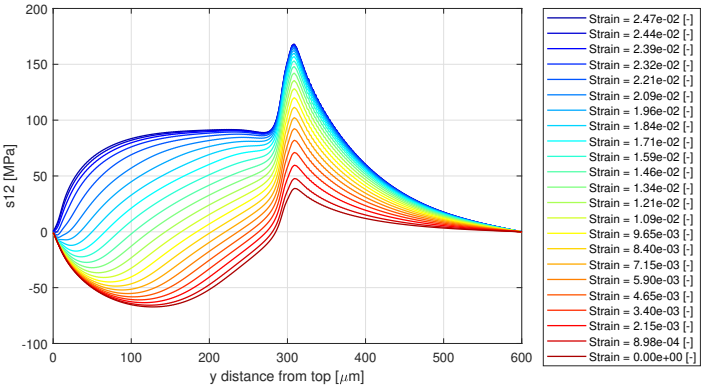


(b) Unloading Step

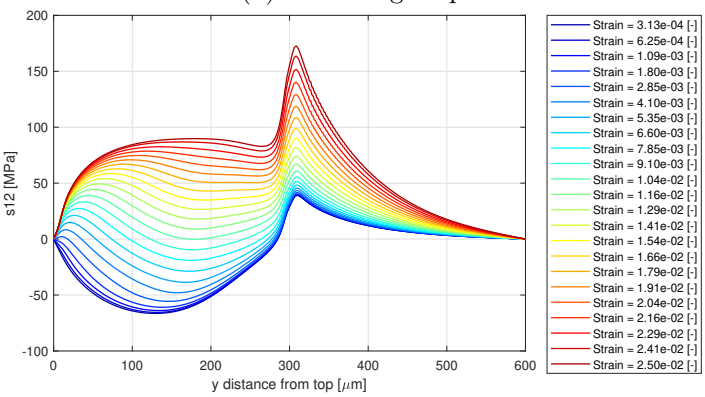


(c) Reloading Step

Figure 42: S12 at Surface of Neighbouring Fibre, $\mu = 0.50$

S22 in the neighbouring fibre was also plotted along a circular path at the middle of the fibre (300 $\mu$m from the fibre fracture plane), in the plane of the debond crack tip. This path is illustrated in Figure 44. The resulting S22 plots for the three loading steps are given in Figure 43. Although the distance between the broken and neighbouring fibres is smallest at 30°, the maximum S22 value actually occurs below 30°, with S22 being essentially constant from 0° to slightly under 30°.

This result can be explained by considering the effects of two broken fibres. Looking again at Figure 12, it can be seen that at the 0° position, the neighbouring fibre is exposed to the stress fields from two debond crack tips, since the finite element model boundary is defined as a symmetry plane. Such a finding also validates the use of vertical path plots at 0° when capturing the behaviour of the neighbouring fibre in the y-direction and when determining the maximum S22 value in the neighbouring fibre.

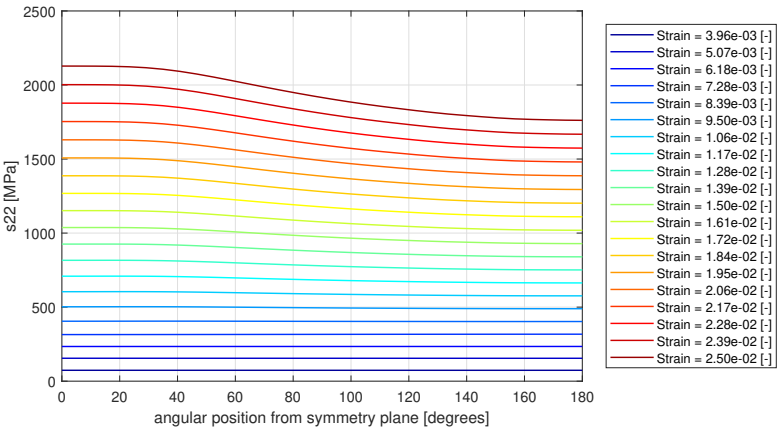


(a) Initial Loading Step

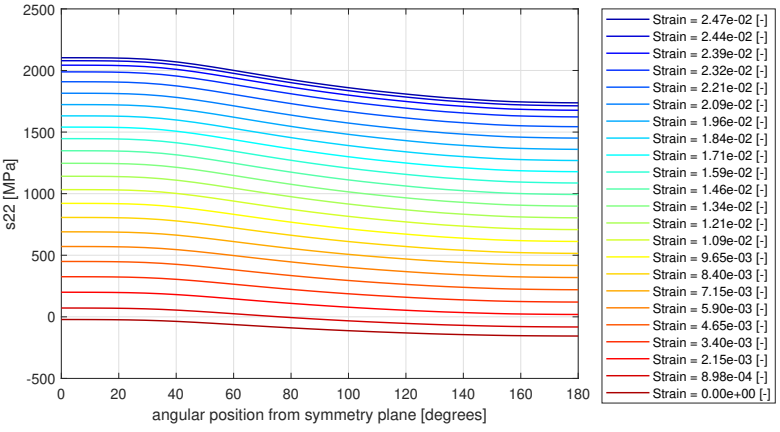


(b) Unloading Step

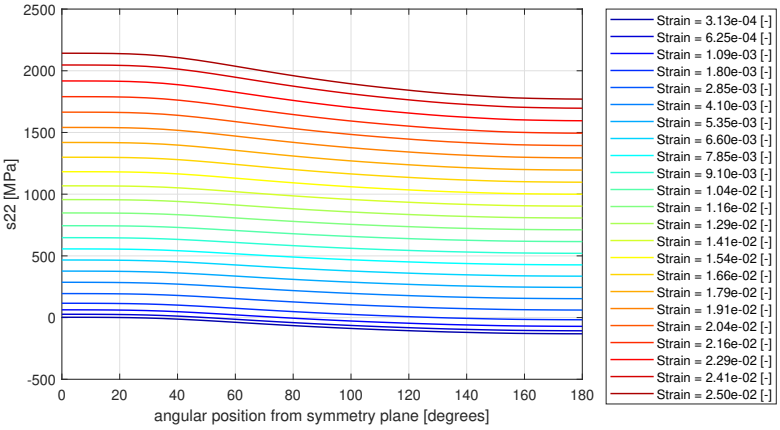


(c) Reloading Step

Figure 43: S22 Along Perimeter of Neighbouring Fibre Cross Section, $\mu = 0.50$

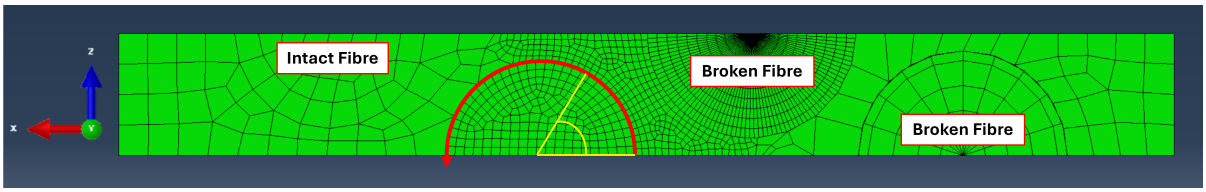


Figure 44: Neighbouring Fibre Circular Path (Taken at the Debond Crack Tip Plane)

Figure 45 shows the maximum value of S22 that was found for each increment along the vertical path with respect to strain across the three loading/unloading steps. As the maximum stress for this simulation case was largely unrelated to the debond crack tip stress zone, Figure 45 contains rather linear curves.

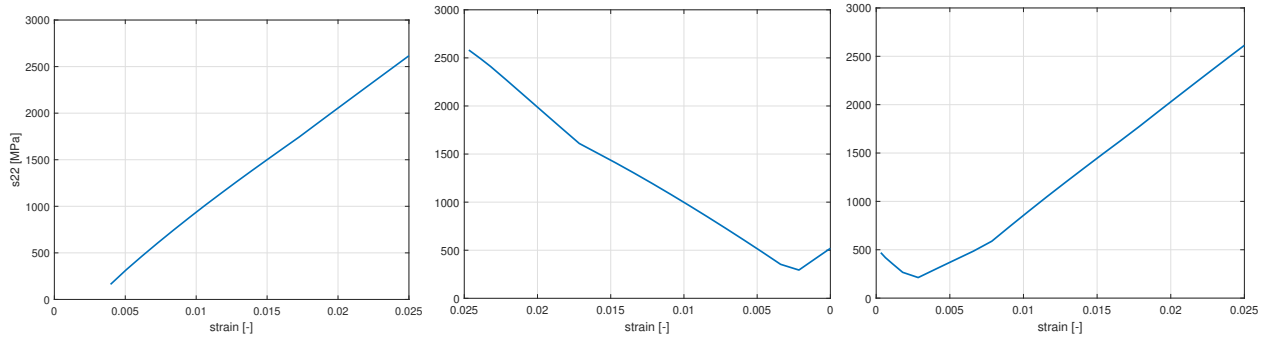


(a) Initial Loading Step (b) Unloading Step (c) Reloading Step

Figure 45: Max. S22 (Absolute Value) in Neighbouring Fibre vs. Strain, $\mu = 0.50$

The small increase in S22 between the unloading and loading steps is due to the thermal expansion that occurs before the first loading step. Since the strain at the end of the unloading step (and the beginning of the reloading step) is defined to be zero, the unloading step actually exerts a compressive load onto the system at the end of the step as it pushes the model past its post-thermal expansion equilibrium state. This effect is illustrated visually in Figure 46. This compressive loading is not accurate to the system that is being modelled, but as it does not interfere with the results of interest, it was tolerated.

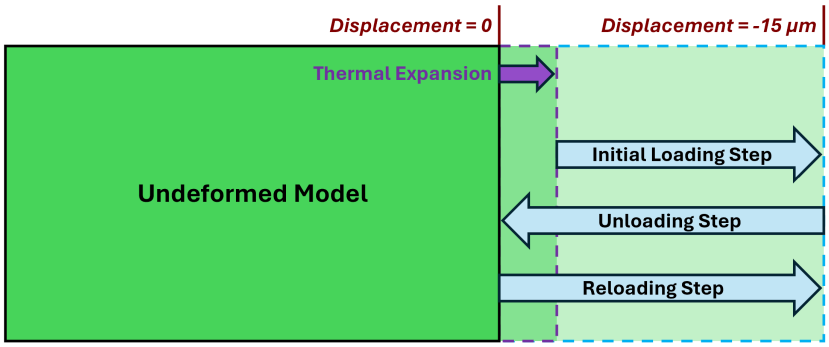


Figure 46: Schematic Illustration of the Effect of Thermal Expansion on the Loading Steps

## 7.2 Varying the Coefficient of Friction Over the Debond Interface

The coefficient of friction $\mu$ along the debonded portion of the fibre-matrix interface was varied from 1 to 0 in order to simulate the effects of the erosion of asperities along this interface after sustained cyclic loading. In total, seven $\mu$ values were tested, including one frictionless case. For each case, a full simulation was run, and plots were generated and investigated as they were for the control case discussed in section 7.1. Selected results, primarily showing $G$ at the debond crack tip and S22 in the neighbouring fibre, are included in this section, and the remaining results can be found in Appendix B.

In order to more easily observe the effects of varying $\mu$, for each loading step, one S22 vs. y-distance curve was taken from each case, and the six curves were plotted together. The specific increments plotted were chosen so as to match the upstream stress value (i.e. the value when the y-distance equals 600 $\mu$m) while also occurring near the end of each loading step. The resulting plots are provided as Figures 47 through 49.

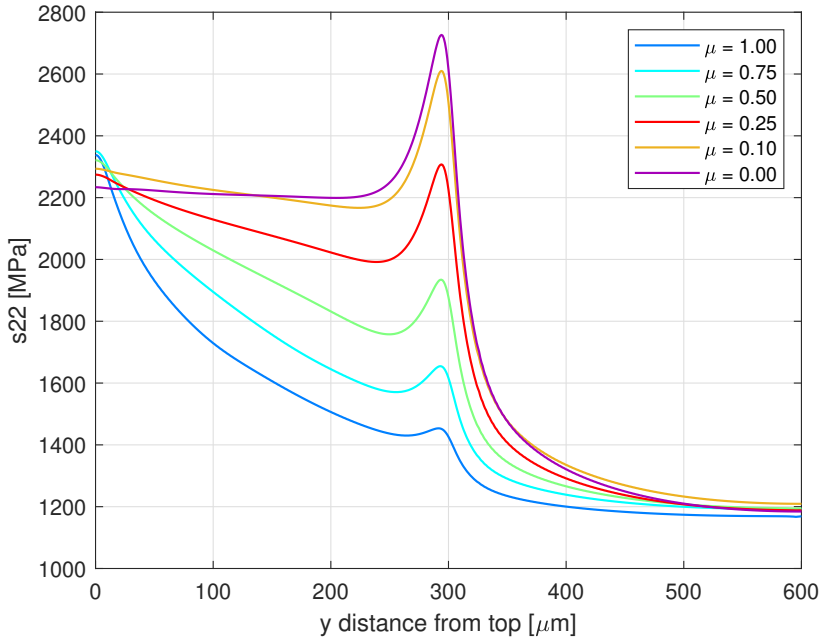


Figure 47: S22 at Surface of Neighbouring Fibre Under Various Coefficients of Friction, Initial Loading Step, 55% Fibre Volume Packing

Figure 47, along with Figure 49, are some of the most important results of this thesis, as they directly show how a decrease in friction along the debond interface can cause an increase in the maximum stress on the surface of neighbouring fibres for the same upstream stress. Figure 48 presents an interesting result that is perhaps more useful for understanding the system's behaviour than for predicting fibre failure. Notably, the highest S22 values near the end of the unloading step occurred in the control case ($\mu = 0.50$) as opposed to either of the extreme cases.

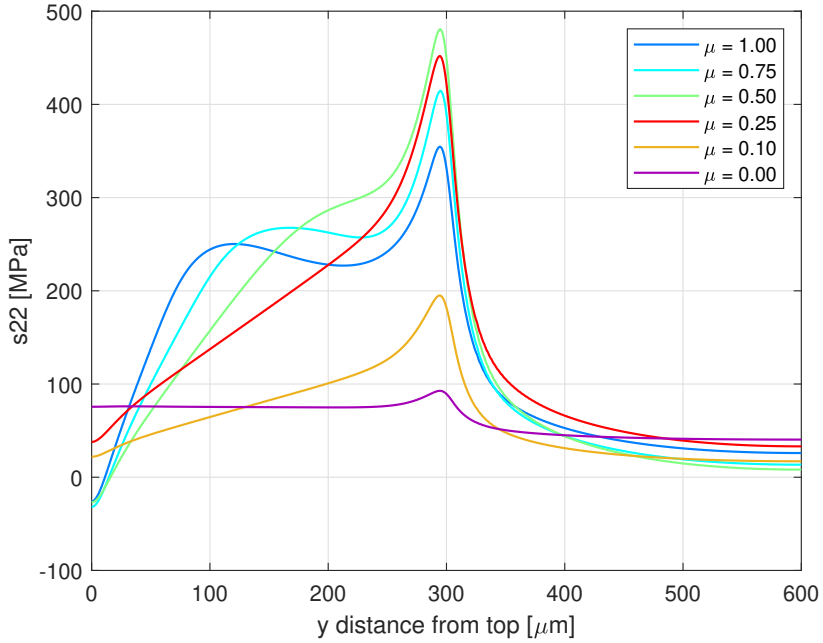


Figure 48: S22 at Surface of Neighbouring Fibre Under Various Coefficients of Friction, Unloading Step, 55% Fibre Volume Packing

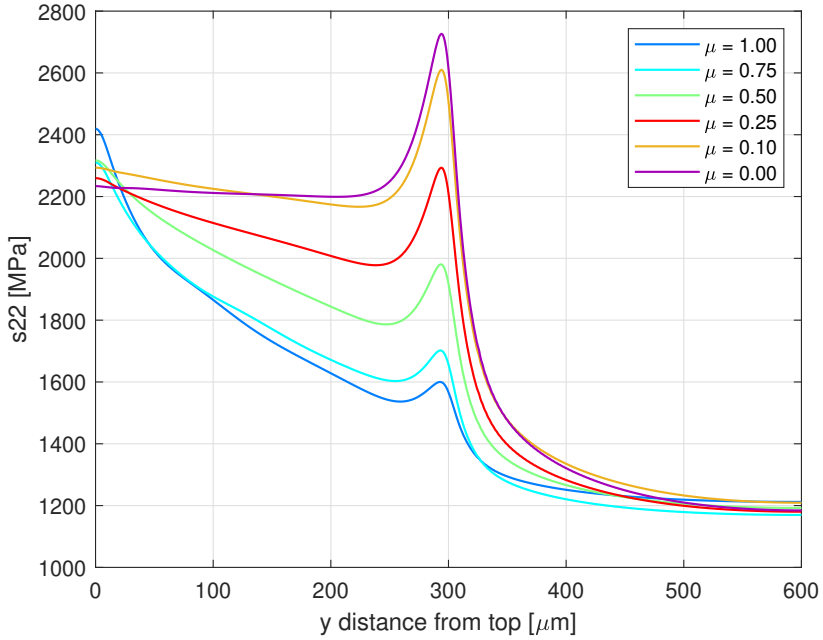


Figure 49: S22 at Surface of Neighbouring Fibre Under Various Coefficients of Friction, Reloading Step, 55% Fibre Volume Packing

### 7.2.1 $\mu = 1.00$

Figure 50 shows $G$ as a function of strain across the three loading/unloading steps for the $\mu = 1.00$ case, which was the highest coefficient of friction tested. Compared to Figure 40, the sticking during the unloading step is increased, leading to an even shallower slope on the left side of Figure 50b. Furthermore, the maximum $G$ value is much smaller for the $\mu = 1.00$ than for the control case, which shows how increased frictional forces can reduce the driving force on the crack tip.

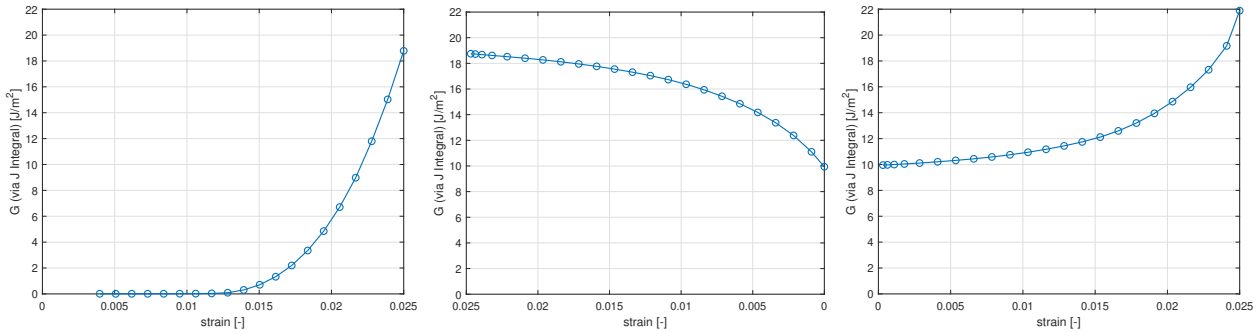


(a) Initial Loading Step (b) Unloading Step (c) Reloading Step

Figure 50: Energy Release Rate vs. Strain, $\mu = 1.00$

Moving on to the neighbouring fibre, Figure 51 shows the maximum S22 in that fibre for the $\mu = 1.00$ case. Under these friction conditions, however, Figure 51 is dominated by the stress at the top of the fibre and is therefore unrelated to the crack tip effects.

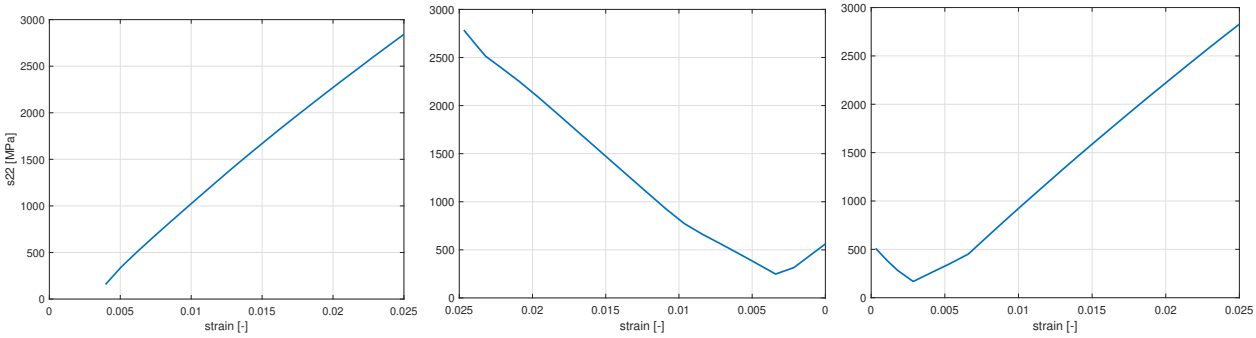


(a) Initial Loading Step (b) Unloading Step (c) Reloading Step

Figure 51: Max. S22 (Absolute Value) in Neighbouring Fibre vs. Strain, $\mu = 1.00$

Figure 52 gives S22 in the neighbouring fibre as a function of y-distance for the $\mu = 1.00$ case, and it shows how the maximum stress occurs far downstream of the debond crack tip. At such a high coefficient of friction, the frictional forces are sufficient to transfer a significant portion of the load from the broken fibre to the matrix, leading to a lower crack tip energy release rate, leading to a weaker stress field surrounding the debond crack tip, leading to relatively minor spikes in S22 in the neighbouring fibre near the crack tip.

Notably, looking at the last increment in the loading step shown in Figure 52a, both the maximum S22 on the left side of the plot and the upstream S22 value on the right side of the plot are higher than they were in the control case. This result suggests that a higher coefficient of friction increases the overall stiffness of the composite specimen, with stress values being higher overall for a given imposed strain.

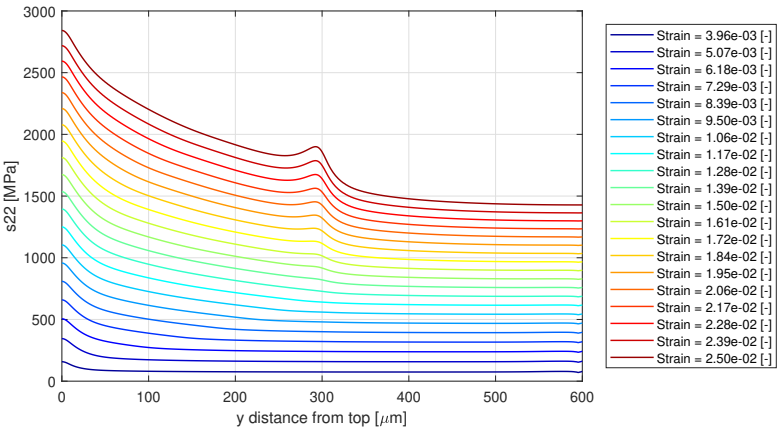


(a) Initial Loading Step

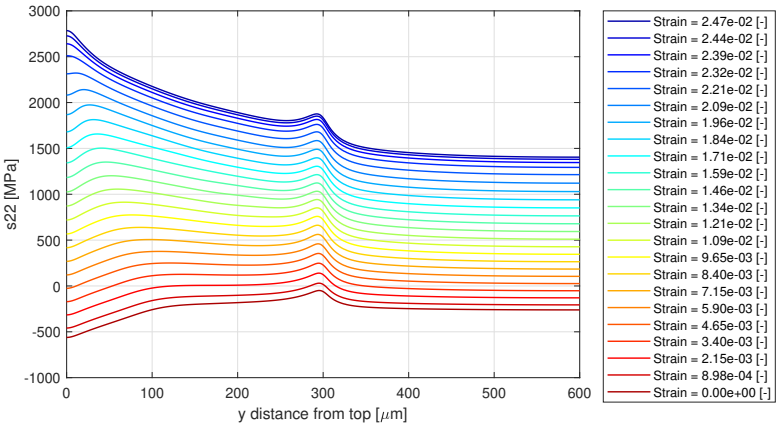


(b) Unloading Step

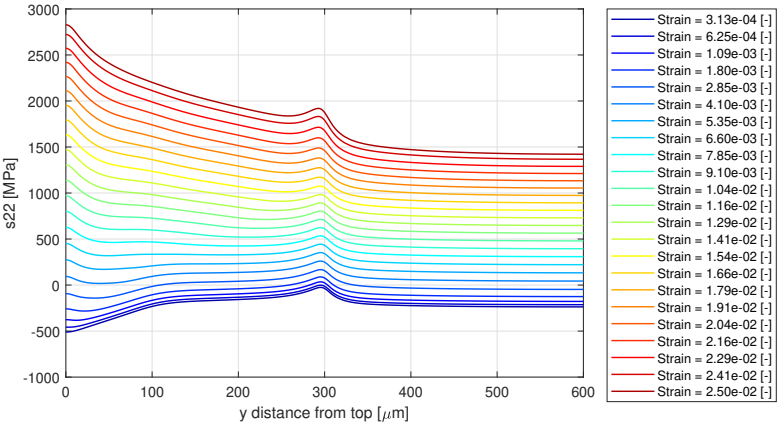


(c) Reloading Step

Figure 52: S22 at Surface of Neighbouring Fibre, $\mu = 1.00$

### 7.2.2 $\mu = 0.75$

The results for the $\mu = 0.75$ case are highly similar to the results for the $\mu = 1.00$ case. Looking at Figure 53b, it can be seen that the sticking in the unloading step is less significant that it was for the $\mu = 1.00$ case, but the broken fibre still does not slip back sufficiently so that the $G$ curve starts to flatten out again as it approaches zero. That being said, there is a significant increase in the maximum value of $G$ compared to the $\mu = 1.00$ case, with the maximum $G$ more than doubling.

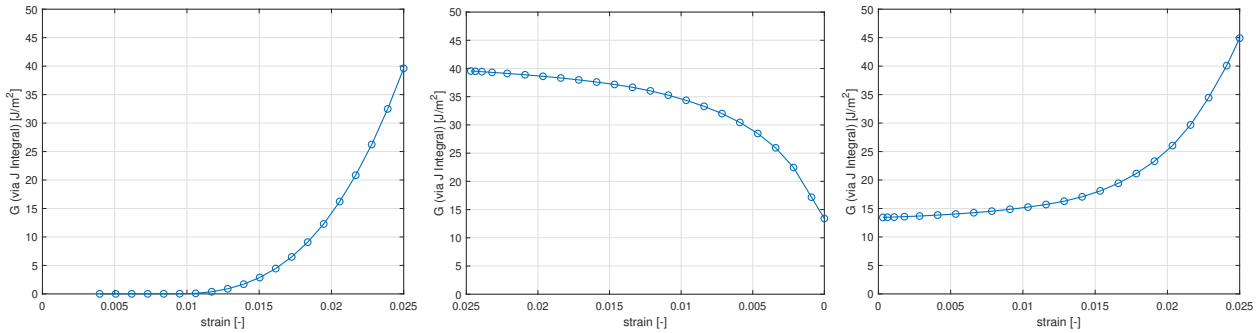


(a) Initial Loading Step (b) Unloading Step (c) Reloading Step

Figure 53: Energy Release Rate vs. Strain, $\mu = 0.75$

The maximum loading in the neighbouring fibre is still dominated by the top of the fibre, meaning that there is little change from Figure 51 to Figure 54.

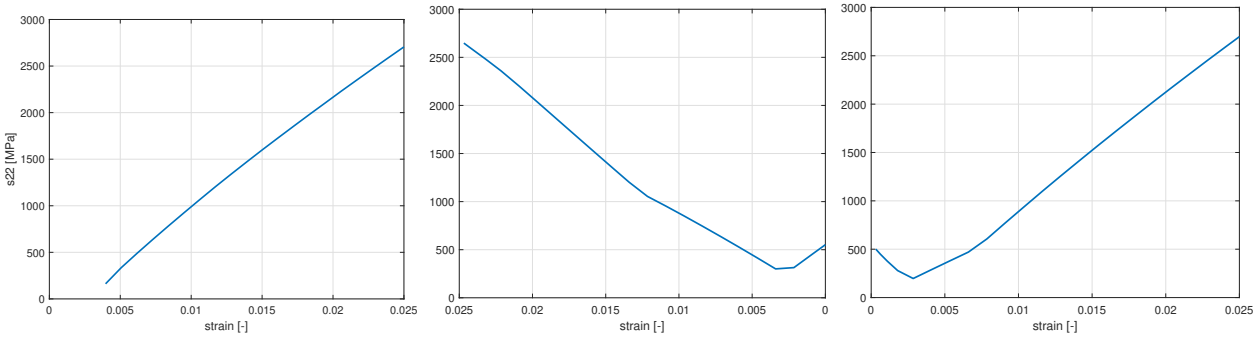


(a) Initial Loading Step (b) Unloading Step (c) Reloading Step

Figure 54: Max. S22 (Absolute Value) in Neighbouring Fibre vs. Strain, $\mu = 0.75$

While the plots for S22 in the neighbouring fibre with respect to y-distance for the $\mu = 1.00$ case and the $\mu = 0.75$ case are quite similar, when comparing Figures 52, 55, and 41, the beginnings of the trend depicted in Figures 47 through 49 begin to emerge. As friction decreases, the magnitude of the S22 spike near the crack tip increases relative to the magnitude of S22 at the top of the fibre near the fibre fracture location.

The $\mu = 1.00$ case and the $\mu = 0.75$ both are dominated by high friction forces that may in actuality be higher than what would be seen in practice, since the thermal expansion mismatch between fibre and matrix is higher than what would be likely seen in reality, as will be discussed further in chapter 8. The next three cases presented have lower coefficients of friction than the control case, and they produce arguably more noteworthy results.

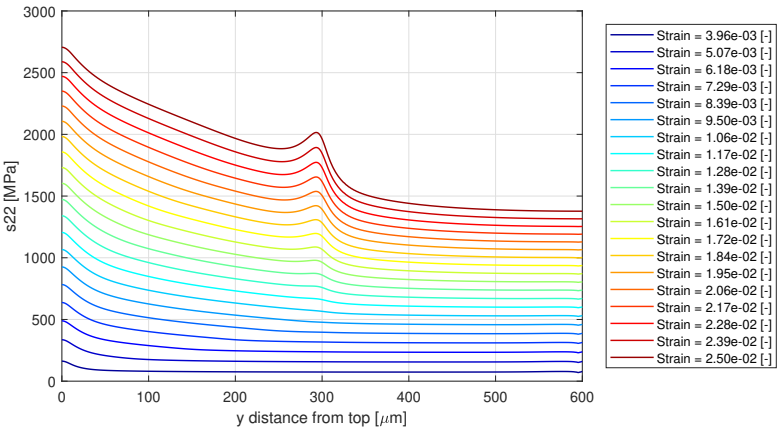


(a) Initial Loading Step

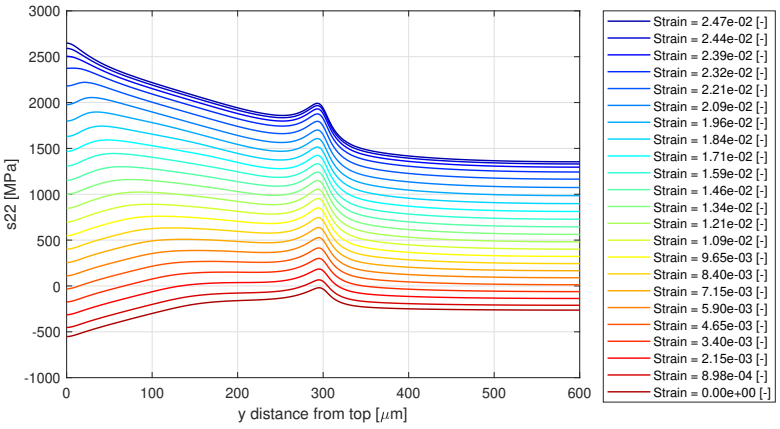


(b) Unloading Step

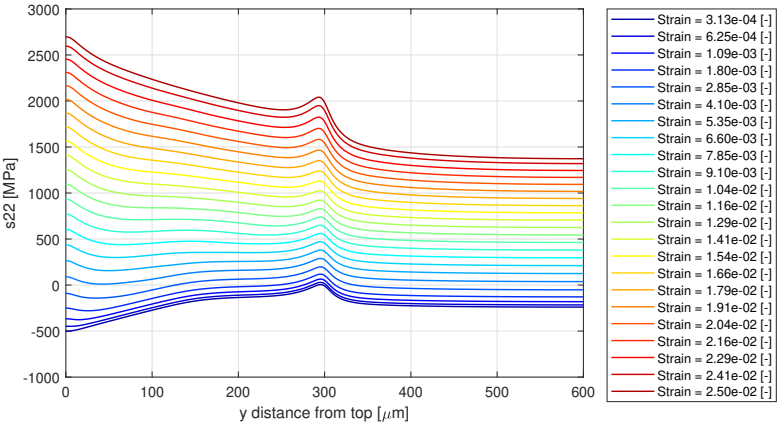


(c) Reloading Step

Figure 55: S22 at Surface of Neighbouring Fibre, $\mu = 0.75$

### 7.2.3 $\mu = 0.25$

The first case tested using a lower coefficient of friction than the control case is the $\mu = 0.25$ case. Looking at Figure 56, the maximum $G$ value has increased to approximately 170 J/m$^2$ (up from 90 J/m$^2$ for the control case). Focusing on Figure 56b, it can be seen that the crack tip is finally relieved fully in the unloading step, with the $G$ curve flattening out and approaching zero.

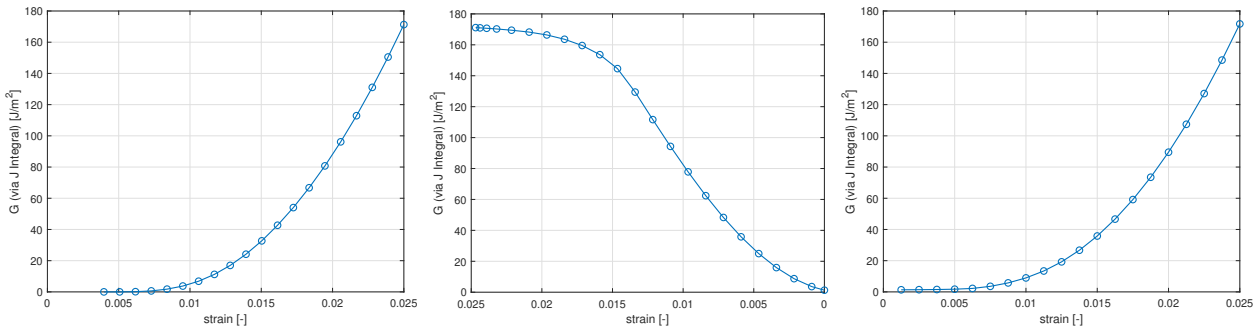


(a) Initial Loading Step (b) Unloading Step (c) Reloading Step

Figure 56: Energy Release Rate vs. Strain, $\mu = 0.25$

The maximum stress in the neighbouring fibre with respect to strain, however, still looks quite similar, as shown in Figure 57. Even with $\mu = 0.25$, maximum stress in the neighbour occurs at the top of the fibre for lower strain values.

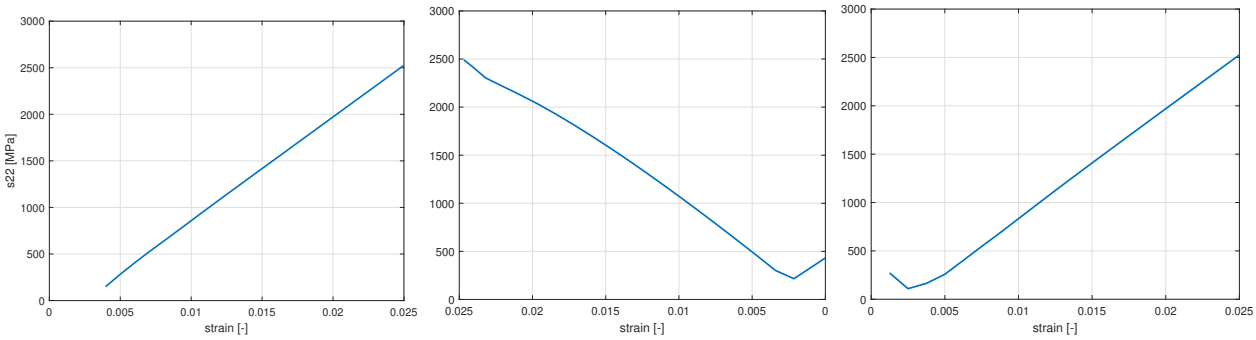


(a) Initial Loading Step (b) Unloading Step (c) Reloading Step

Figure 57: Max. S22 (Absolute Value) in Neighbouring Fibre vs. Strain, $\mu = 0.25$

However, once strain reaches $2.28 \times 10^{-2}$, the location of maximum strain shifts from the top of the fibre to near the midpoint of the fibre, close to the debond crack tip, as is shown in Figure 58. If the neighbouring fibre were to contain flaws that would form a crack when exposed to axial stress values exceeding 2000 MPa, it would be expected that under these conditions, failure of this fibre would occur not at the location of fracture of the broken fibre, but at the location of the debond crack tip.

The above result is crucial in understanding why fibre-to-fibre failure progression has been observed to occur not in a straight line, but along a zigzag path. While the $\mu = 0.25$ case is the first to produce such a result, upon decreasing the coefficient of friction further, the importance of the stress concentration near the debond crack tip is only amplified.

It can also be noticed that as $\mu$ decreases, the spike in S22 near the crack tip appears at lower and lower strain increments. This result is evidence that full slip is reached earlier for lower coefficients of friction.

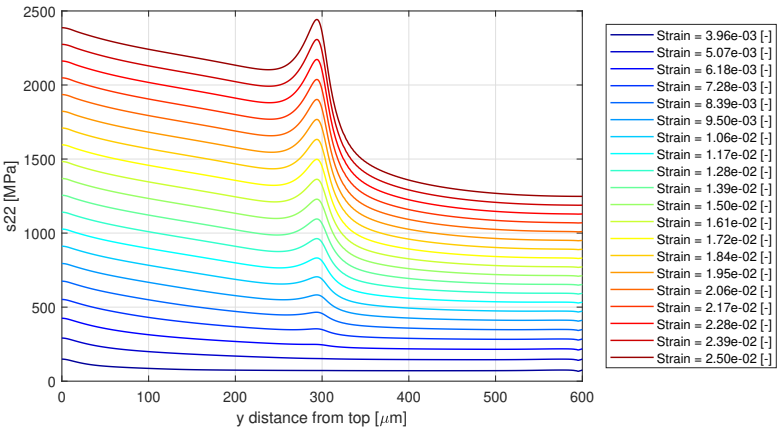


(a) Initial Loading Step

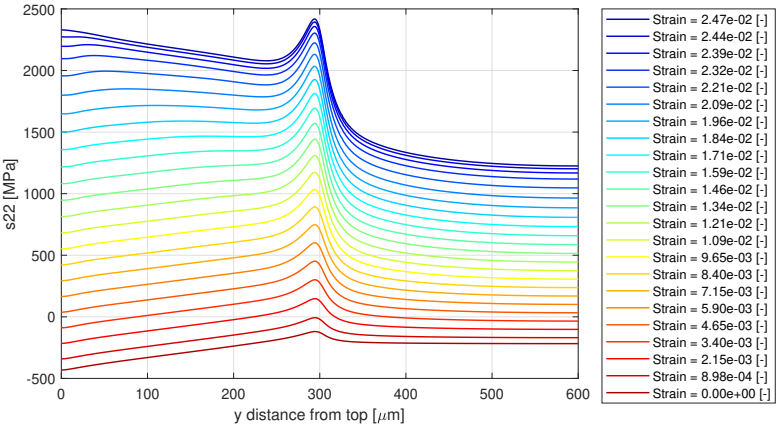


(b) Unloading Step

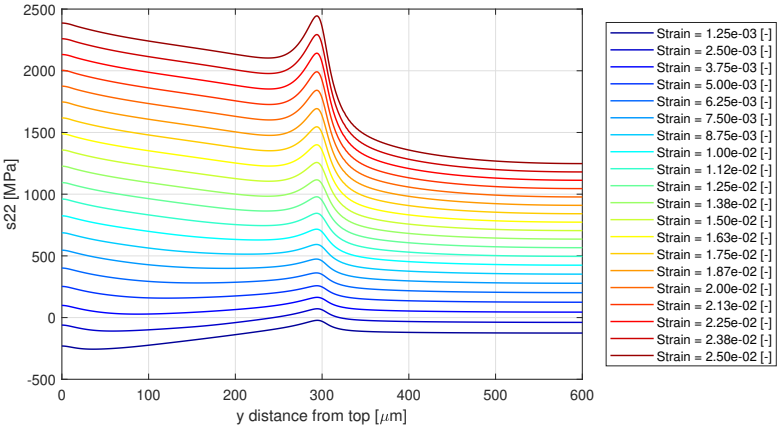


(c) Reloading Step

Figure 58: S22 at Surface of Neighbouring Fibre, $\mu = 0.25$

### 7.2.4 $\mu = 0.10$

The $\mu = 0.10$ case was the lowest-friction case tested, except for the frictionless case, which would not occur in reality. Therefore, the behaviour of the model with $\mu = 0.10$ will be presented in more detail, as it is noticeably different than the behaviour of the $\mu = 0.50$ case.

Figure 59 shows the interfacial slipping along the debond interface for the $\mu = 0.10$ case. It can immediately be seen that compared to the control case, full slip is reached much sooner when $\mu = 0.10$, occurring around the third increment in Figure 59a. Focusing on Figure 59b, it is observed that there is much less sticking during unloading, as the lower curves do not bunch together until they approach the crack tip. Also, compared to the control case, the magnitude of the maximum slip is higher for the $\mu = 0.10$ case.

The positive CSLIP2 values seen in Figures Figure 59b and Figure 59c represent the end of the fibre pushing out of the matrix at the broken end. This behaviour is a result of the thermal loading and the imposition of zero strain at the end of the unloading step, as is illustrated in Figure 46. Of course, in reality, this positive slip could not occur, as the broken fibre face would come into contact with the opposing broken fibre face when subjected to compression.

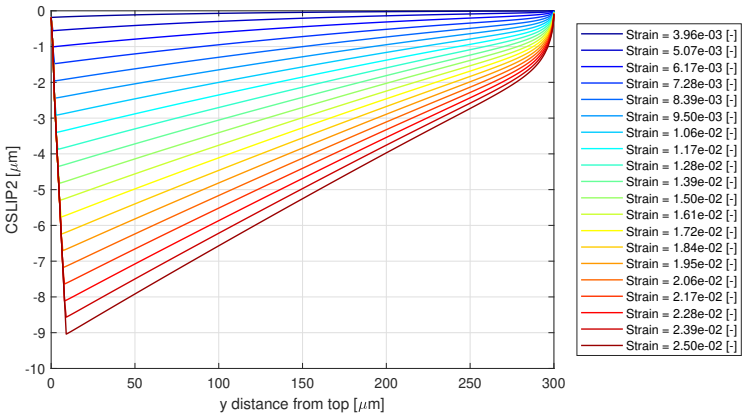


(a) Initial Loading Step

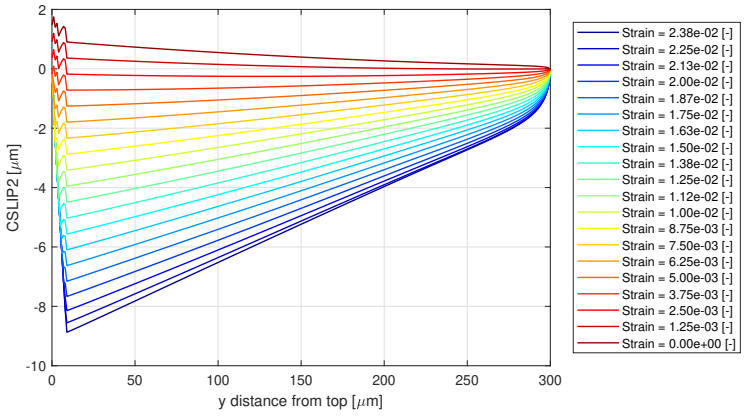


(b) Unloading Step

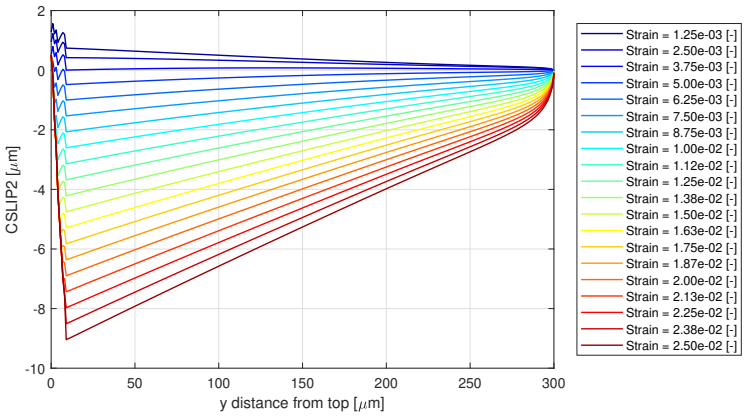


(c) Reloading Step

Figure 59: Interfacial Slipping Along Debond Interface, $\mu = 0.10$

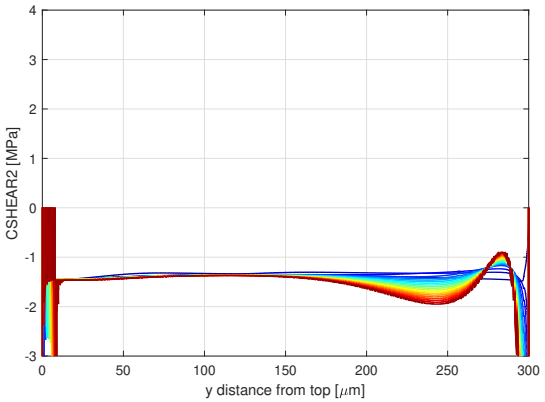


(a) Initial Loading Step

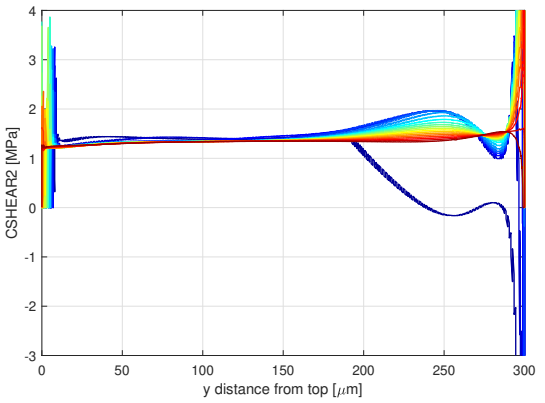


(b) Unloading Step

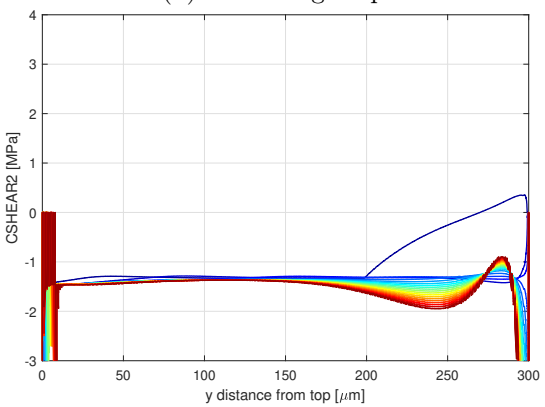


(c) Reloading Step

Figure 60: Shear Stress Along Debond Interface, $\mu = 0.10$

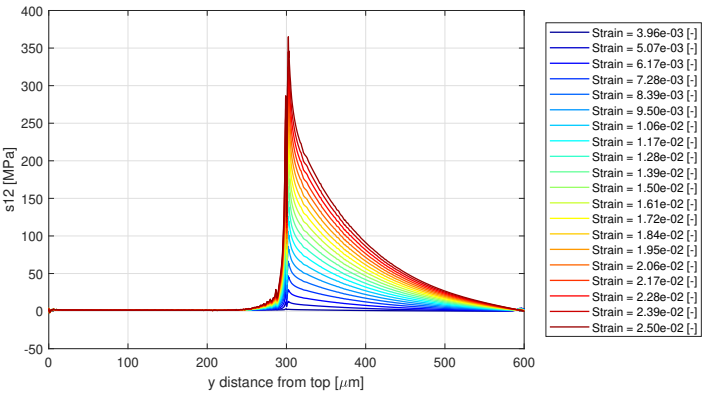


(a) Initial Loading Step

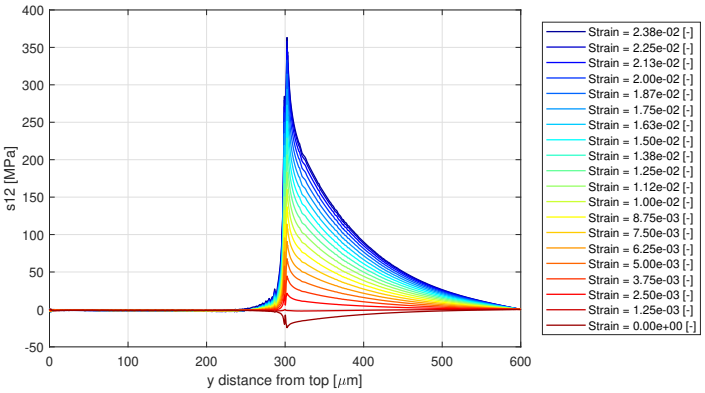


(b) Unloading Step

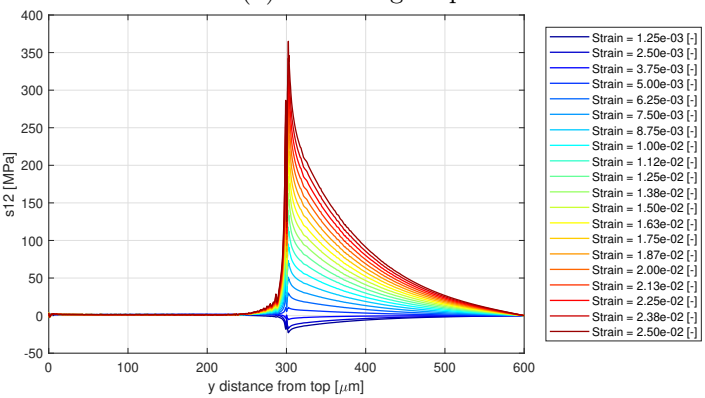


(c) Reloading Step

Figure 61: Broken Fibre Shear Stress Through Outer Path, $\mu = 0.10$, Full View

Figure 60 shows the frictional shear stress along the debond interface for the $\mu = 0.10$ case. In Figure 60a, it can again be seen that full slip is achieved early in the loading step. The small magnitude of the slipping friction is also apparent. In Figure 60b, the lack of much reverse sticking is evident, with only one increment's CSHEAR2 curve deviating from the group of slipping curves.

Figure 61 shows S12 in the outer portion of the broken fibre along the entire length. The dramatic spike in S12 values that was observed in Figure 37 is again observed here, but it is even more prominent in this case. When $\mu = 0.10$, S12 in the fibre exceeds 350 MPa, but in the control case, it remains below 250 MPa. The negative values seen in Figures 61b and 61c are results of the compression applied at the end of the unloading step, which has been discussed already. For comparison with Figure 60, the cropped version of Figure 61 is provided in appendix B.4 as Figure 106.

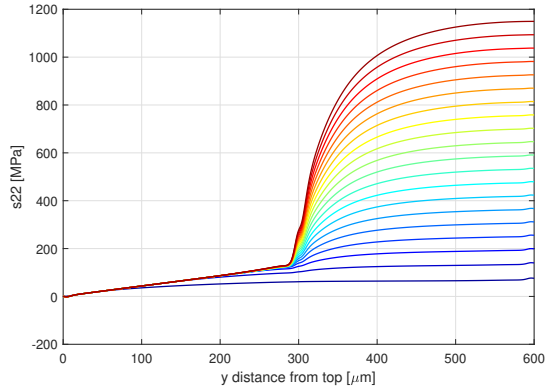


(a) Initial Loading Step

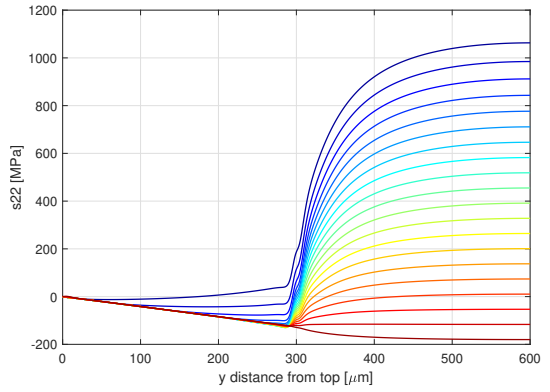


(b) Unloading Step

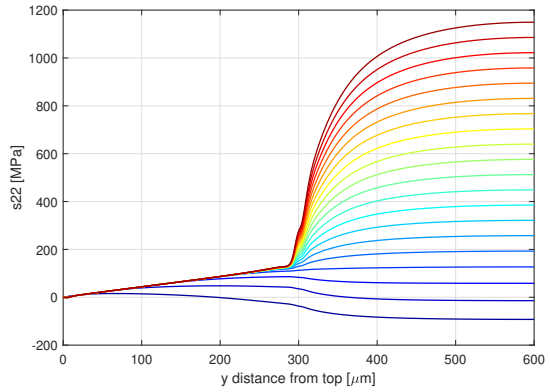


(c) Reloading Step

Figure 62: Broken Fibre S22 Through Centre Path, $\mu = 0.10$

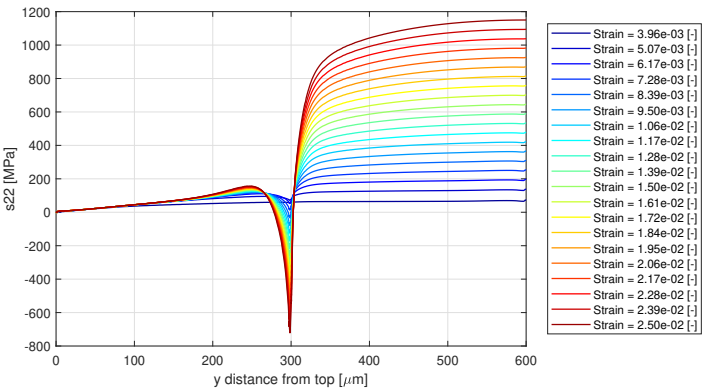


(a) Initial Loading Step

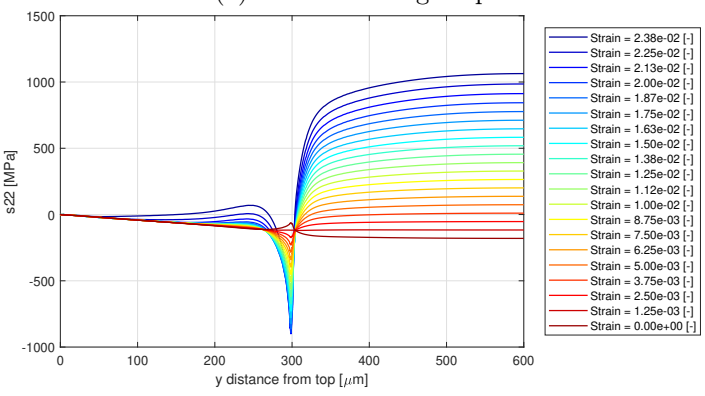


(b) Unloading Step

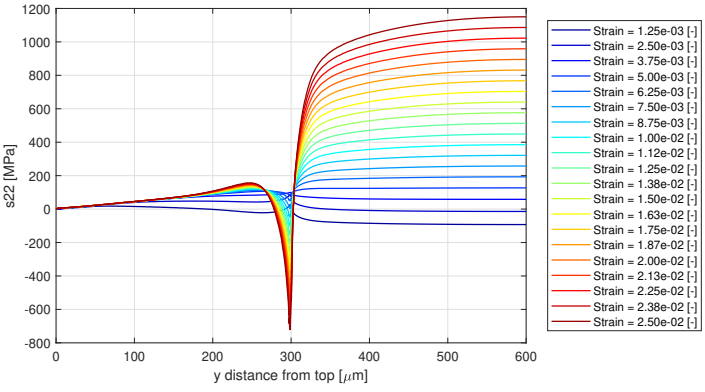


(c) Reloading Step

Figure 63: Broken Fibre S22 Through Outer Path, $\mu = 0.10$

Figures 62 and 63 show the axial stress in the broken fibre along the centre and outer paths, respectively, for the $\mu = 0.10$ case. Looking at Figure 62, it is clearly apparent that compared to the control case, there is much less frictional stress transfer and much more stress transfer at the crack tip, with S22 increasing rapidly as the y-distance approaches 300 $\mu$m.

Focusing on Figure 63, a negative spike in S22 is observed that is significantly more prominent than the spike in Figure 39. Here, the localised compression is enough to overcome the general tension in the fibre, leading to compressive forces in the region of 700 MPa, highlighting the strong influence of the crack tip stress field.

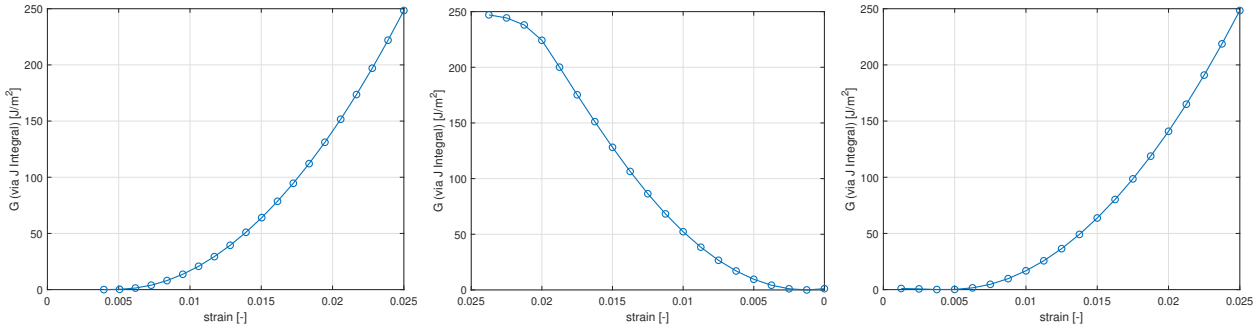


(a) Initial Loading Step (b) Unloading Step (c) Reloading Step

Figure 64: Energy Release Rate vs. Strain, $\mu = 0.10$

In Figure 64, it is evident that the crack tip is fully relieved during the unloading step. In fact, $G$ starts to increase slightly at the end of the unloading step; this is due to the applied compression at the end of this step.

Moving on to the neighbouring fibre, the maximum S22 plots given in Figure 65 still do not look much different from the previous cases, even though, as will be shown in Figure 66, the maximum S22 is occurring near the crack tip for more than half of the loading increments. Evidently, the dominance of S22 near the fibre fracture location for low loading values and the dominance of S22 near the crack tip for higher loading values both fall onto a generally linear trend, with the maximum S22 generally increasing as a linear function of strain. The more important result, then, is the location at which the maximum stress occurs.

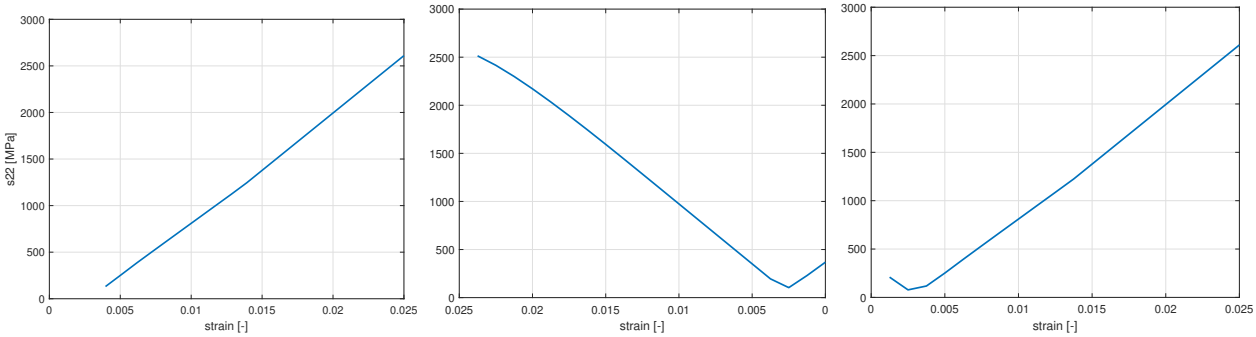


(a) Initial Loading Step (b) Unloading Step (c) Reloading Step

Figure 65: Max. S22 (Absolute Value) in Neighbouring Fibre vs. Strain, $\mu = 0.10$

When looking at Figure 66, the influence of the debond crack tip on the neighbouring fibre becomes clear, with the highest stress values occurring near the crack tip for the majority of increments. Similarly, in Figure 67, the effects of the debond crack tip stress field are clearly visible, although, as mentioned in section 7.1, the high S12 values seen in the figure are more relevant to matrix failure than fibre failure.

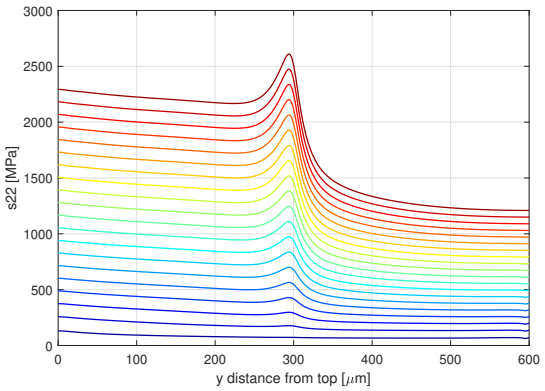


(a) Initial Loading Step

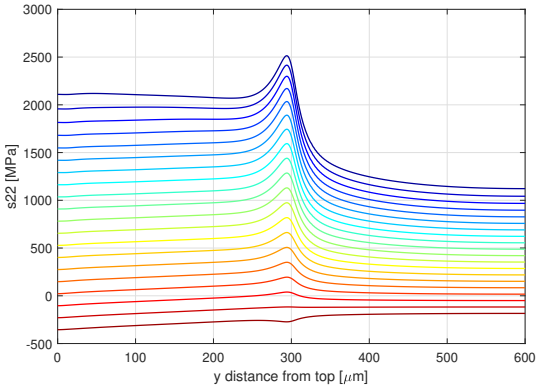


(b) Unloading Step

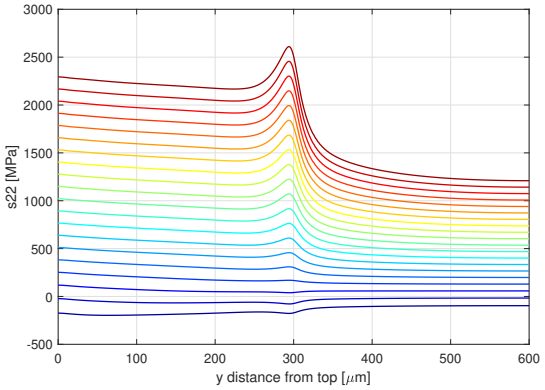


(c) Reloading Step

Figure 66: S22 at Surface of Neighbouring Fibre, $\mu = 0.10$

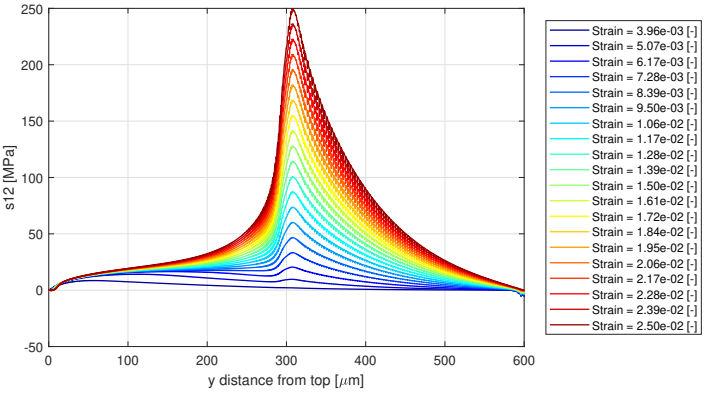


(a) Initial Loading Step

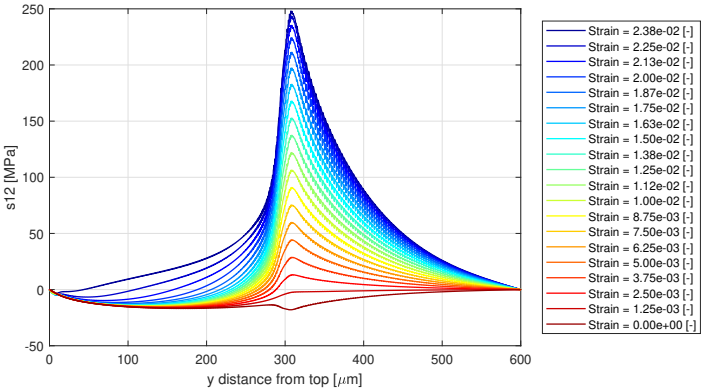


(b) Unloading Step

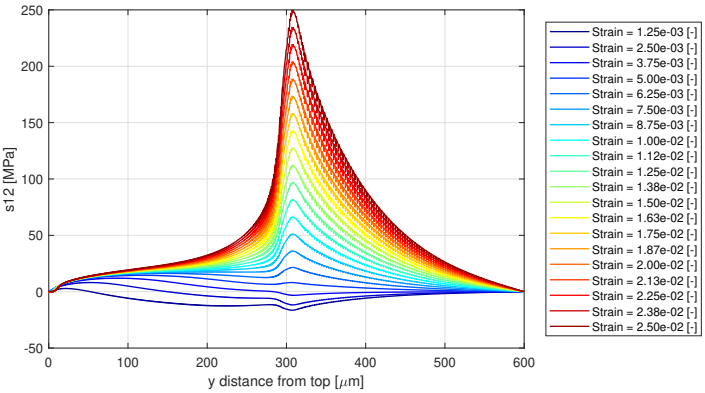


(c) Reloading Step

Figure 67: S12 at Surface of Neighbouring Fibre, $\mu = 0.10$

Figure 68 gives S22 in the neighbouring fibre in the debond crack tip plane (y-distance of 300 $\mu$m) along the circular path defined in Figure 44. When comparing it to Figure 43, Figure 68 suggests a stronger influence of the debond crack tip stress field, with a higher maximum S22 and a steeper decrease in S22 after 30°. This result aligns with the trend observed in Figure 66. The constant S22 values seen below 30° in Figure 43 are again observed here, suggesting that the neighbouring fibre is still being influenced by two debond crack tip stress fields.

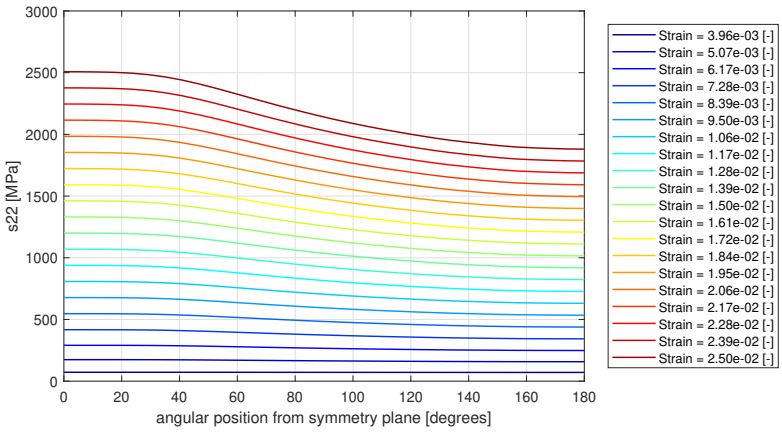


(a) Initial Loading Step

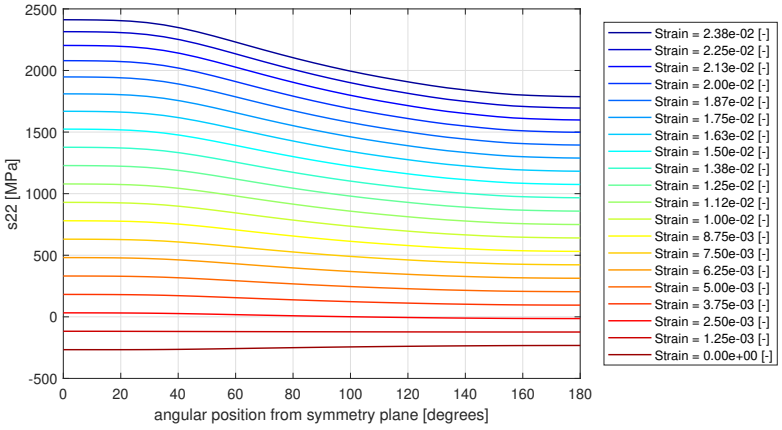


(b) Unloading Step

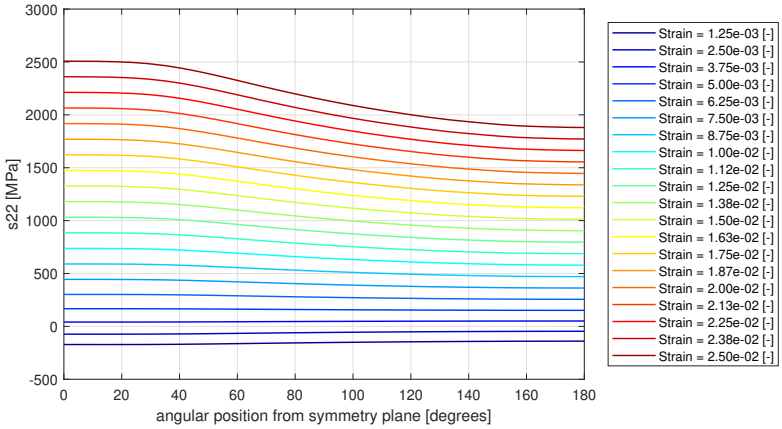


(c) Reloading Step

Figure 68: S22 Along Perimeter of Neighbouring Fibre Cross Section, $\mu = 0.10$

The stress in the fibre induced by the debond crack tip stress field $\hat{\sigma}_f^K$ was calculated for each increment of the initial loading step for the $\mu = 0.10$ case by subtracting the upstream S22 value from the peak S22 value in the vicinity of the debond crack tip plane. The resulting values were plotted as a function of the crack tip energy release rate, and the resulting curve was compared with the corresponding curve generated by plugging the same energy release rate values into Equation 1 from Sørensen and Goutianos [7]. These two curves are given below in Figure 69.

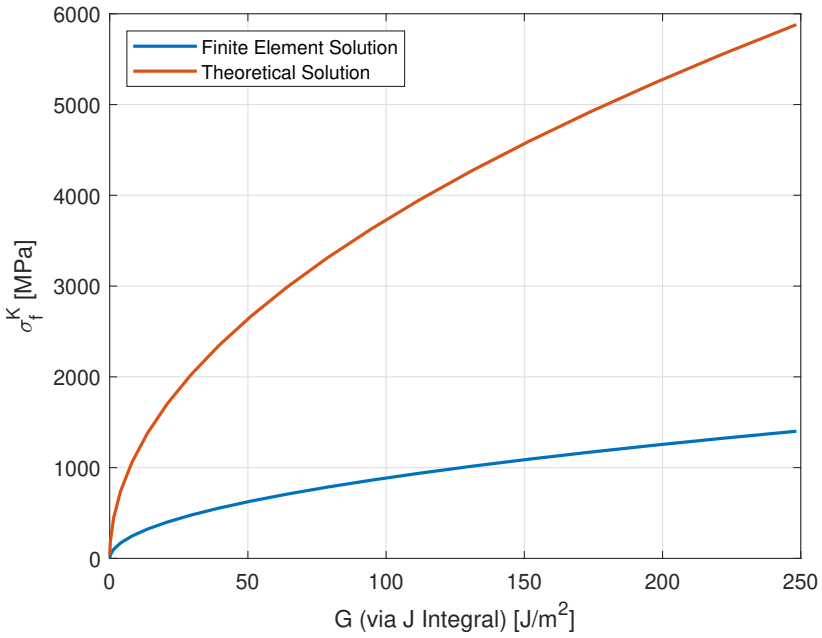


Figure 69: Induced Stress in the Neighbouring Fibre Due to the Debond Crack Tip Stress Field as a Function of the Energy Release Rate in the Broken Fibre for the $\mu = 0.10$ Case, Comparison with Theoretical Solution

As can be seen in Figure 69, the two curves do not show good agreement. However, the shapes of the curves are nearly identical. It was found that by applying a factor of 0.2382 to Equation 1, the resulting curve matches the finite element curve almost perfectly. This result suggests that Equation 1 might be inaccurate.

### 7.2.5 $\mu = 0.00$ (Frictionless Case)

Although it is impossible in reality, a frictionless case was simulated in order to determine the limits to which reducing friction can increase the stress concentration on the neighbouring fibre. In Figure 70, the lack of any sticking friction is indicated by the smooth parabolic shape of the curves, with Figure 70 showing immediate decline in $G$ after the first step.

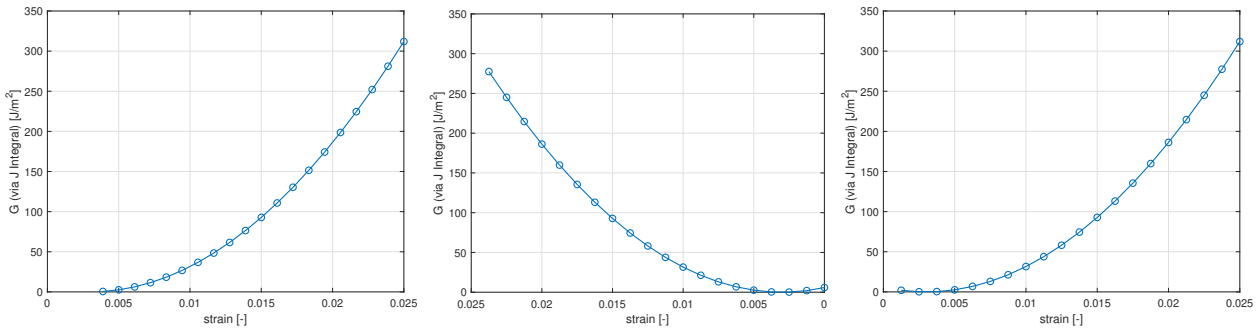


(a) Initial Loading Step (b) Unloading Step (c) Reloading Step

Figure 70: Energy Release Rate vs. Strain, $\mu = 0.00$

While the plot of the maximum S22 in the neighbour with respect to strain looks similar to the other cases, it can be seen in Figure 71 that in the frictionless case, the curves are perfectly straight. This result makes sense, since for this case, the crack tip stress field is the dominant factor for every loading increment, and the system behaves in a completely linear-elastic manner in the absence of friction.

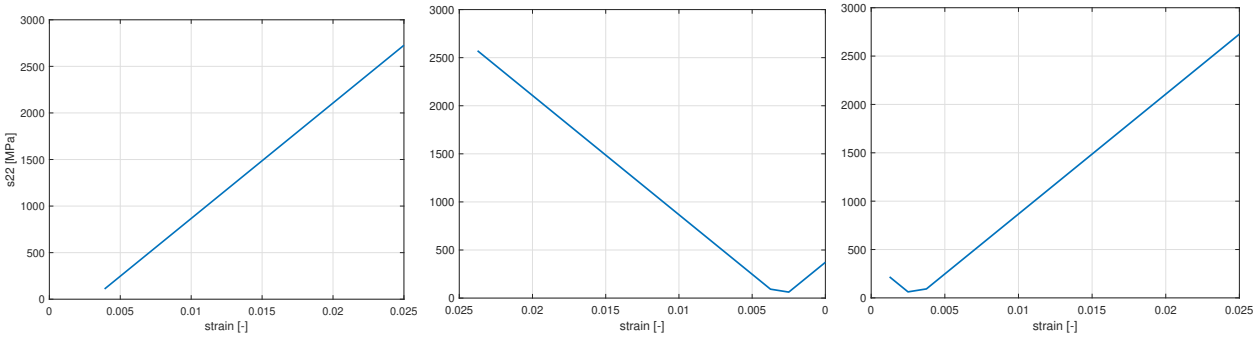


(a) Initial Loading Step (b) Unloading Step (c) Reloading Step

Figure 71: Max. S22 (Absolute Value) in Neighbouring Fibre vs. Strain, $\mu = 0.00$

Focusing on Figure 72, the frictionless nature of the simulation is evidenced by the perfectly flat slope of the curves downstream of the crack tip, as there is no stress transfer from matrix to fibre throughout the debonded region. Furthermore, the three loading steps have identical S22 curves for any given strain value, which means that there is no sticking.

Compared to the $\mu = 0.10$ case, the maximum S22 value in the neighbouring fibre is higher in the frictionless case for a given strain value. The same is true when holding upstream stress values constant. This result alone is enough to validate the premise that erosion of asperities along the debond interface could induce fracture of neighbouring fibres, and that that fracture would occur near the debond crack tip.

While the $\mu = 1.00$ produced a higher S22 value in the neighbouring fibre for a given strain, the same is not true when keeping upstream stress constant, as was shown in Figure 47. Furthermore, it is plausible that the system would never experience frictional forces as high as were present in the $\mu = 1.00$ case, even before onset of asperity erosion.

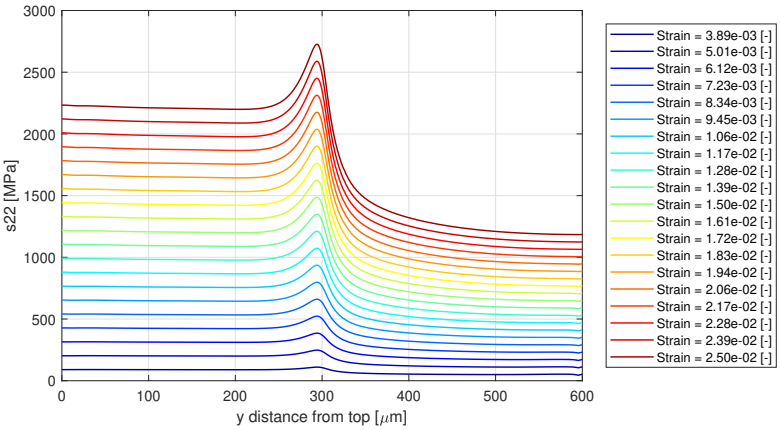


(a) Initial Loading Step

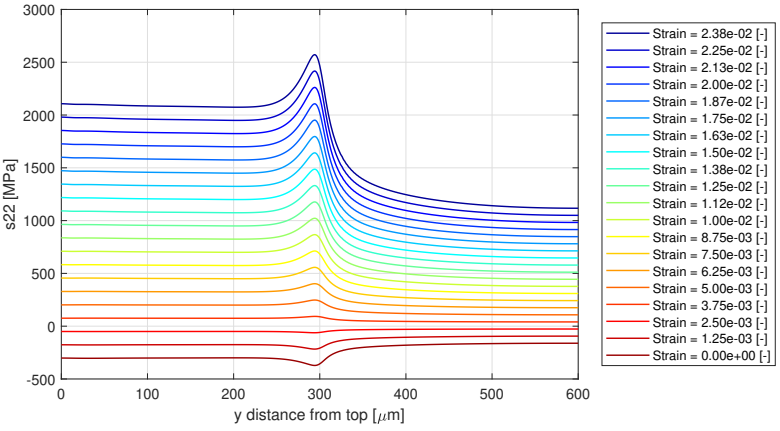


(b) Unloading Step

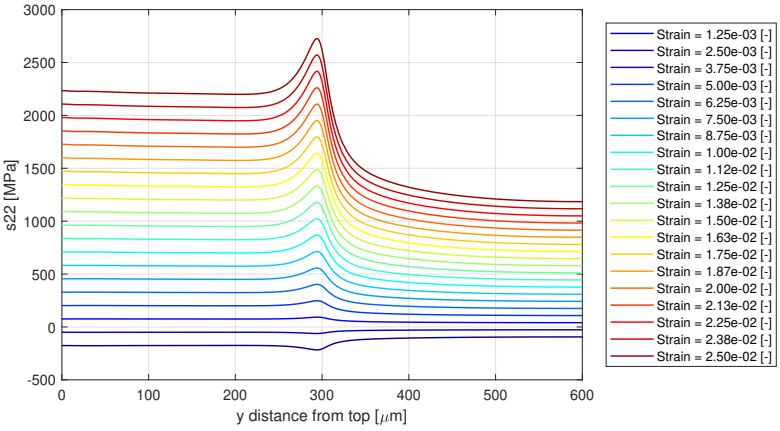


(c) Reloading Step

Figure 72: S22 at Surface of Neighbouring Fibre, $\mu = 0.00$

## 7.3 Varying the Fibre Volume Fraction

In addition to investigating the influence of debond interface friction, the influence of fibre volume fraction was also explored. The control case, as well as the other friction variation cases, used 55% fibre packing, which is typical for wind turbine blade applications. The other fibre volume fractions tested were 25%, 40%, and 70%, with each of these three simulations using a coefficient of friction of 0.50, as in the control case. The plots left out of this section are included in Appendix C.

As when varying the coefficient of friction, one S22 vs. y-distance curve was taken from each case for each loading step, and the four curves were plotted together. Again, the plotted increments were chosen so as to exhibit similar upstream stress values. The resulting plots are given below as Figures 73 through 75.

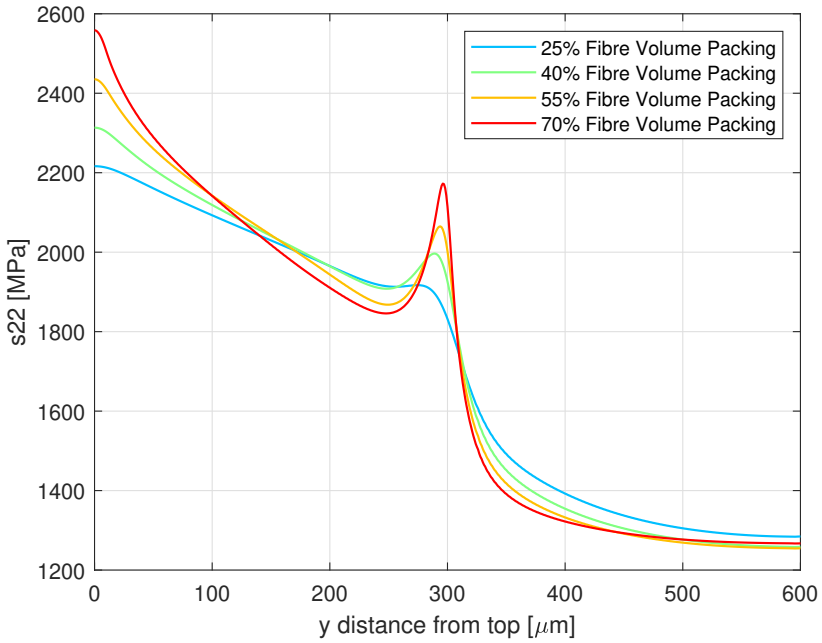


Figure 73: S22 at Surface of Neighbouring Fibre Under Various Fibre Volume Fractions, Initial Loading Step, $\mu = 0.50$

Examining Figures 73 through 75, it can be seen that for similar upstream stress values, the spike in S22 in the neighbouring fibre near the debond crack tip is more pronounced for higher fibre volume fractions. This result makes sense, as the neighbouring fibre is closer to the debond crack for higher volume fractions.

Focusing on Figure 74, the shape of the S22 curve varies between the cases, with the 70% packing case curve flattening out between an initial steep upward slope and the spike near the crack tip, suggesting that the small inter-fibre distances in this case lead to more complex interactions between fibres.

Although the maximum stress in the neighbouring fibre does not occur near the debond crack tip for any of the cases simulated in this section, the trends observed would be expected to continue were the coefficient of friction to decrease from 0.50.

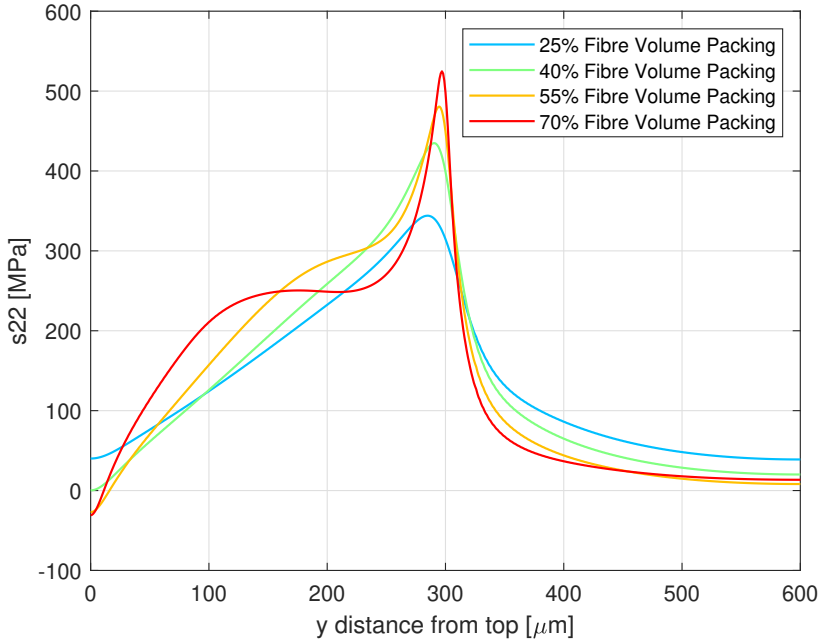


Figure 74: S22 at Surface of Neighbouring Fibre Under Various Fibre Volume Fractions, Unloading Step, $\mu = 0.50$

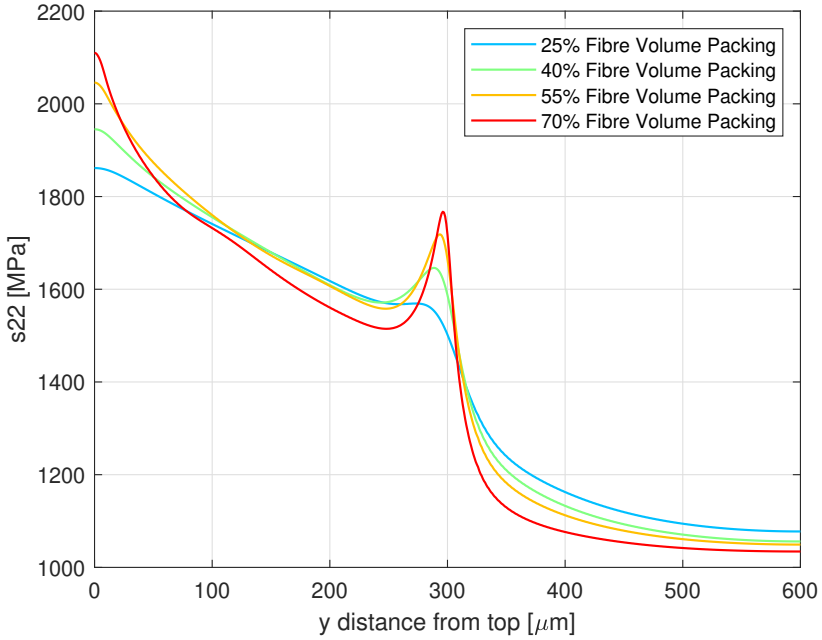


Figure 75: S22 at Surface of Neighbouring Fibre Under Various Fibre Volume Fractions, Reloading Step, $\mu = 0.50$

### 7.3.1 25% Packing

The lowest fibre volume fraction simulated was 25%. In this simulation, the neighbouring fibre appears to be far enough away from the debond crack so as to significantly attenuate the effects of the debond crack tip stress field, as is evidenced by the small height of the S22 spikes near 300 $\mu$m y-distance in Figure 76.

Furthermore, it is observed that the slope of the S22 curve to the right of the debond crack tip is rather shallow when compared to the other packing cases, with the stress in the fibre taking a greater distance to reach its far-upstream value. Such a result could suggest that while the crack tip stress field is less intense in this case than for the others, it extends over a greater distance.

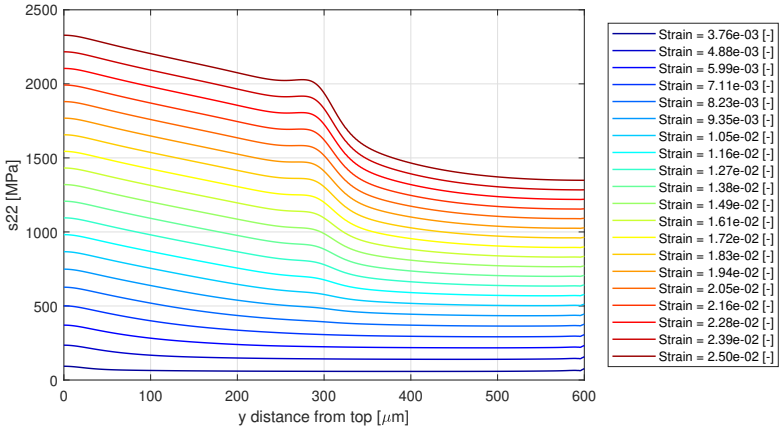


(a) Initial Loading Step

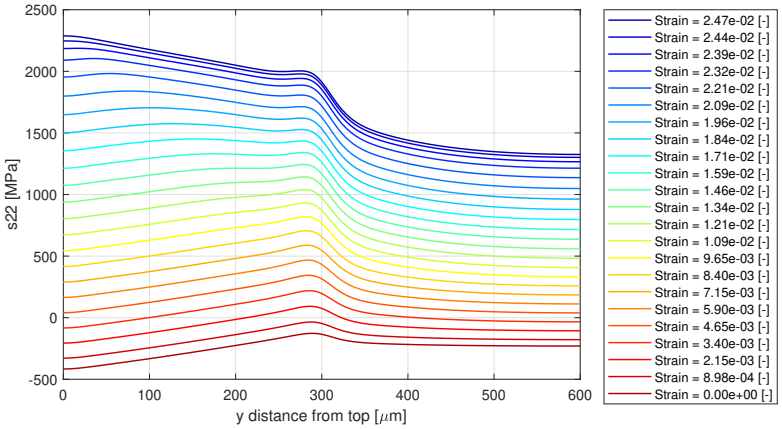


(b) Unloading Step

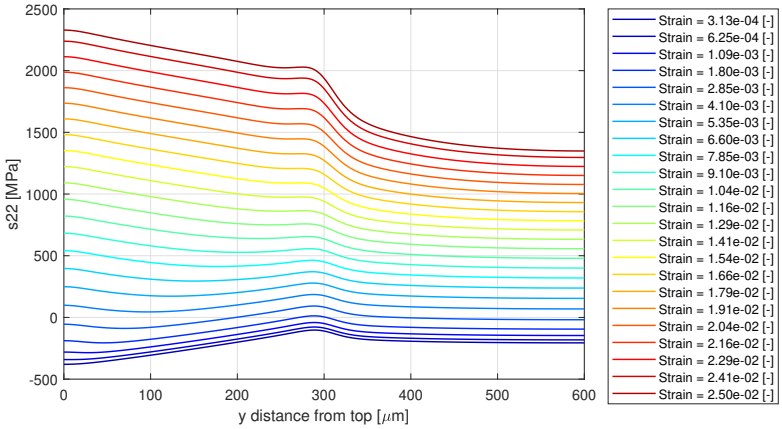


(c) Reloading Step

Figure 76: S22 at Surface of Neighbouring Fibre, 25% Packing

### 7.3.2 40% Packing

The second-lowest fibre volume fraction simulated was 40%. The results for this case look highly similar to the results from the 55% packing control case. The spikes near the crack tip seen in Figure 77 are slightly lower than they was for the control case, but they still exceed the height of the spikes seen in the 25% packing case.

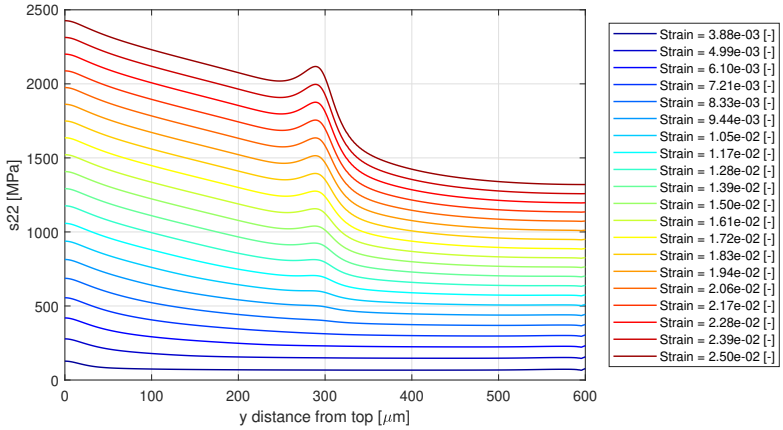


(a) Initial Loading Step

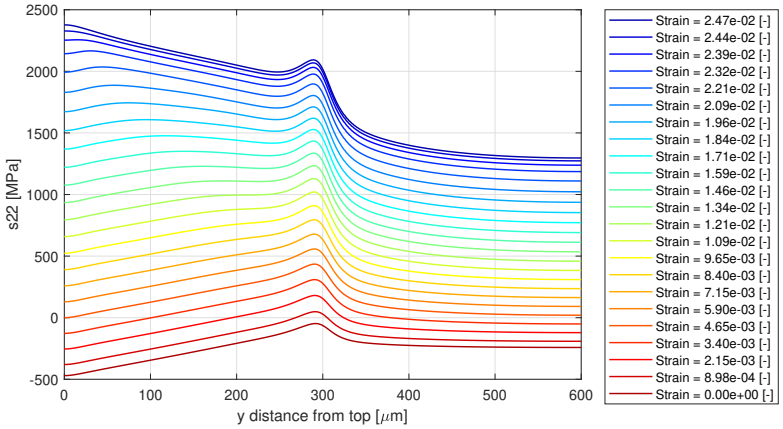


(b) Unloading Step

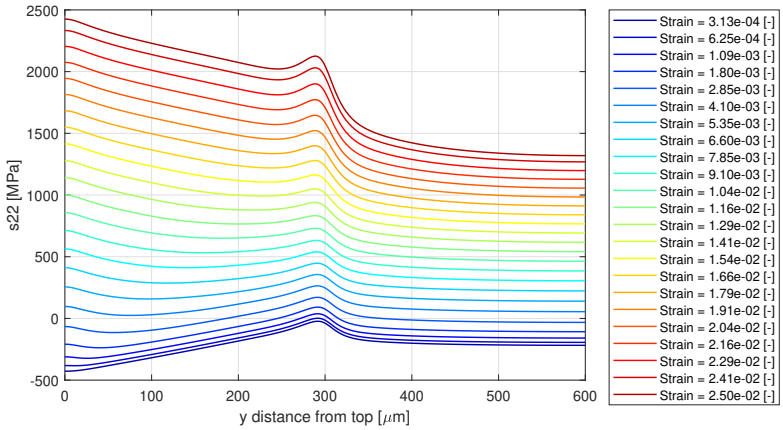


(c) Reloading Step

Figure 77: S22 at Surface of Neighbouring Fibre, 40% Packing

### 7.3.3 70% Packing

The highest fibre volume fraction tested was 70%, which is near the limit of feasible manufacturing capabilities. At this volume fraction, the influence of the debond crack tip stress field is pronounced and acute, with the S22 spikes seen in Figure 78 extending higher and occurring over a shorter distance than for the other volume fraction cases. However, the S22 spikes are still not as significant as they were in the 55% packing, $\mu = 0.25$ case, suggesting that fibre volume fraction is less important than friction in the debond zone when predicting fibre failure progression.

Another result that is observed in Figure 78 is that the maximum fibre stress downstream of the debond crack tip increases as fibre volume fraction increases, with the 70% simulation producing the only two increments to exceed 2500 MPa at any point along the fibre length for any of the $\mu = 0.50$ cases tested. This result is to be expected, as there is less matrix present to bear any of the load.

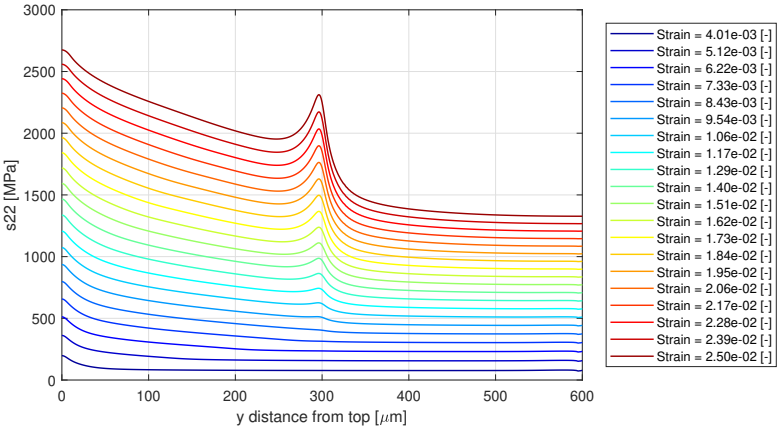


(a) Initial Loading Step

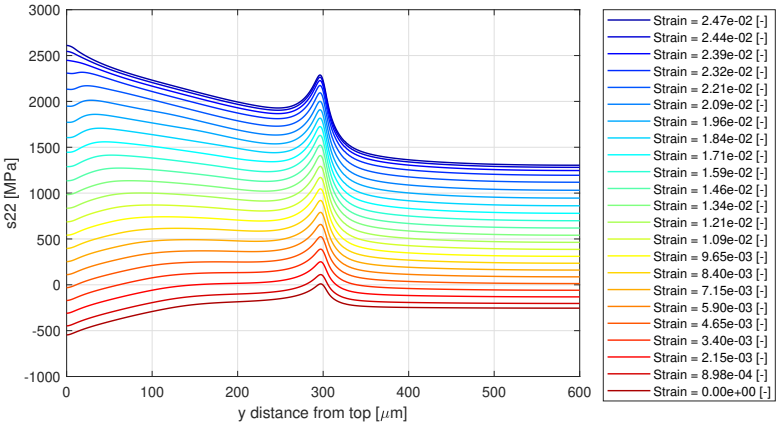


(b) Unloading Step

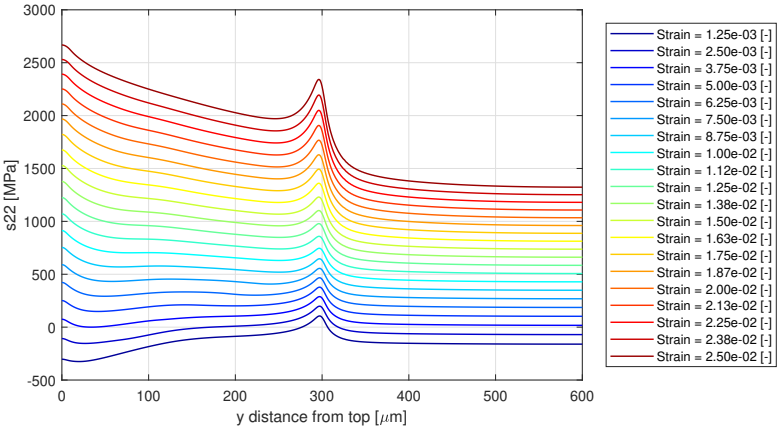


(c) Reloading Step

Figure 78: S22 at Surface of Neighbouring Fibre, 70% Packing

Another notable result from the 70% fibre volume packing case was that it was the only case tested that shows the maximum stress in the neighbouring fibre (in the debond crack tip plane) occurring at an angle of 30° from the symmetry plane, which is the closest point to the debond crack tip. This behaviour can be clearly seen in Figure 79.

This result highlights the more acute influence of the debond crack tip stress field on the neighbouring fibre that was also observed in Figure 78. Interestingly, a similar peak at 30° was not observed for the $\mu = 0.10$ case, as can be seen in Figure 68, nor was one observed for the frictionless case. These observations suggest that the influence of the debond crack tip is more dispersed, regardless of friction, except for very high fibre volume fractions.

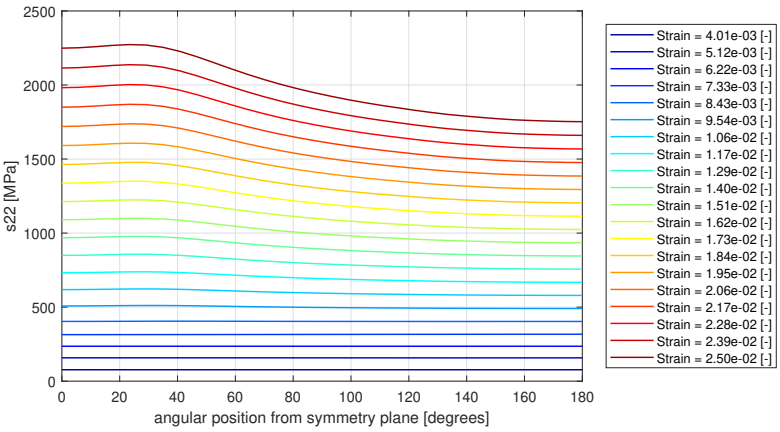


(a) Initial Loading Step

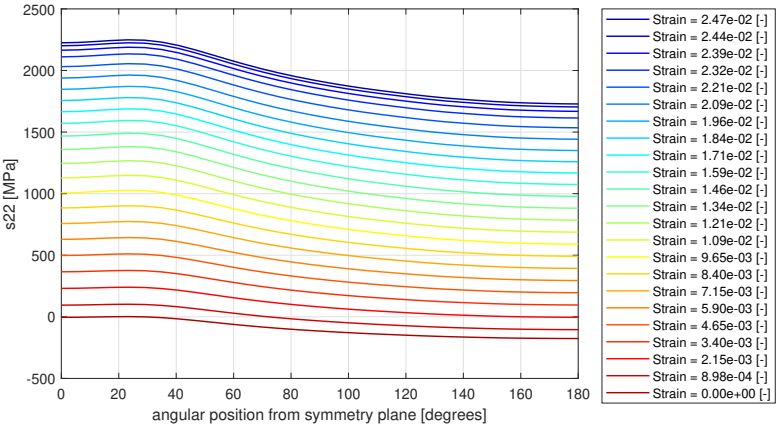


(b) Unloading Step

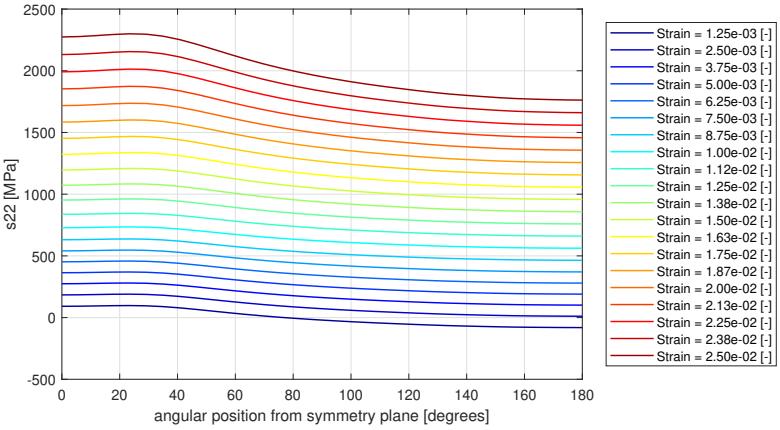


(c) Reloading Step

Figure 79: S22 Along Perimeter of Neighbouring Fibre Cross Section, 70% Packing

# 8 Discussion of Results

The finite element modelling undertaken for this thesis project effectively demonstrates the mechanisms by which a reduction in the coefficient of friction on the interface between a partially debonded fibre and the surrounding matrix can lead to an increase in the crack tip energy release rate, causing a stress field to form around the crack tip that can potentially induce fracture in neighbouring fibres. Assuming that repeated forward and reverse slipping can cause erosion of the asperities along the debond interface, the model built here successfully explains the phenomenon of successive fibre breaks occurring in different planes as well as the large number of cycles in between successive fibre failures.

## 8.1 Answers to Research Questions

This thesis project has successfully identified answers to the research questions posed in chapter 3. The first question was: **How does debonding of a broken fibre affect the stress field in a neighbouring fibre?** While the debond length was not varied in the simulations, since shorter debond lengths produce the same effects as higher loading and vice versa, the incrementation of the simulations allowed for illustration of the fact that shorter debond lengths will lead to increased stress on the neighbouring fibre. Essentially, a shorter debond length allows for less load transfer between the fibre and matrix to occur via friction, meaning that more load transfer will have to occur at the debond crack tip, resulting in higher energy release rates. The effect of fibre spacing was explored, with higher volume fractions producing more intense and more acute stress fields on neighbouring fibres. The effects of interfacial friction were identified, with lower friction values corresponding to greater stress concentrations in neighbouring fibres.

A notable result was Figure 69, which shows that the finite element model's results for the debond crack tip energy release rate's effect on the stress field in neighbouring fibres does not match the theoretical relationship proposed by Sørensen and Goutianos [7]. This result suggests a potential inaccuracy in Equation 1, but it should be noted that the model's treatment of inter-fibre stress transfer was not directly validated, as the finite element model validation was performed using the single-fibre model. The discrepancy shown in Figure 69 warrants further investigation.

The second question was: **What is the criterion for failure of a neighbouring fibre?** The presence of stress concentrations near the debond crack tip explains why successive fractures of fibres often occur in different planes, as neighbouring fibres are likely to fail in the plane of the debond crack tip rather than the plane of the original fibre fracture. However, the results for cases with high frictional forces show that in some instances, fracture of neighbouring fibres could also occur in the same plane as the original fracture. The large number of cycles between fibre failures is explained by the need for erosion to occur before stress fields will reach critical magnitudes.

The third and final question posed was: **How does the mechanism of friction reduction through asperity erosion affect the debond length?** While debond crack growth was not directly simulated, the reduction of interfacial friction was clearly shown to increase the debond crack tip energy release rate, suggesting that asperity erosion can lead to debond crack growth. Furthermore, it was observed that in cases where full slip is not achieved and sticking friction is present, the crack tip energy release rate remains very small in value, suggesting crack growth arrest. An extension of this project could attempt to use the Two-Step Crack Closure Method to directly model debond crack growth.

## 8.2 Potential Sources of Error

For the single-fibre model, realistic thermal conditions were initially applied to simulate the thermal loading seen in the composite manufacturing process. However, these conditions did not yield clear results for the parameters of interest. Consequently, a simplified approach was adopted by applying thermal expansion directly to the fibre to highlight the relevant results.

Upon transitioning to the multi-fibre model, significantly higher shear forces were observed. Additionally, a greater displacement was required to achieve full slip compared to the single-fibre model. Notably, only the $\mu = 0.1$ case and the frictionless case produced results where the highest axial stress in the neighbouring fibre occurred at the debond crack tip rather than at the fibre fracture location. The applied thermal expansion likely led to higher frictional forces than typically expected for a given coefficient of friction along the interface.

The single-fibre model was laterally unconstrained, with only the matrix providing resistance to the fibre's expansion, thus generating a normal force which in turn produced a frictional force. The multi-fibre model, however, had zero-lateral-displacement boundary conditions imposed on all four lateral faces. Consequently, while the contact pressing stress between the fibre and matrix in the single-fibre model was approximately 8.3 MPa, the pressing stress in the 55% packing multi-fibre model was close to 16.3 MPa.

Future work could focus on applying more realistic thermal conditions to the model to examine its behaviour at specific coefficients of friction. The coefficients of friction used in this study were somewhat arbitrary due to the excessive thermal expansion applied to the fibre. Alternatively, future research could involve testing a range of coefficients of friction closer to 0.10.

Another inaccuracy in the post processing was the failure to capture data at the location of maximum stress in the neighbouring fibre for the 70% fibre volume packing vertical path plots. The neighbouring fibre vertical path plots for all of the simulation cases were generated at the 0° position as defined in Figure 44. This path choice was likely sufficient to capture the maximum stress for most of the cases tested, as the circular path plots showed that the region of maximum stress included the 0° position. However, for the 70% packing case, the maximum stress occurred at the 30° position, as shown in Figure 79. The S22 peaks seen in Figure 78 would likely be more pronounced were the vertical path to be defined at the 30° position for that case.

Despite these challenges, the project provides valuable insights into the evolution of fatigue damage progression and how debond cracks can affect stress concentration on neighbouring fibres.

# 9 Conclusion

In this thesis, fatigue damage progression was investigated through advanced modelling at the fibre scale via an Abaqus finite element model in order to explore how the presence of a fibre-matrix debond crack affects stress concentrations in adjacent fibres over successive loading, unloading, and reloading cycles. The influence of varying friction coefficients at the fibre-matrix interface and varying fibre volume fractions on these stress fields was tested through the simulation of nine cases in total. This research aims to contribute significant insights into the mechanics of composite materials, particularly in understanding the complex interactions that govern fibre-matrix debonding and frictional sliding.

In chapter 2, a comprehensive literature review was presented, examining current research on fibre-matrix interactions and highlighting the opportunity for improved finite element models to increase understanding of progressive fibre failure in composite fatigue. In chapter 4, essential equations for the analytic validation of the finite element model were introduced, forming a robust theoretical basis for the simulations. Chapter 5 detailed the development of the single-fibre and multi-fibre models, specifying geometry, material properties, boundary conditions, and thermal loading conditions, along with mesh construction and simulation steps.

The single-fibre model results presented in chapter 6 demonstrated successful mesh convergence and validation with analytical solutions for single-fibre pull-out, while also verifying axial symmetry and checking for J-integral contour dependency. Chapter 7 presented the results from the nine simulation cases tested using the full multi-fibre model, exploring the effects of varying the coefficient of friction and fibre volume fraction and revealing complex interactions within the composite material. The finite element simulations showed how reducing the coefficient of friction at the fibre-matrix interface increases the crack tip energy release rate, creating a stress field and potentially inducing fractures in neighbouring fibres, and the variation in the location of the maximum stress in the neighbouring fibre depending on the coefficient of friction helps to explain observations of successive fibre breaks occurring in a zigzag manner. The research questions posed in chapter 3 were discussed and answered in chapter 8.

Further work could involve working to improve the physical accuracy of the thermal conditions imposed on the model, testing lower friction values to more clearly see the mechanisms of fibre failure progression. Further, the Two-Step Crack Closure Method could be employed to directly model debond crack growth. More easily, the existing simulation data could be post-processed again using y-direction evaluation paths that capture the behaviour in the neighbouring fibre at its closest point to the broken fibre, especially for high fibre volume fractions. Finally, an explanation for the discrepancy between the theoretical and model-derived curves in Figure 69 could be sought out through more robust validation of the stress transfer mechanisms in the finite element model as well as review of Equation 1.

Overall, this thesis represents a step forward in modelling fibre-matrix interactions within composite materials. The findings not only contribute to the theoretical knowledge but also have potential to improve the design and application of future materials. The insights gained from this study pave the way for future research and innovation in the field of composite materials.

# References


[1] B. F. Sørensen, S. Goutianos, L. P. Mikkelsen, and S. Fæster, "Fatigue damage growth and fatigue life of unidirectional composites," *Composites Science and Technology*, vol. 211, 7 2021.

[2] A. P. Vassilopoulos, "The history of fiber-reinforced polymer composite laminate fatigue," *International Journal of Fatigue*, vol. 134, 2020.

[3] E. K. Gamstedt and R. Talreja, "Fatigue damage mechanisms in unidirectional carbon-fibre-reinforced plastics," *Journal of Materials Science*, vol. 34, pp. 2535–2546, 1999.

[4] R. Talreja, "Fatigue of composite materials: damage mechanisms and fatigue-life diagrams," *Proceedings of The Royal Society of London, Series A: Mathematical and Physical Sciences*, vol. 378, pp. 461–475, 1981.

[5] P. W. J. Van Den Heuvel, T. Peijs, and R. J. Young, "Failure phenomena in two-dimensional multi-fibre microcomposites - 3. a raman spectroscopy study of the influence of interfacial debonding on stress concentrations," *Composites Science and Technology*, vol. 58, pp. 933–944, 1998.

[6] S. Goutianos and T. Peijs, "Fatigue damage mechanisms in carbon-epoxy multi-fibre model composites," *Advanced Composites Letters*, vol. 10, pp. 21–32, 2001.

[7] B. F. Sørensen and S. Goutianos, "Micromechanical model for prediction of the fatigue limit for unidirectional fibre composites," *Mechanics of Materials*, vol. 131, pp. 169–187, 4 2019.

[8] K. M. Jespersen and L. P. Mikkelsen, "Three dimensional fatigue damage evolution in non-crimp glass fibre fabric based composites used for wind turbine blades," *Composites Science and Technology*, vol. 153, pp. 261–272, 12 2017.

[9] P. W. J. Van Den Heuvel, M. K. Wubbolts, R. J. Young, and T. Peijs, "Failure phenomena in two-dimensional multi-fibre model composites: 5. a finite element study," *Composites Part A: Applied Science and Manufacturing*, vol. 29, pp. 1121–1135, 1 1998.

[10] C. Breite, A. Melnikov, A. Turon, A. B. de Morais, C. Le Bourlot, E. Maire, E. Schöberl, F. Otero, F. Mesquita, I. Sinclair, J. Costa, J. A. Mayugo, J. M. Guerrero, L. Gorbatikh, L. N. McCartney, M. Hajikazemi, M. Mehdikhani, M. N. Mavrogordato, P. P. Camanho, R. Tavares, S. M. Spearing, S. V. Lomov, S. Pimenta, W. V. Paepegem, and Y. Swolfs, "Detailed experimental validation and benchmarking of six models for longitudinal tensile failure of unidirectional composites," *Composite Structures*, vol. 279, 1 2022.

[11] L. Zhuang, A. Pupurs, J. Varna, and Z. Ayadi, "Fiber/matrix debond growth from fiber break in unidirectional composite with local hexagonal fiber clustering," *Composites Part B: Engineering*, vol. 101, pp. 124–131, 9 2016.

[12] B. Budiansky, J. W. Hutchinson, and A. G. Evans, "Matrix fracture in fiber-reinforced ceramics," *Journal of the Mechanics and Physics of Solids*, vol. 34, pp. 167–189, 1986.

[13] R. Krueger, "Virtual crack closure technique: History, approach, and applications," *Applied Mechanics Reviews*, vol. 57, pp. 109–143, 1 2004.

[14] J. R. Rice, "A path independent integral and the approximate analysis of strain concentration by notches and cracks," *Journal of Applied Mechanics, Transactions ASME*, vol. 35, pp. 379–386, 1968.

[15] J. W. Hutchinson and H. M. Jensen, "Models of fiber debonding and pullout in brittle composites with friction," *Mechanics of Materials*, vol. 9, pp. 139–163, 1990.

# A S22 Analytic Validation for All Increments

Figures 80 and 81 show the comparison of the single-fibre S22 results with the analytic solution for each loading increment, with the dotted lines representing the analytic solutions.

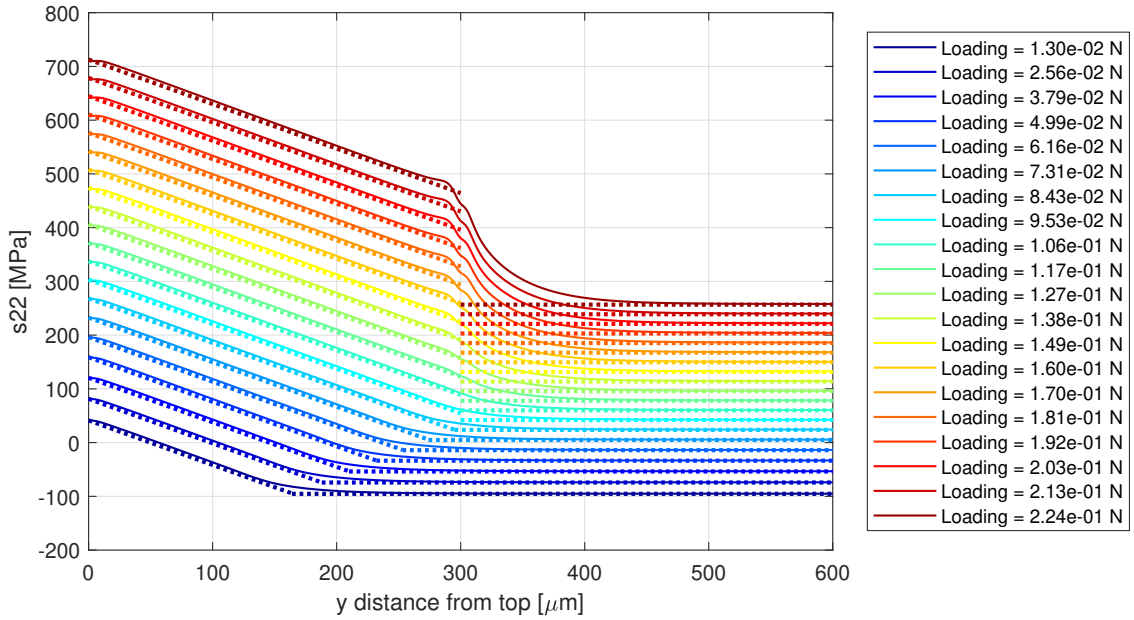


Figure 80: S22 Through Centre Path, Comparison with Analytic Solution, All Increments (Solid Lines Represent Finite Element Results, Dotted Lines Represent Analytic Solutions)

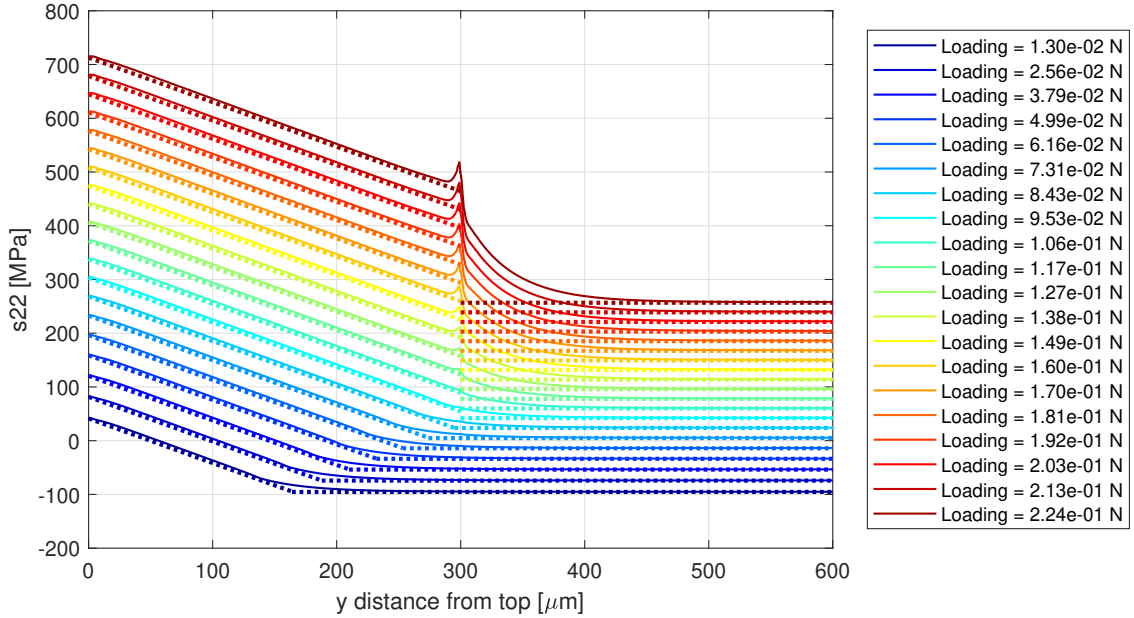


Figure 81: S22 Through Outer Path, Comparison with Analytic Solution, All Increments (Solid Lines Represent Finite Element Results, Dotted Lines Represent Analytic Solutions)

# B Remaining Results from Friction Variation Tests

## B.1 $\mu = 1.00$

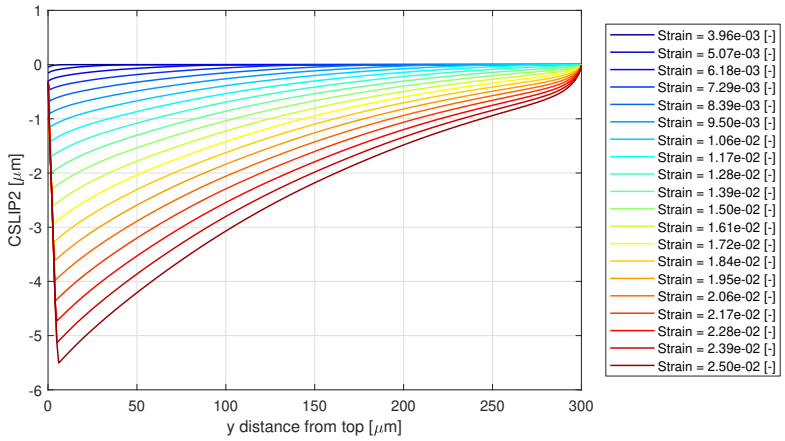


(a) Initial Loading Step

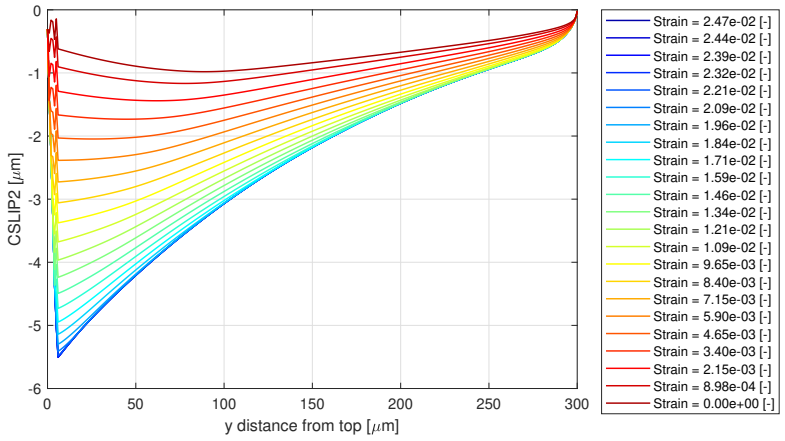


(b) Unloading Step

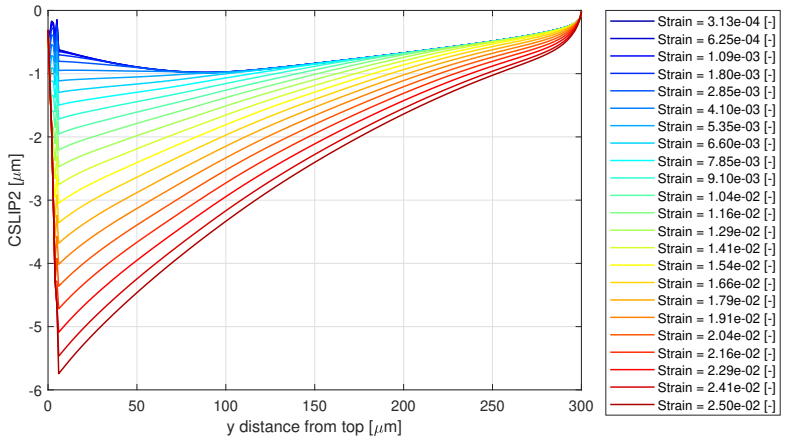


(c) Reloading Step

Figure 82: Interfacial Slipping Along Debond Interface, $\mu = 1.00$

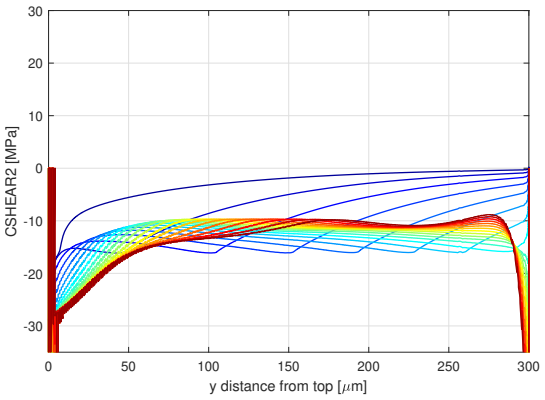


(a) Initial Loading Step

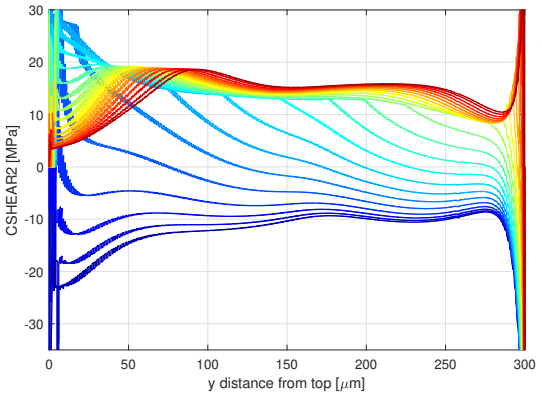


(b) Unloading Step

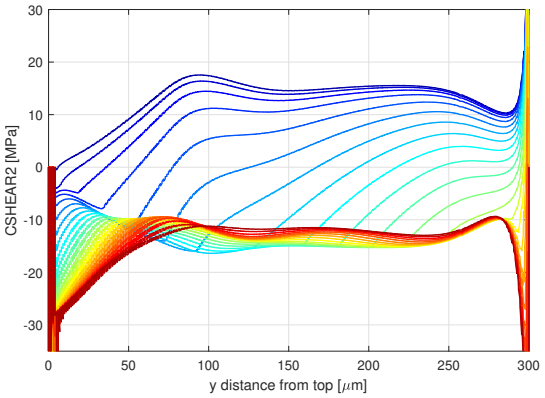


(c) Reloading Step

Figure 83: Shear Stress Along Debond Interface, $\mu = 1.00$

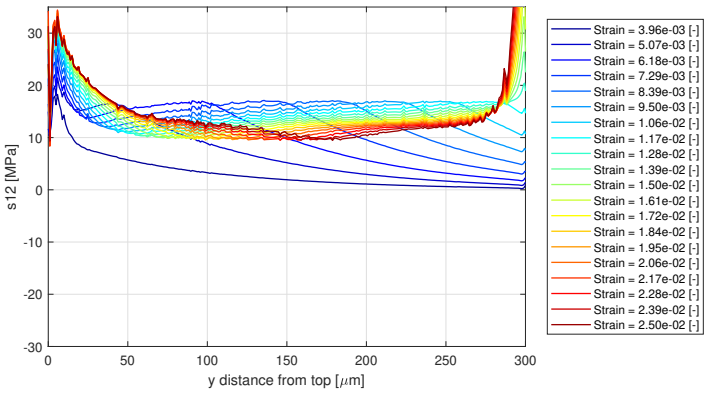


(a) Initial Loading Step

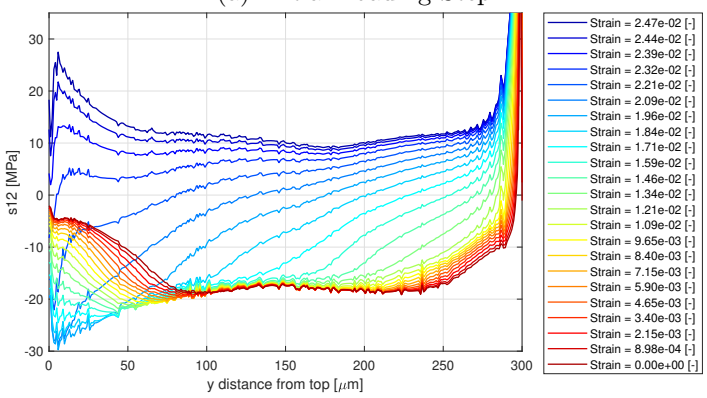


(b) Unloading Step

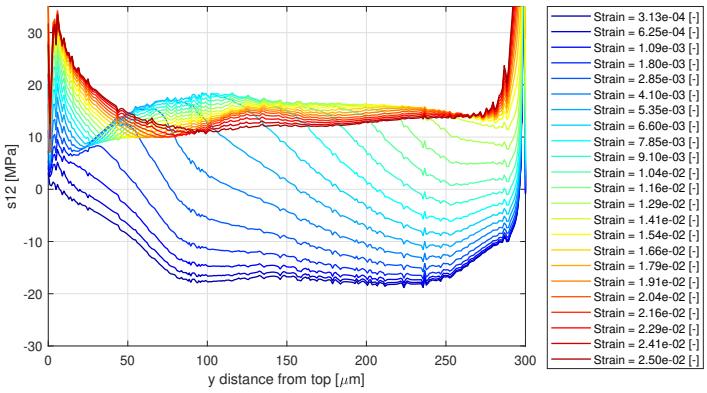


(c) Reloading Step

Figure 84: Broken Fibre Shear Stress Through Outer Path, $\mu = 1.00$, Cropped View

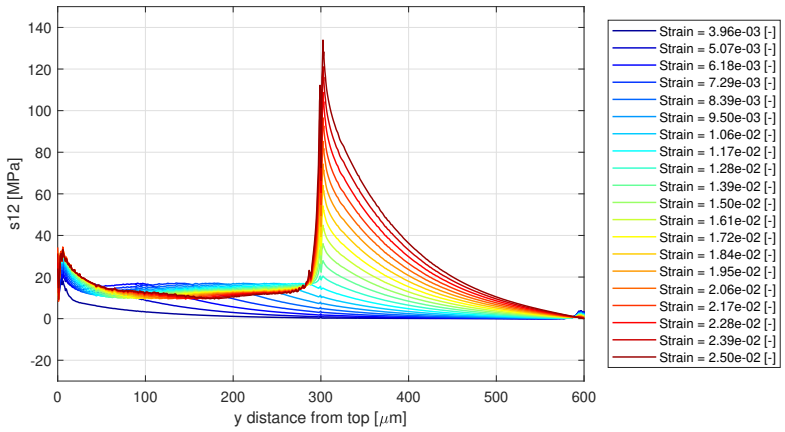


(a) Initial Loading Step

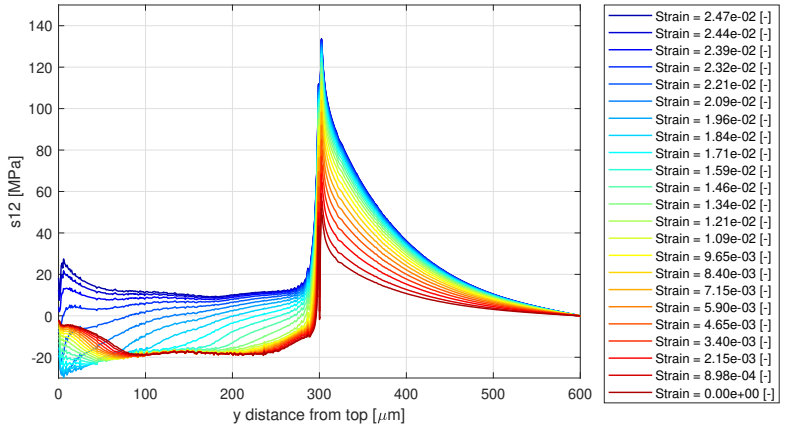


(b) Unloading Step

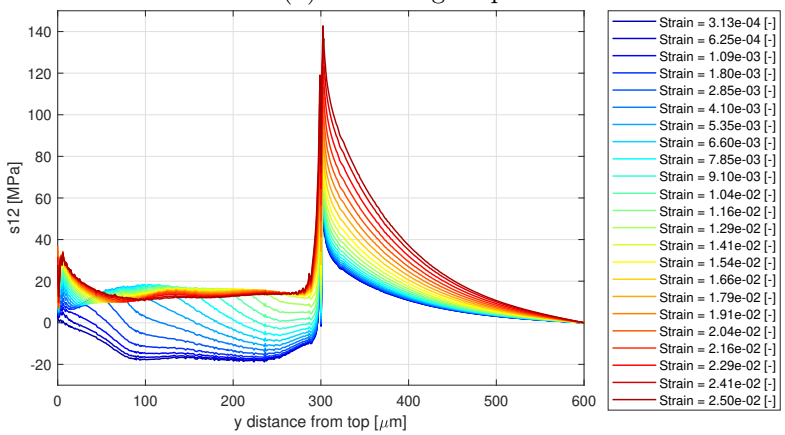


(c) Reloading Step

Figure 85: Broken Fibre Shear Stress Through Outer Path, $\mu = 1.00$, Full View

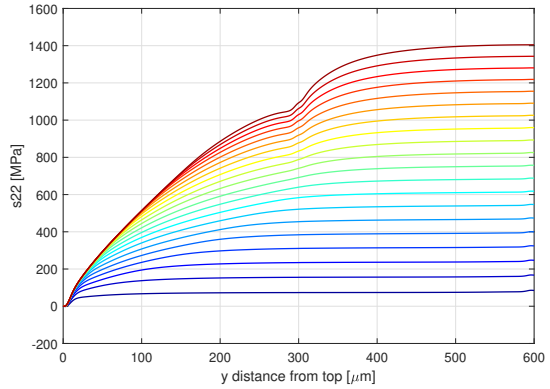


(a) Initial Loading Step

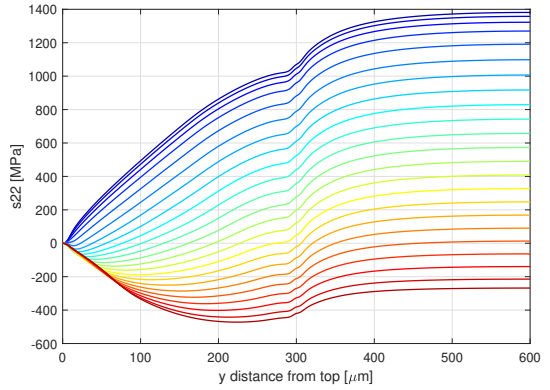


(b) Unloading Step

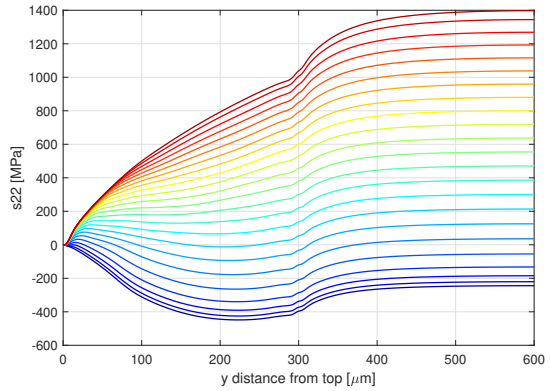


(c) Reloading Step

Figure 86: Broken Fibre S22 Through Centre Path, $\mu = 1.00$

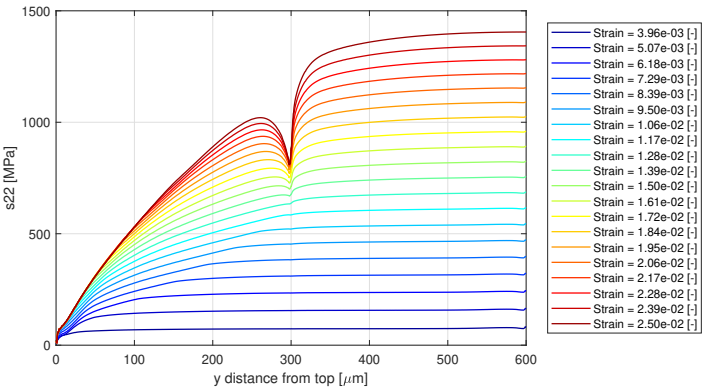


(a) Initial Loading Step

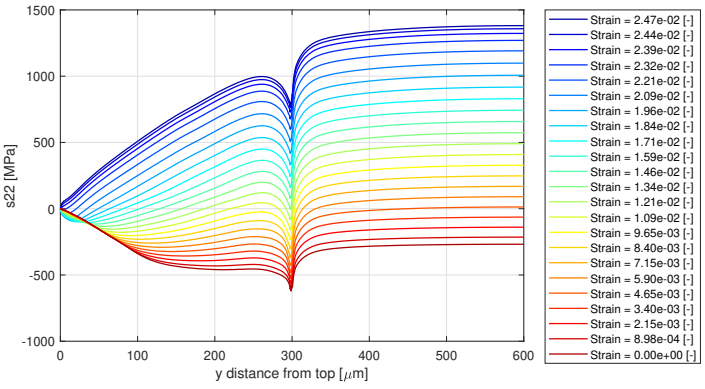


(b) Unloading Step

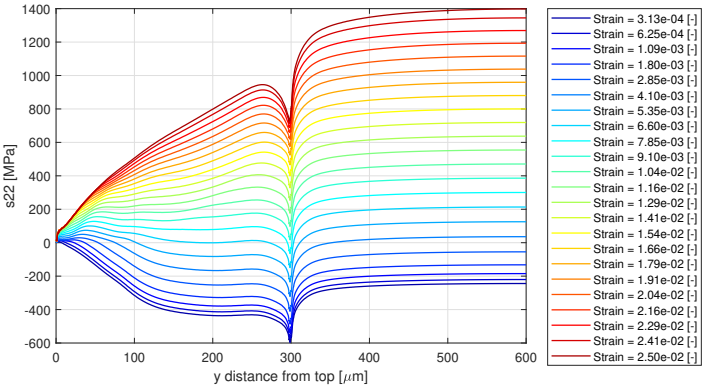


(c) Reloading Step

Figure 87: Broken Fibre S22 Through Outer Path, $\mu = 1.00$

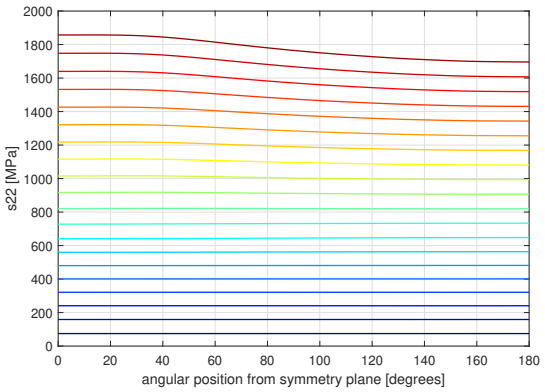


(a) Initial Loading Step

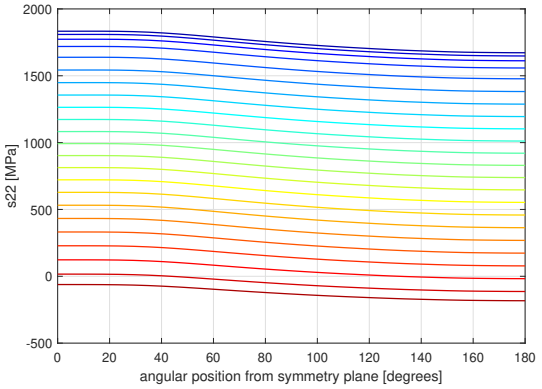


(b) Unloading Step

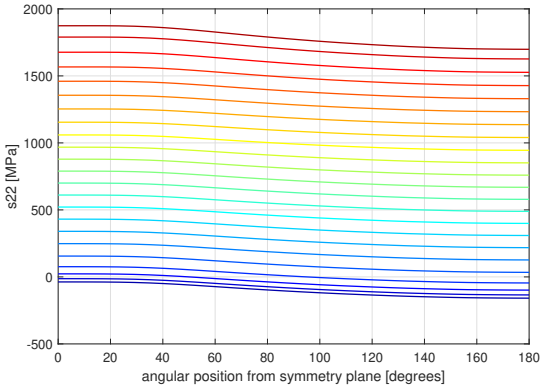


(c) Reloading Step

Figure 88: S22 Along Perimeter of Neighbouring Fibre Cross Section, $\mu = 1.00$

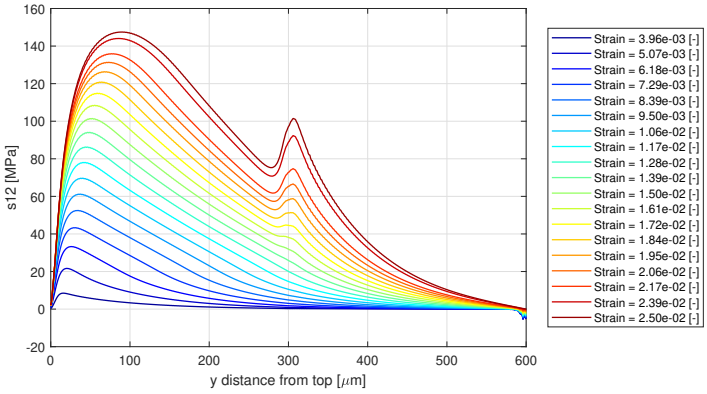


(a) Initial Loading Step

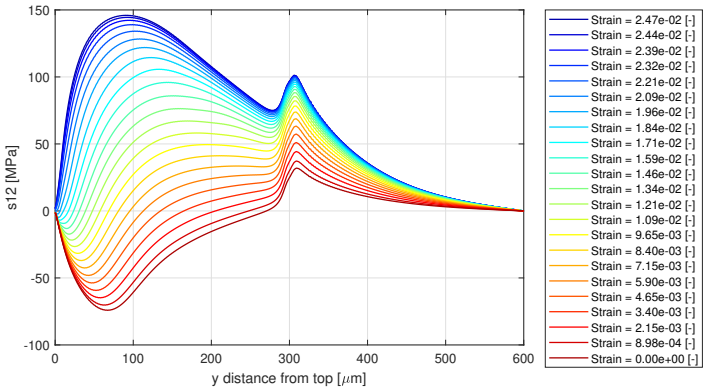


(b) Unloading Step

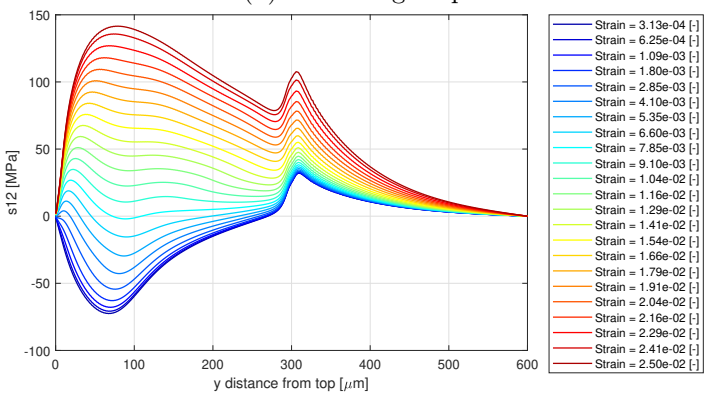


(c) Reloading Step

Figure 89: S12 at Surface of Neighbouring Fibre, $\mu = 1.00$

## B.2 $\mu = 0.75$

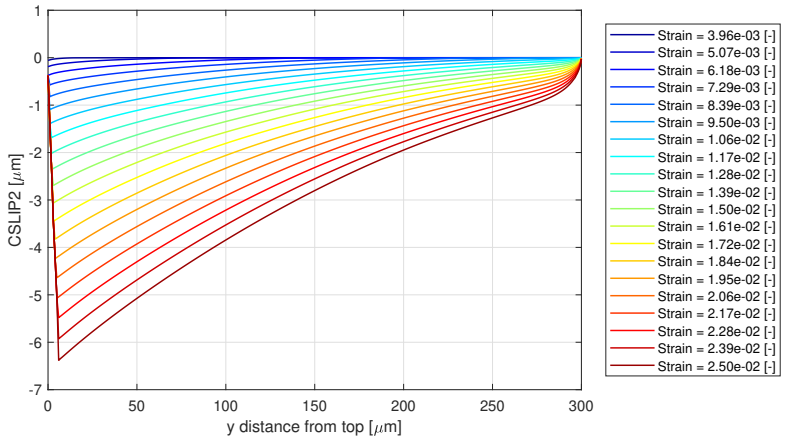


(a) Initial Loading Step

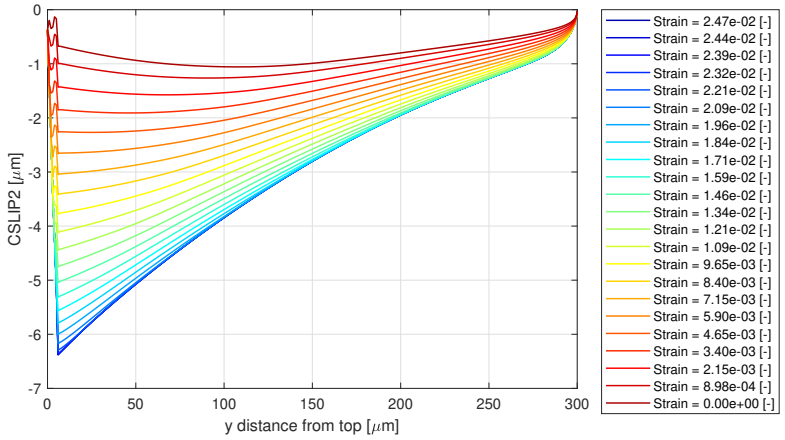


(b) Unloading Step

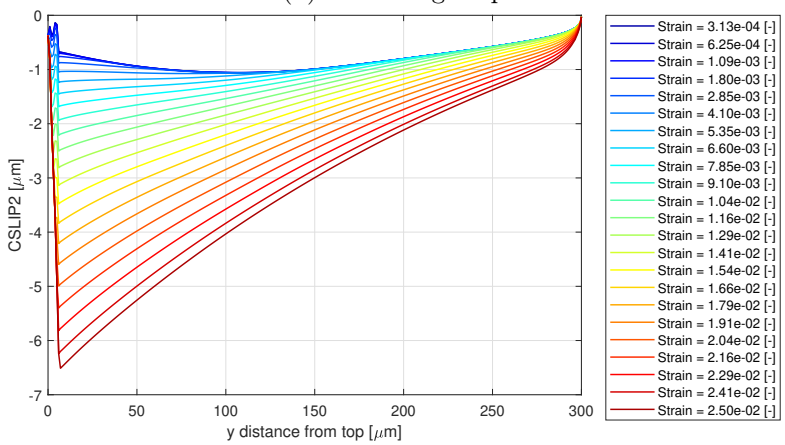


(c) Reloading Step

Figure 90: Interfacial Slipping Along Debond Interface, $\mu = 0.75$

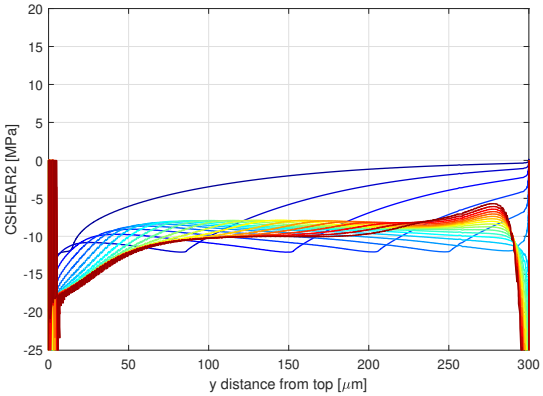


(a) Initial Loading Step

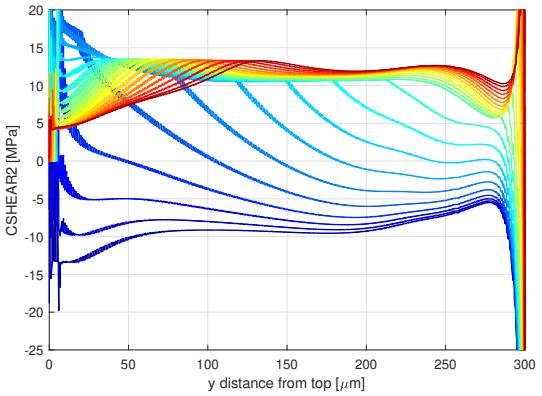


(b) Unloading Step

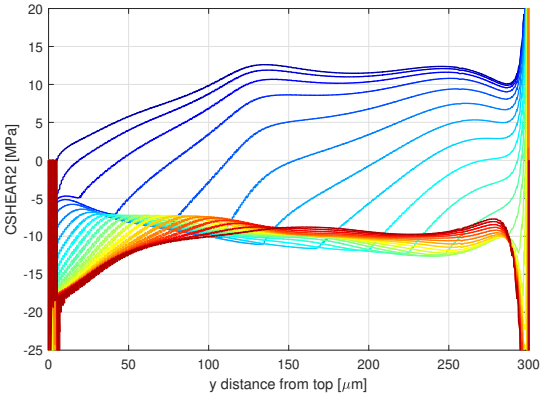


(c) Reloading Step

Figure 91: Shear Stress Along Debond Interface, $\mu = 0.75$

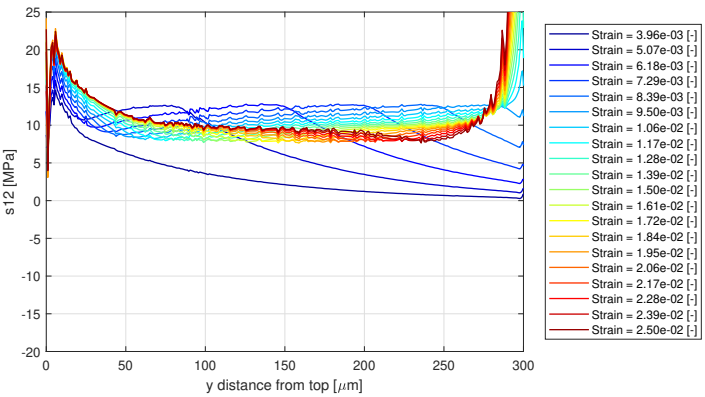


(a) Initial Loading Step

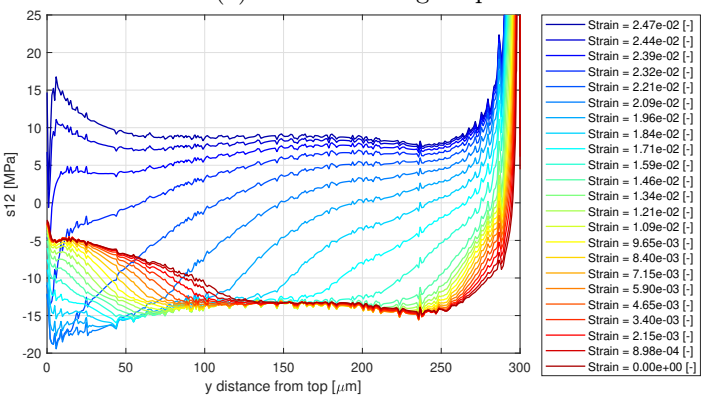


(b) Unloading Step

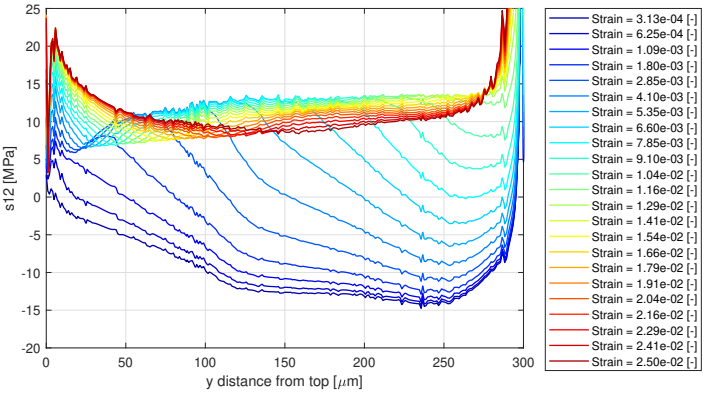


(c) Reloading Step

Figure 92: Broken Fibre Shear Stress Through Outer Path, $\mu = 0.75$, Cropped View

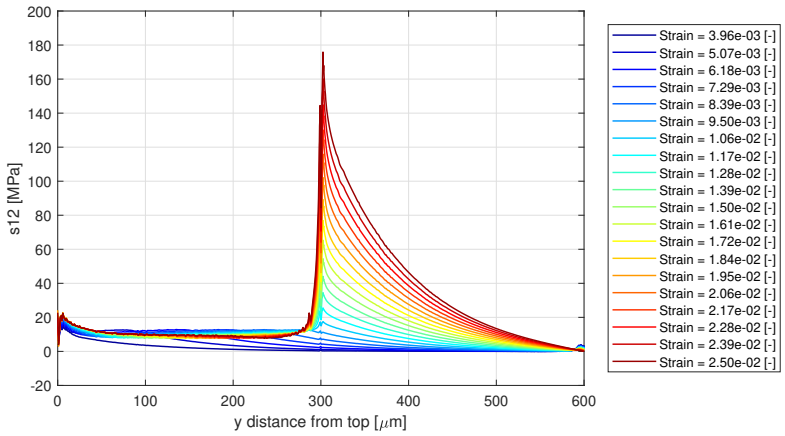


(a) Initial Loading Step

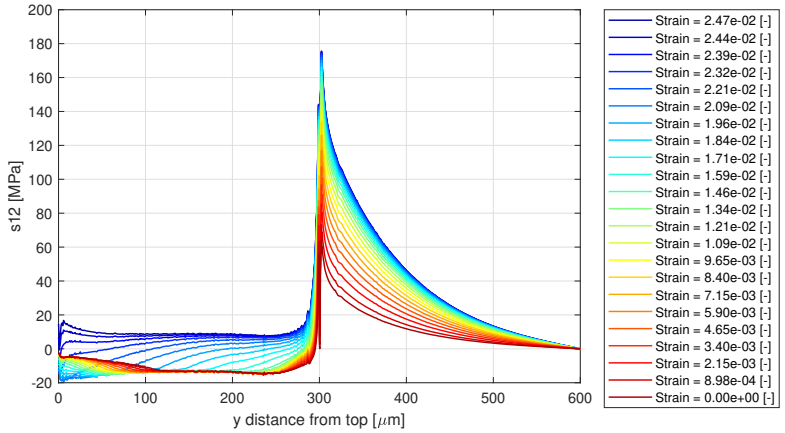


(b) Unloading Step

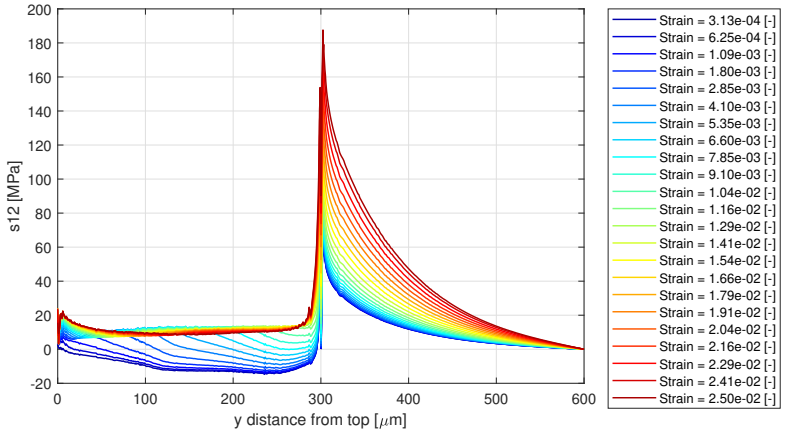


(c) Reloading Step

Figure 93: Broken Fibre Shear Stress Through Outer Path, $\mu = 0.75$, Full View

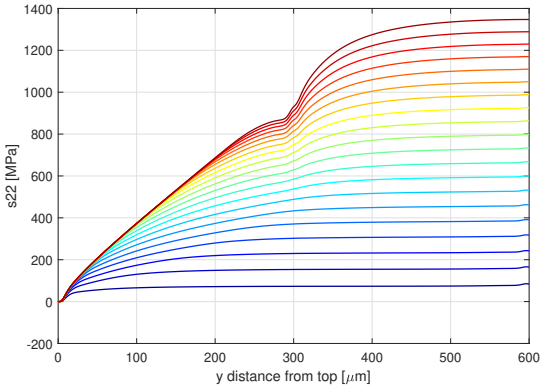


(a) Initial Loading Step

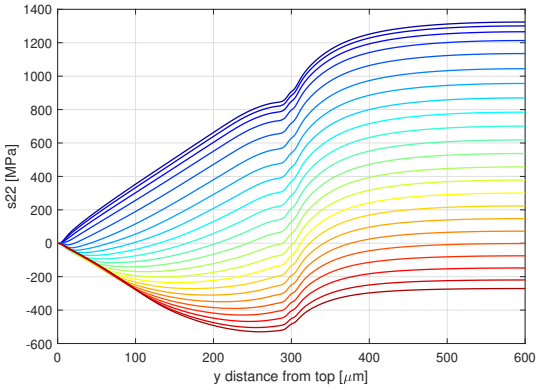


(b) Unloading Step

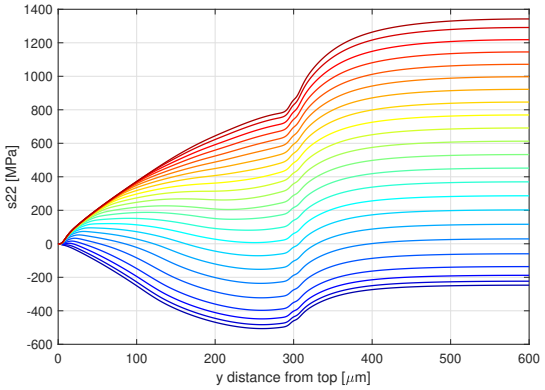


(c) Reloading Step

Figure 94: Broken Fibre S22 Through Centre Path, $\mu = 0.75$

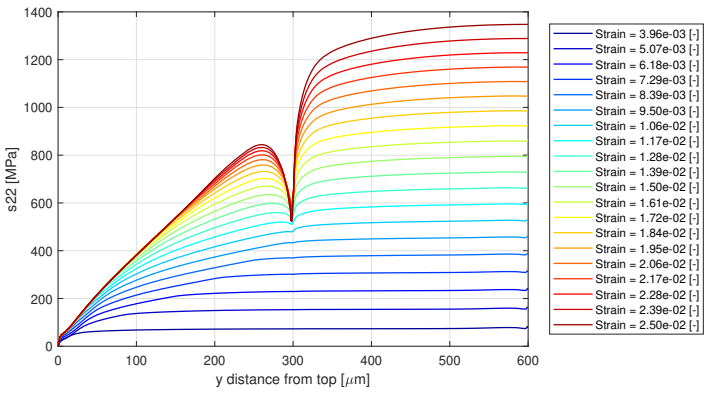


(a) Initial Loading Step

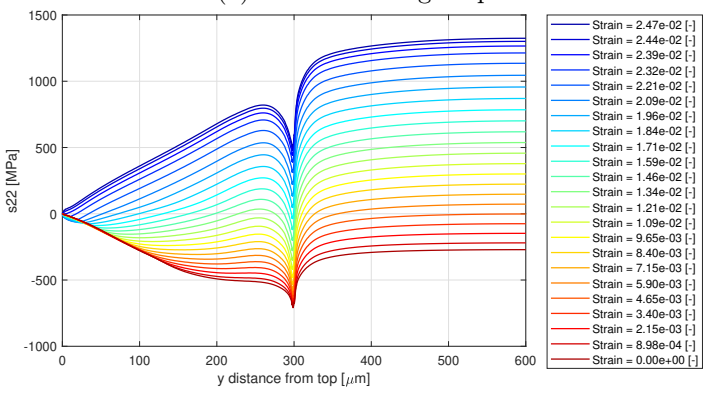


(b) Unloading Step

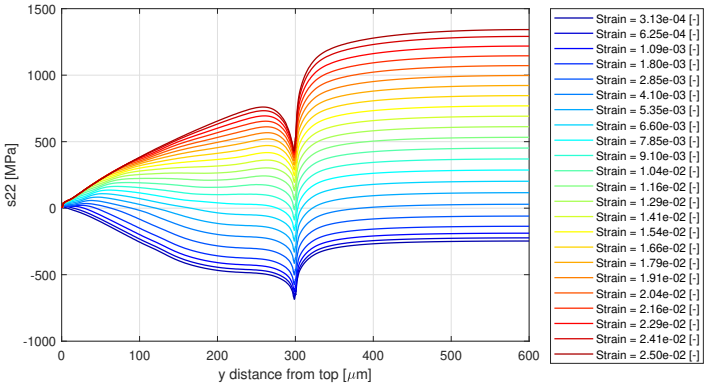


(c) Reloading Step

Figure 95: Broken Fibre S22 Through Outer Path, $\mu = 0.75$

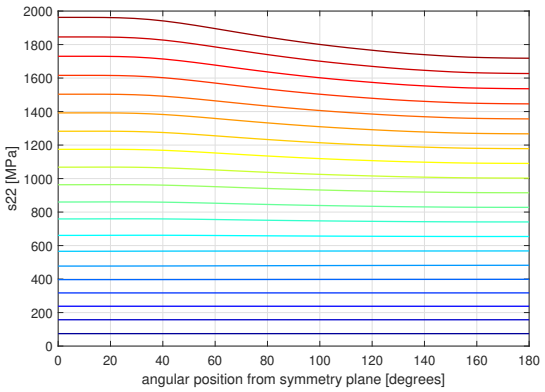


(a) Initial Loading Step

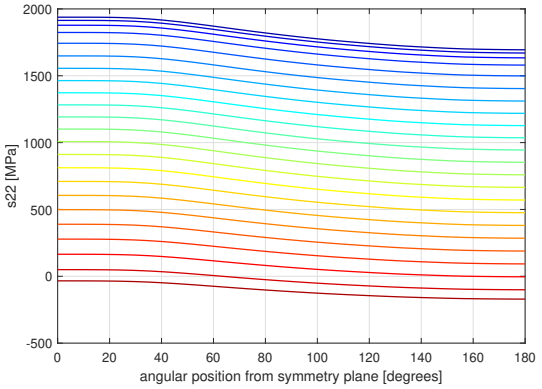


(b) Unloading Step

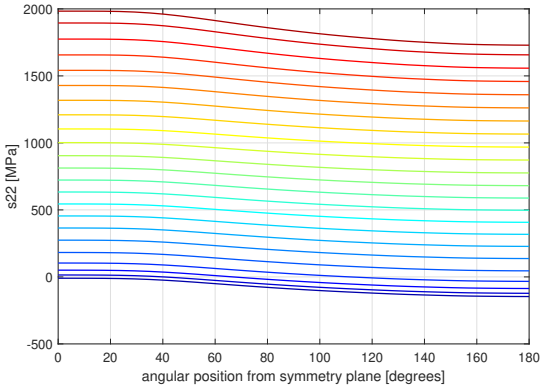


(c) Reloading Step

Figure 96: S22 Along Perimeter of Neighbouring Fibre Cross Section, $\mu = 0.75$

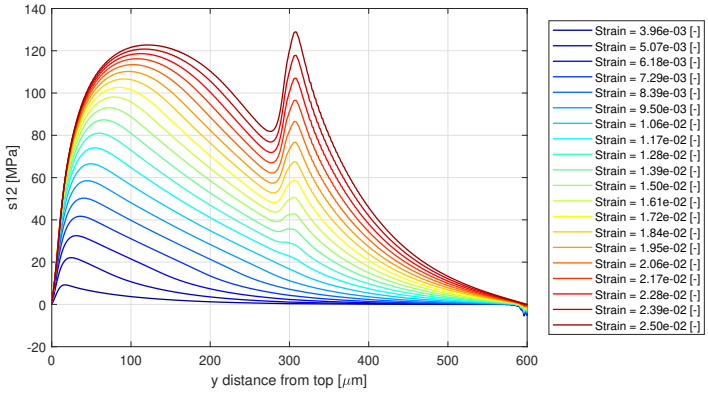


(a) Initial Loading Step

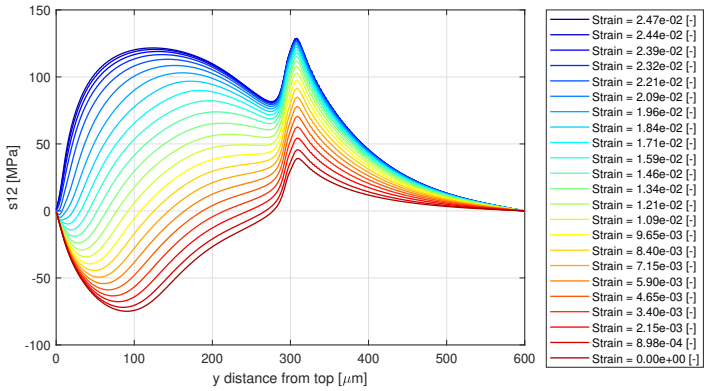


(b) Unloading Step

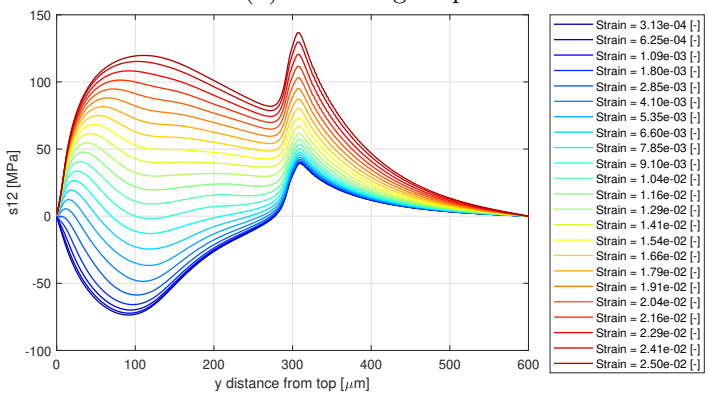


(c) Reloading Step

Figure 97: S12 at Surface of Neighbouring Fibre, $\mu = 0.75$

## B.3 $\mu = 0.25$

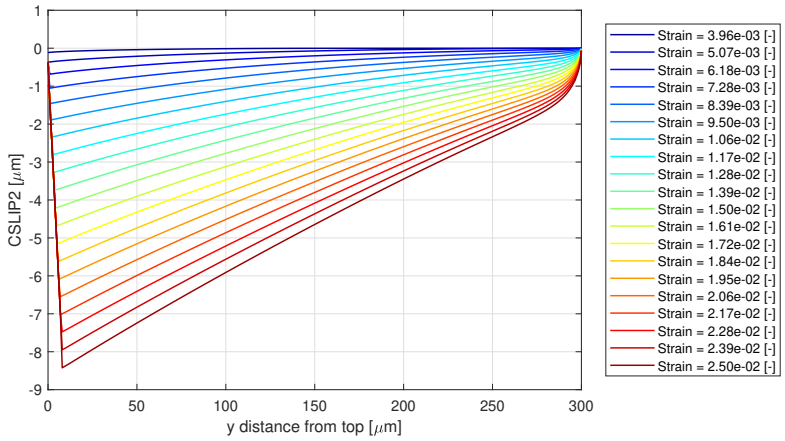


(a) Initial Loading Step

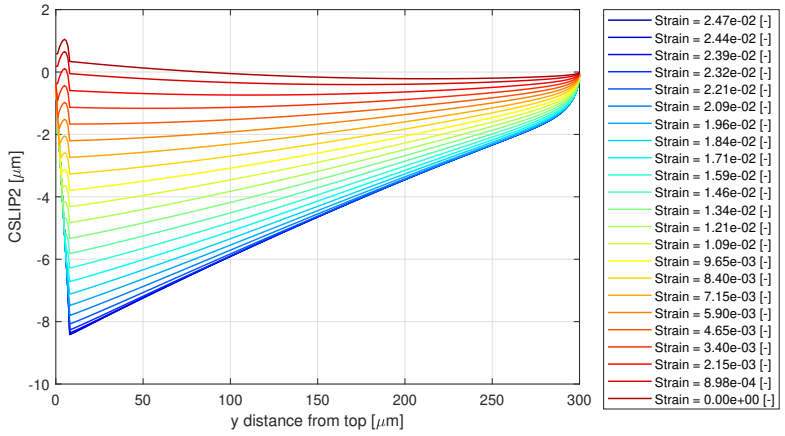


(b) Unloading Step

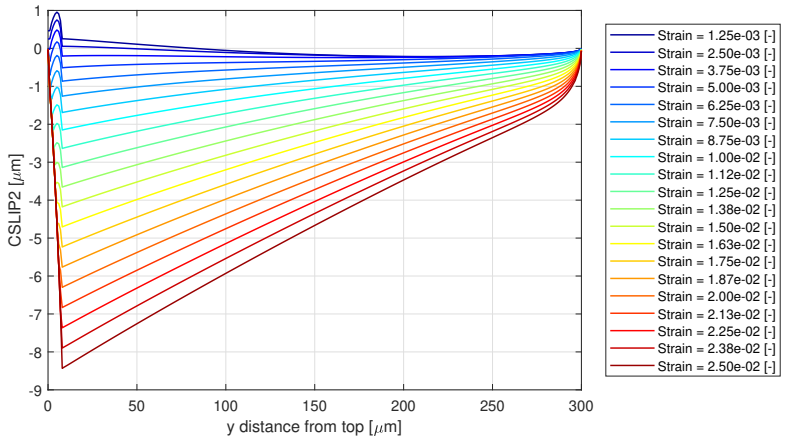


(c) Reloading Step

Figure 98: Interfacial Slipping Along Debond Interface, $\mu = 0.25$

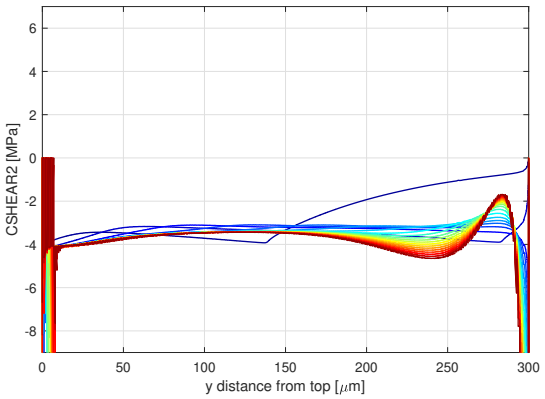


(a) Initial Loading Step

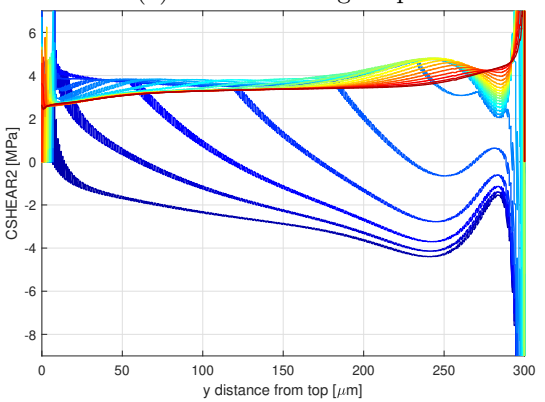


(b) Unloading Step

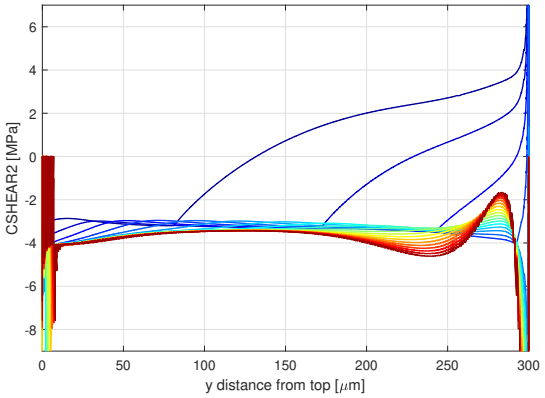


(c) Reloading Step

Figure 99: Shear Stress Along Debond Interface, $\mu = 0.25$

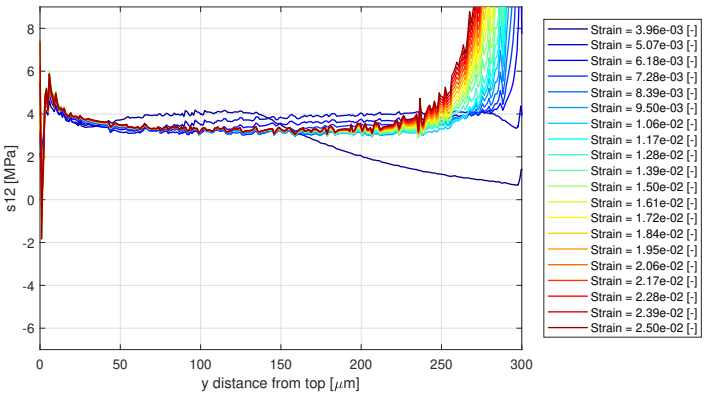


(a) Initial Loading Step

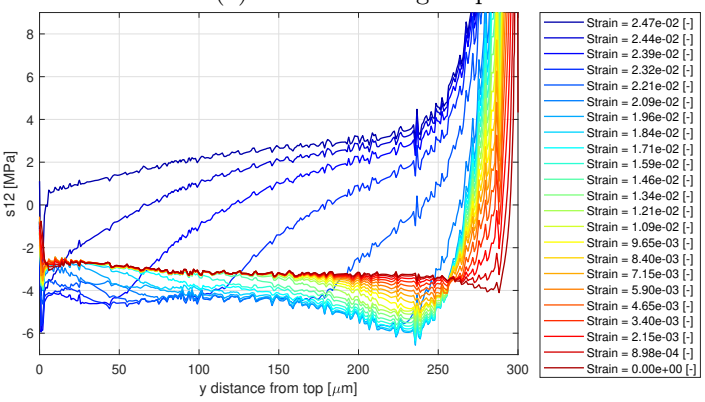


(b) Unloading Step

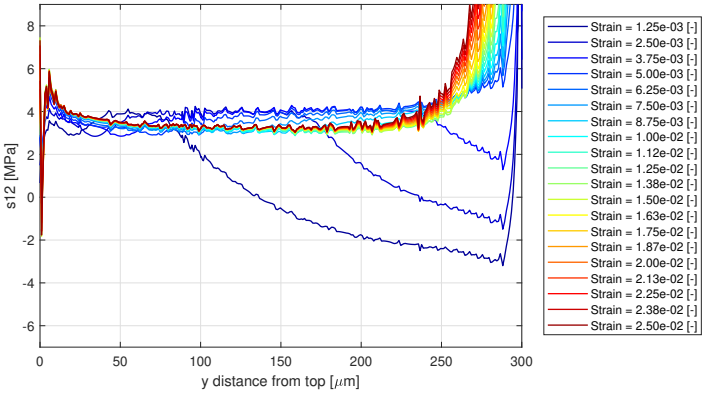


(c) Reloading Step

Figure 100: Broken Fibre Shear Stress Through Outer Path, $\mu = 0.25$, Cropped View

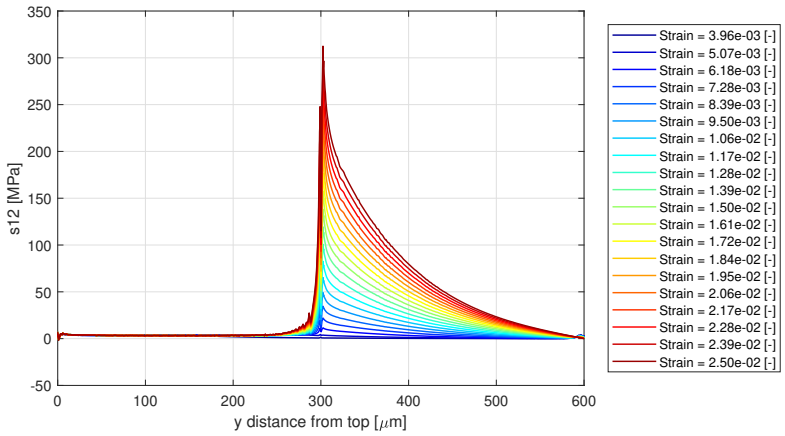


(a) Initial Loading Step

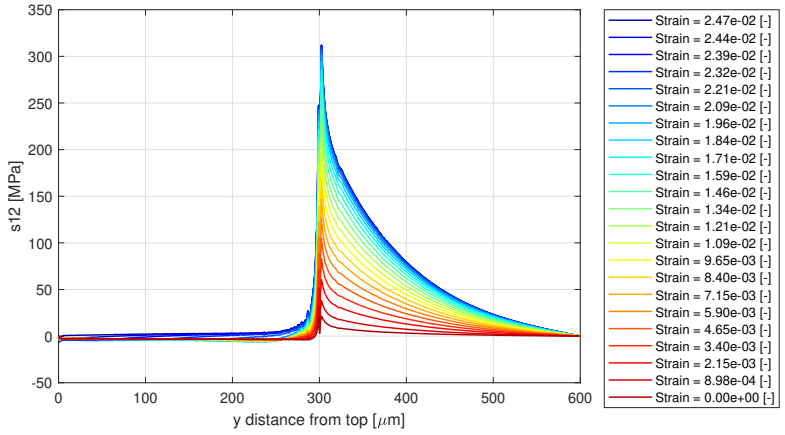


(b) Unloading Step

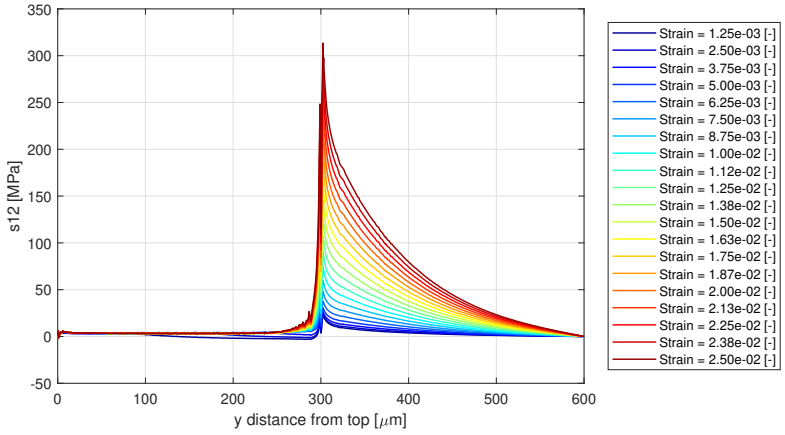


(c) Reloading Step

Figure 101: Broken Fibre Shear Stress Through Outer Path, $\mu = 0.25$, Full View

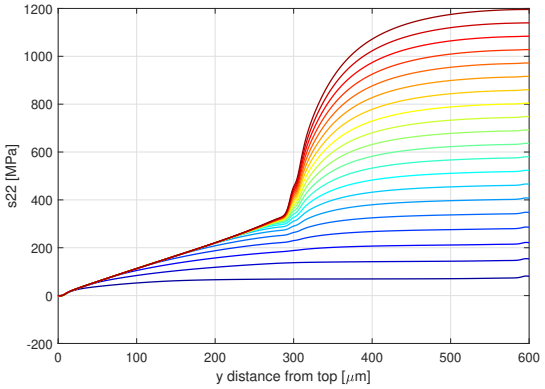


(a) Initial Loading Step

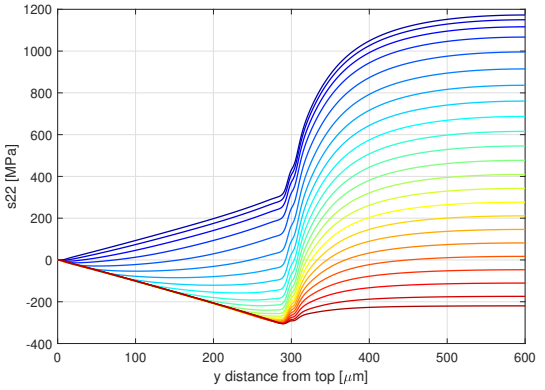


(b) Unloading Step

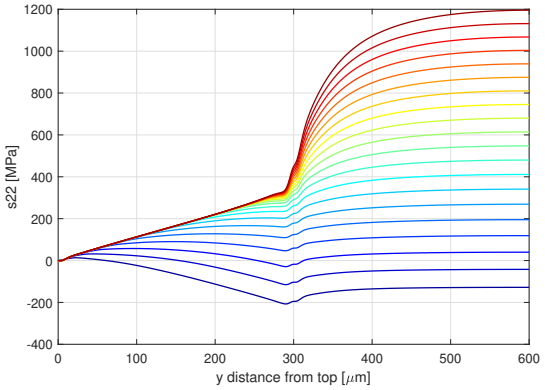


(c) Reloading Step

Figure 102: Broken Fibre S22 Through Centre Path, $\mu = 0.25$

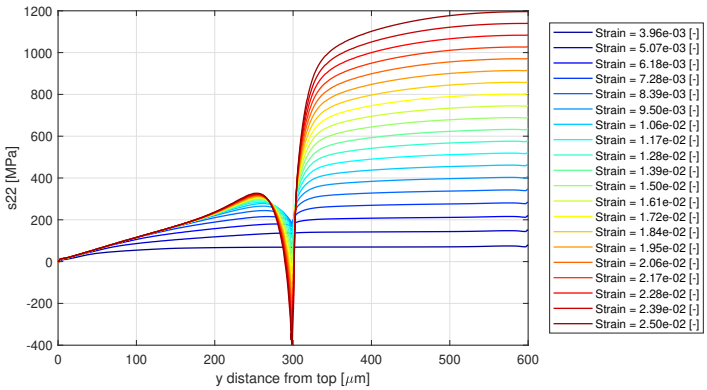


(a) Initial Loading Step

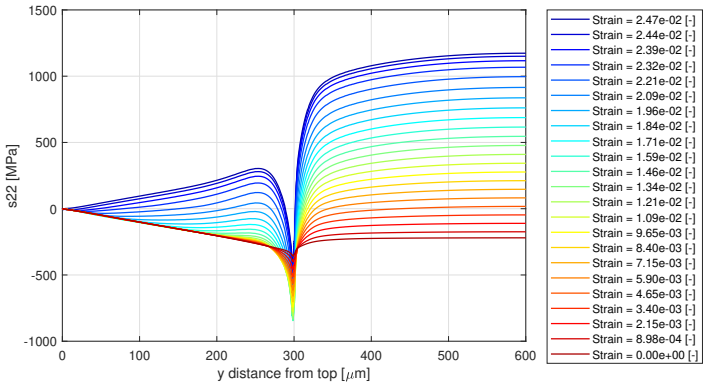


(b) Unloading Step

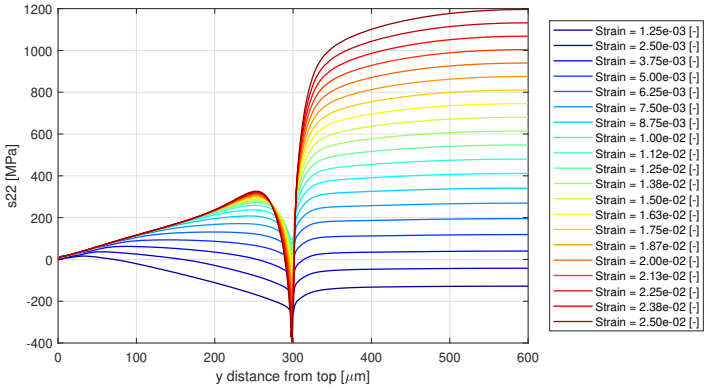


(c) Reloading Step

Figure 103: Broken Fibre S22 Through Outer Path, $\mu = 0.25$

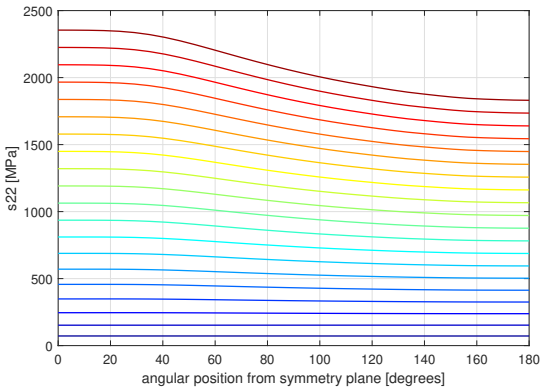


(a) Initial Loading Step

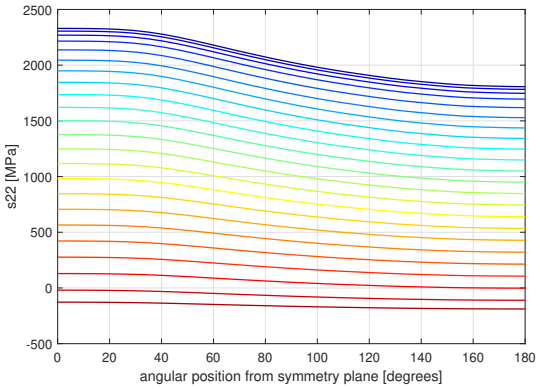


(b) Unloading Step

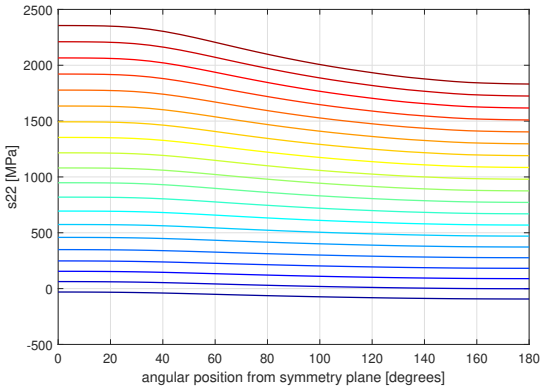


(c) Reloading Step

Figure 104: S22 Along Perimeter of Neighbouring Fibre Cross Section, $\mu = 0.25$

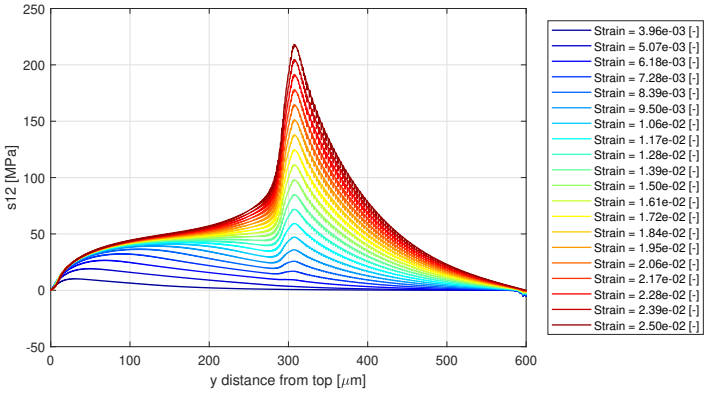


(a) Initial Loading Step

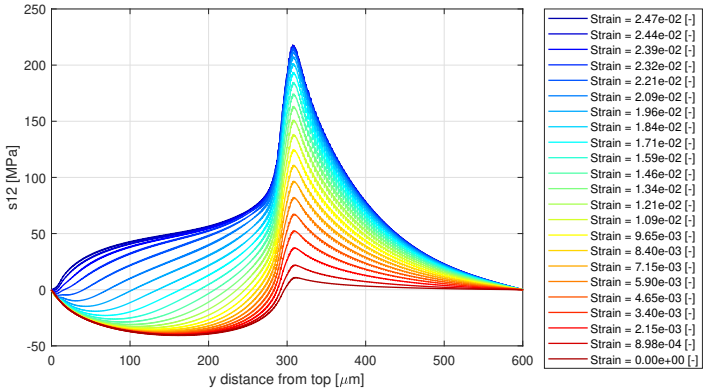


(b) Unloading Step

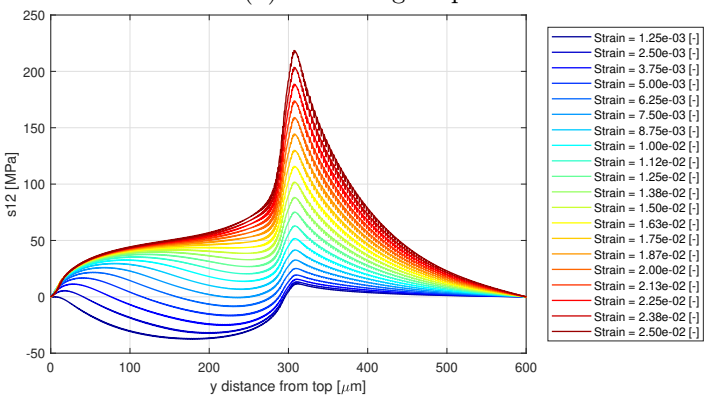


(c) Reloading Step

Figure 105: S12 at Surface of Neighbouring Fibre, $\mu = 0.25$

## B.4 $\mu = 0.10$

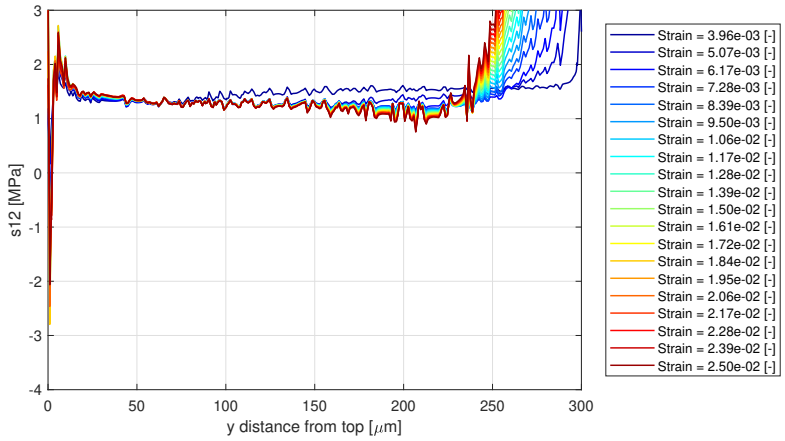


(a) Initial Loading Step

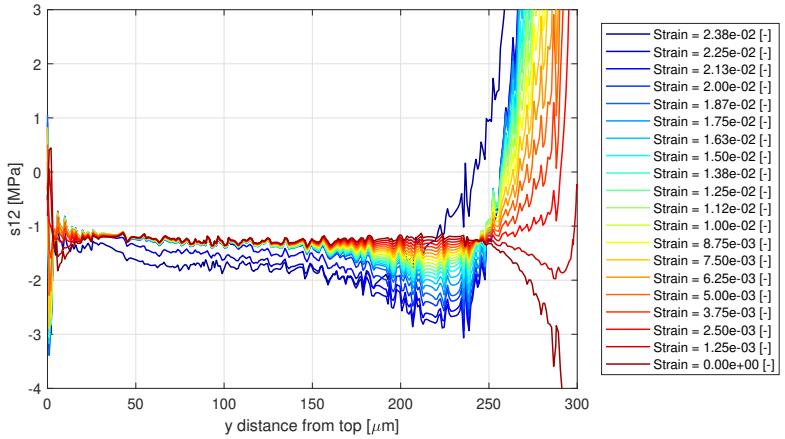


(b) Unloading Step

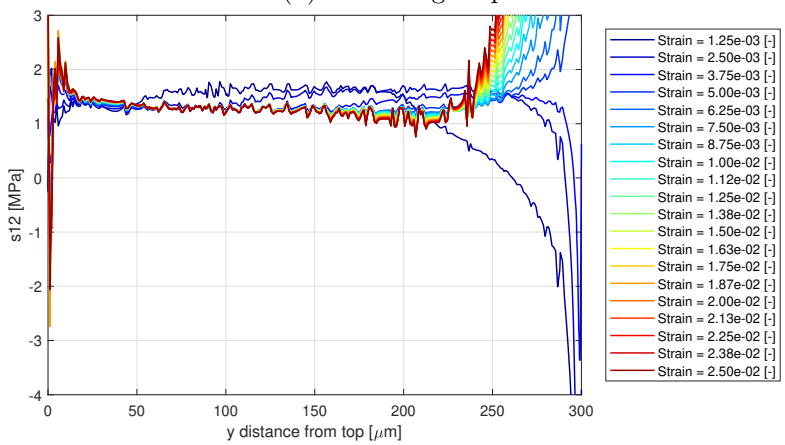


(c) Reloading Step

Figure 106: Broken Fibre Shear Stress Through Outer Path, $\mu = 0.10$, Cropped View

## B.5 $\mu = 0.00$ (Frictionless Case)

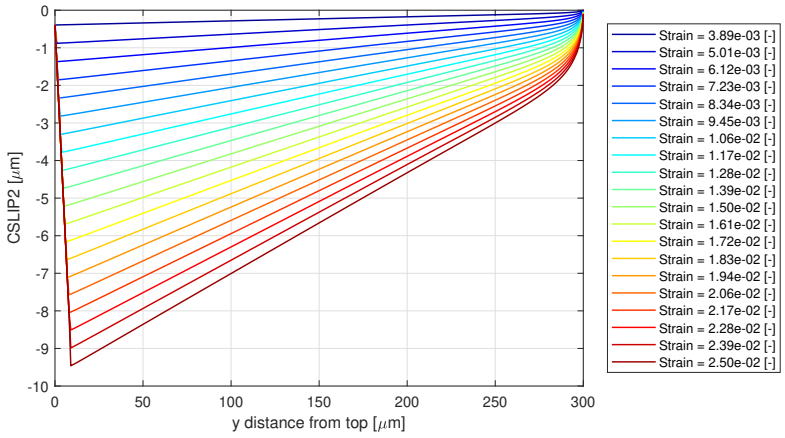


(a) Initial Loading Step

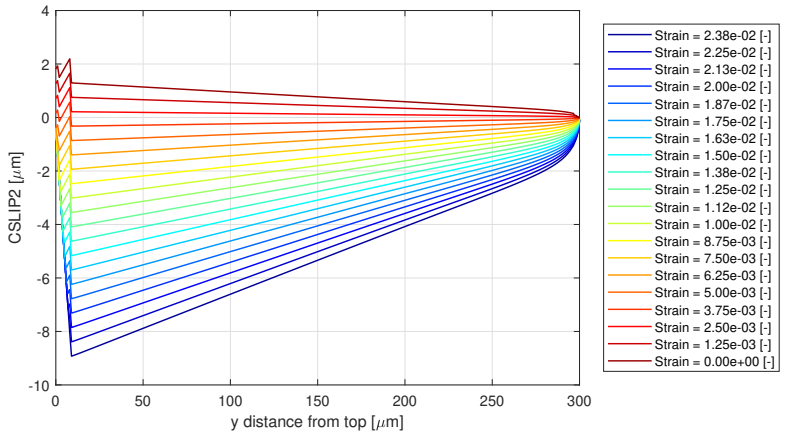


(b) Unloading Step

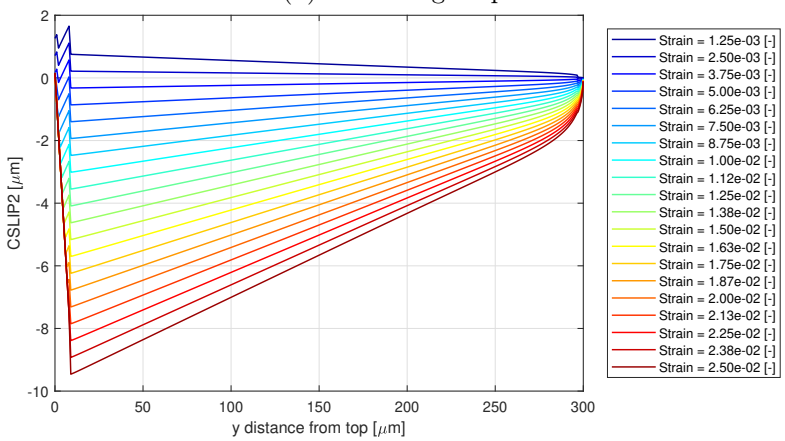


(c) Reloading Step

Figure 107: Interfacial Slipping Along Debond Interface, $\mu = 0.00$

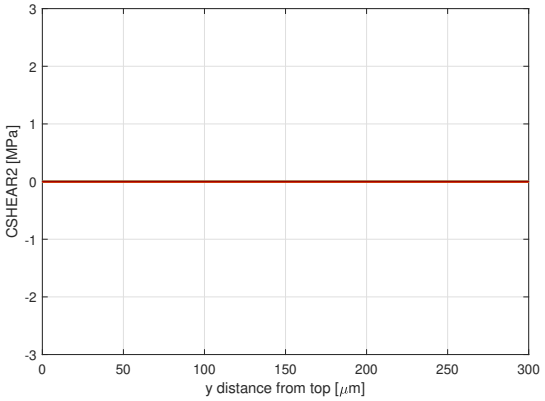


(a) Initial Loading Step

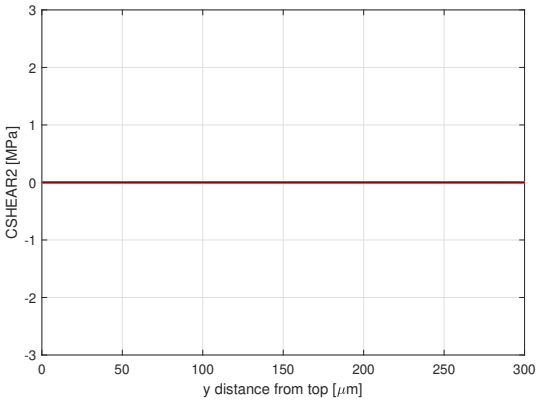


(b) Unloading Step

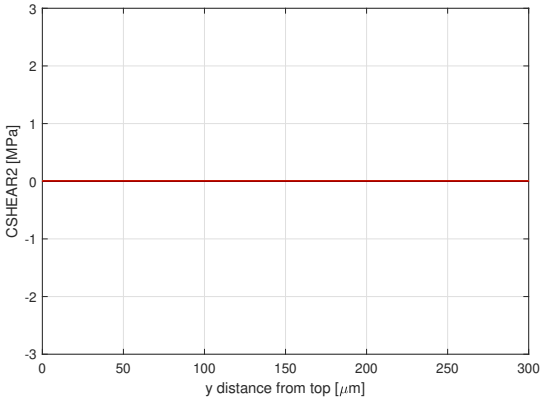


(c) Reloading Step

Figure 108: Shear Stress Along Debond Interface, $\mu = 0.00$

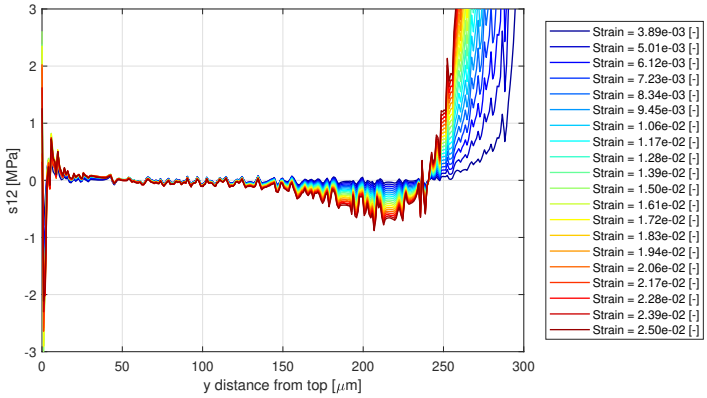


(a) Initial Loading Step

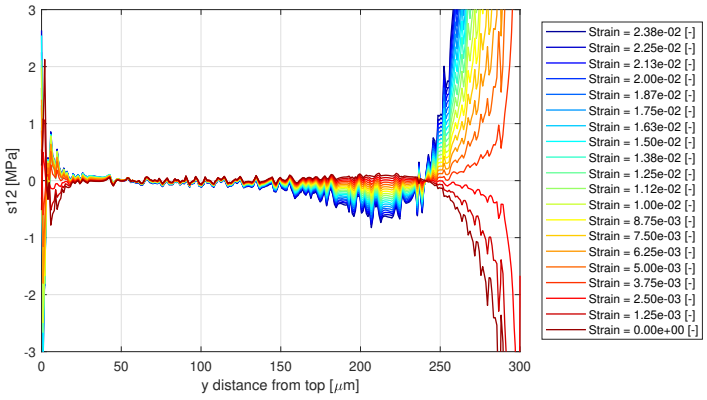


(b) Unloading Step

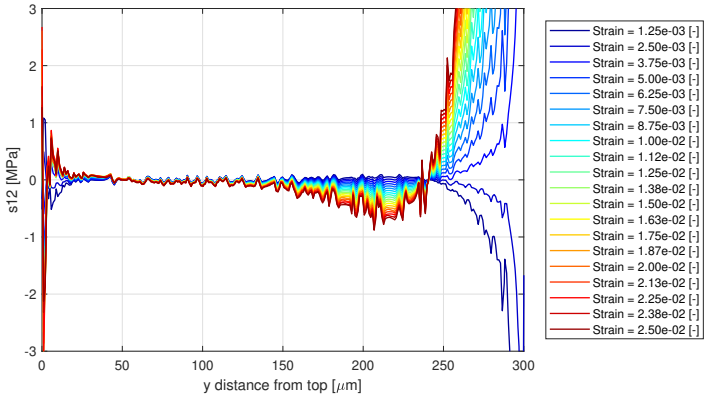


(c) Reloading Step

Figure 109: Broken Fibre Shear Stress Through Outer Path, $\mu = 0.00$, Cropped View

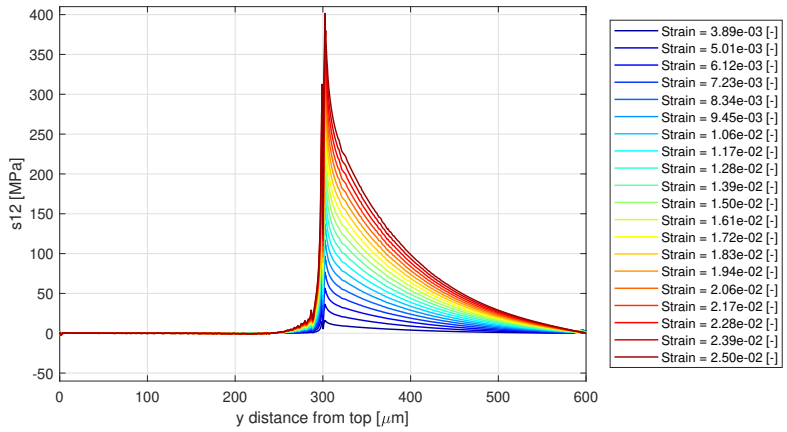


(a) Initial Loading Step

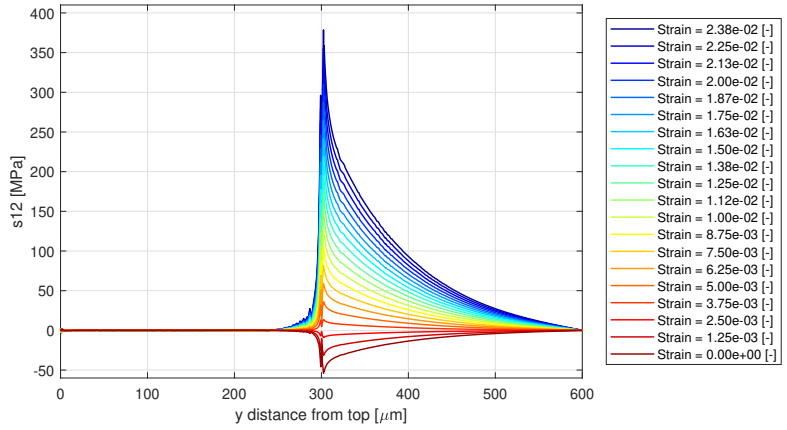


(b) Unloading Step

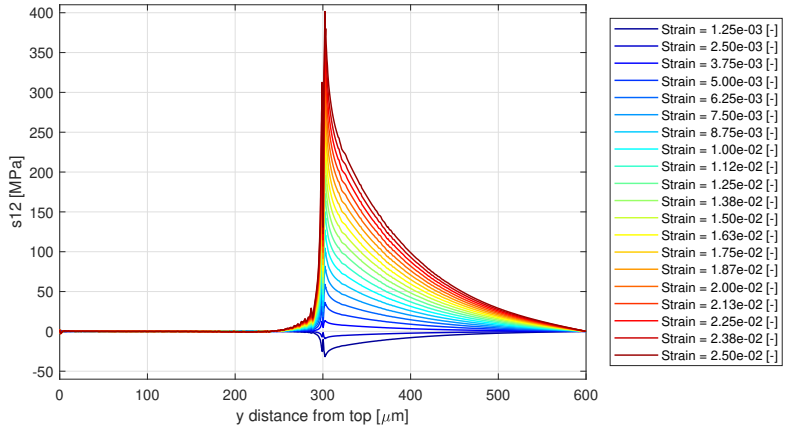


(c) Reloading Step

Figure 110: Broken Fibre Shear Stress Through Outer Path, $\mu = 0.00$, Full View

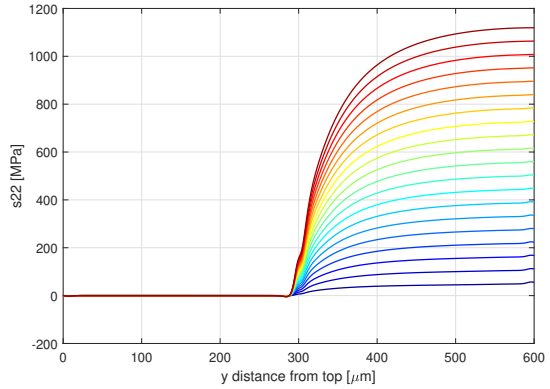


(a) Initial Loading Step

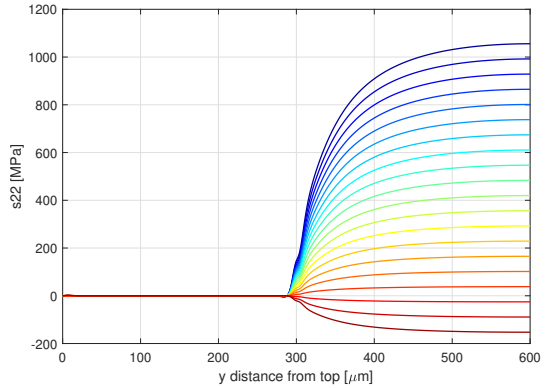


(b) Unloading Step

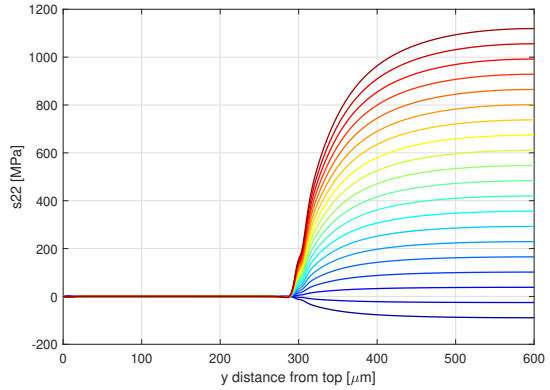


(c) Reloading Step

Figure 111: Broken Fibre S22 Through Centre Path, $\mu = 0.00$

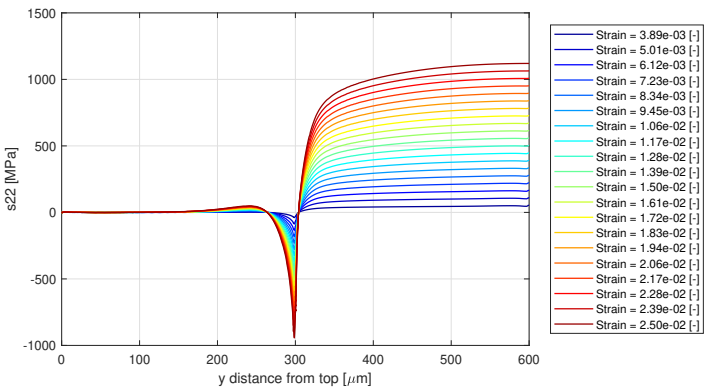


(a) Initial Loading Step

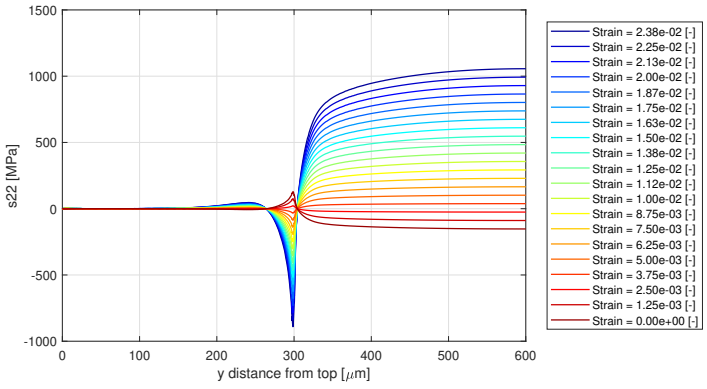


(b) Unloading Step

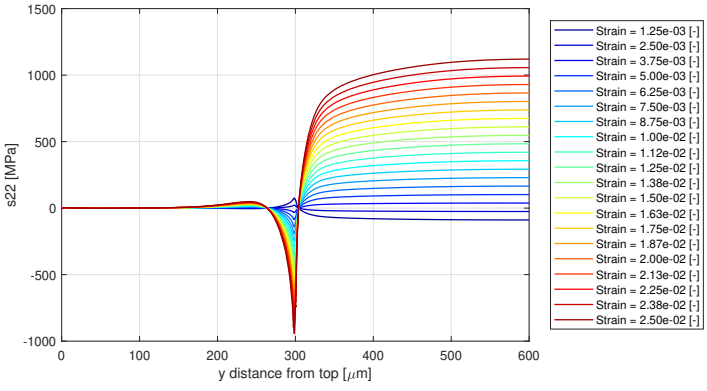


(c) Reloading Step

Figure 112: Broken Fibre S22 Through Outer Path, $\mu = 0.00$

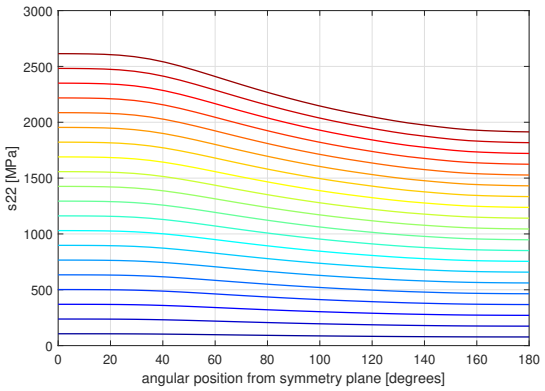


(a) Initial Loading Step

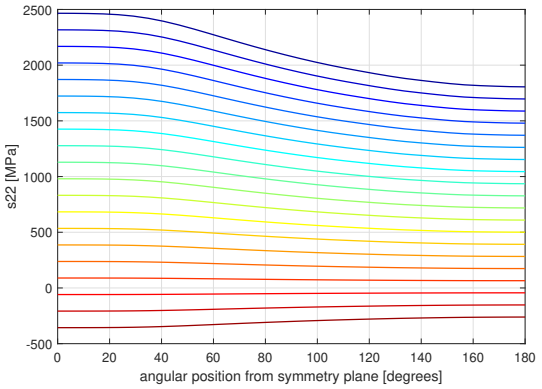


(b) Unloading Step

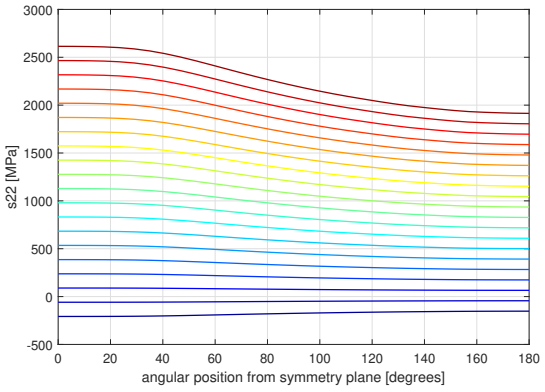


(c) Reloading Step

Figure 113: S22 Along Perimeter of Neighbouring Fibre Cross Section, $\mu = 0.00$

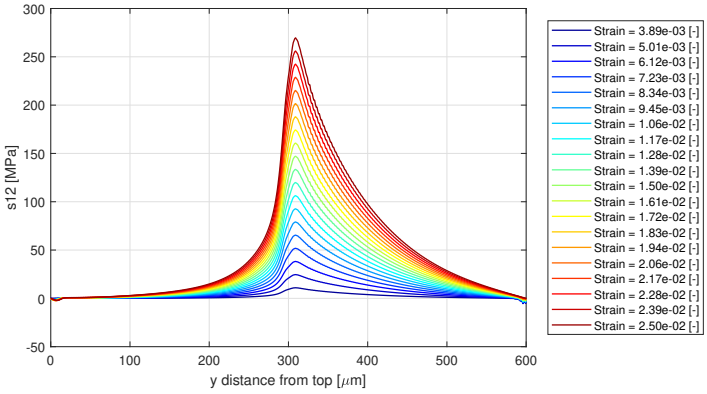


(a) Initial Loading Step

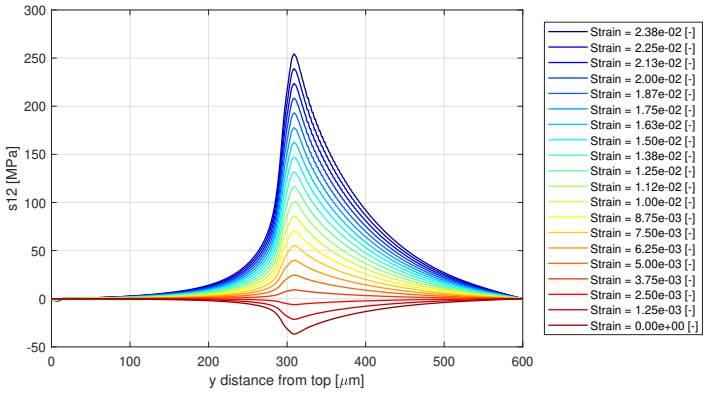


(b) Unloading Step

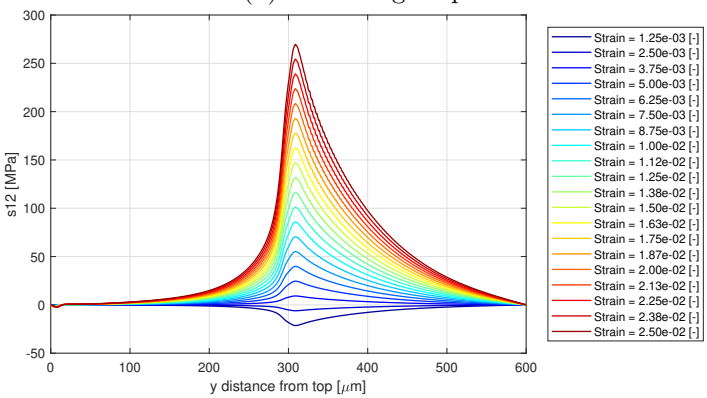


(c) Reloading Step

Figure 114: S12 at Surface of Neighbouring Fibre, $\mu = 0.00$

# C Remaining Results from Fibre Volume Fraction Variation Tests

## C.1 25% Packing

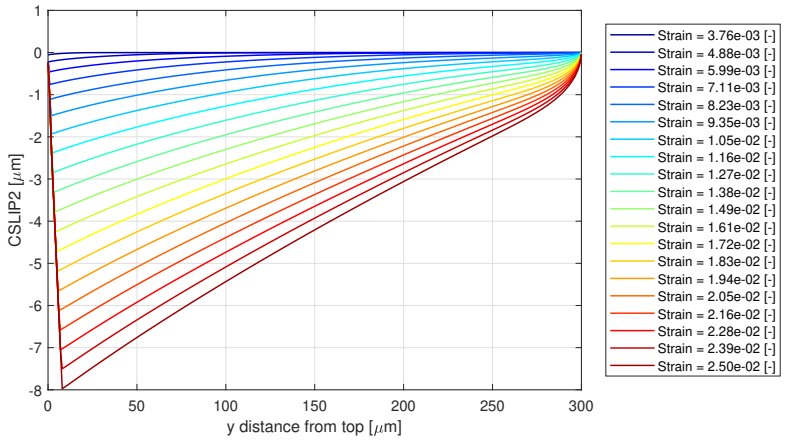


(a) Initial Loading Step

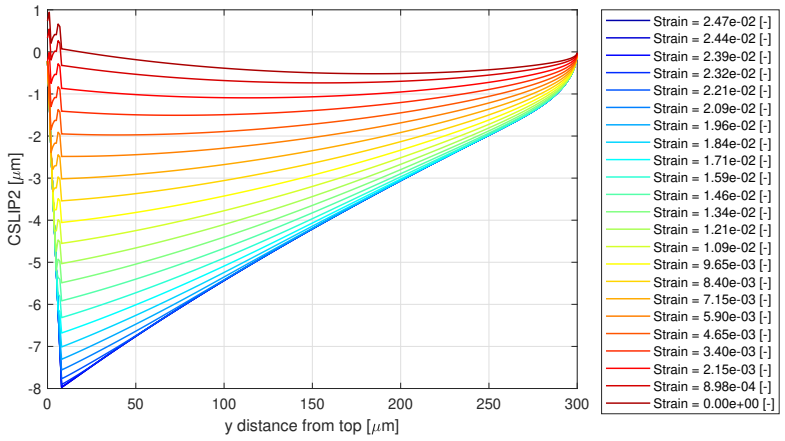


(b) Unloading Step

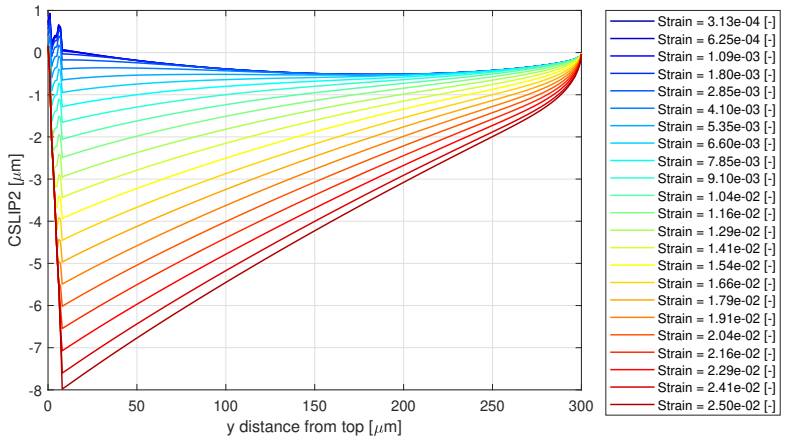


(c) Reloading Step

Figure 115: Interfacial Slipping Along Debond Interface, 25% Packing

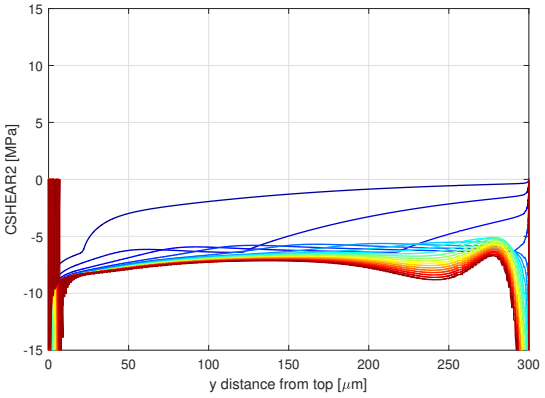


(a) Initial Loading Step

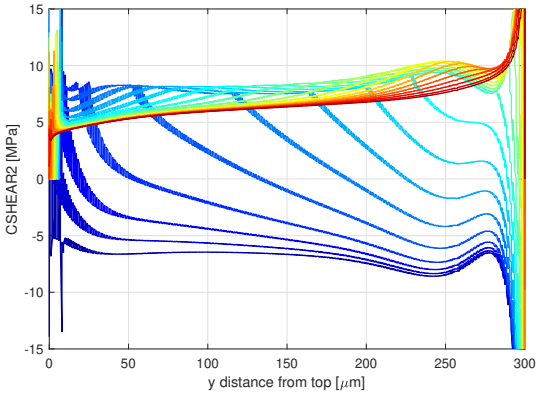


(b) Unloading Step

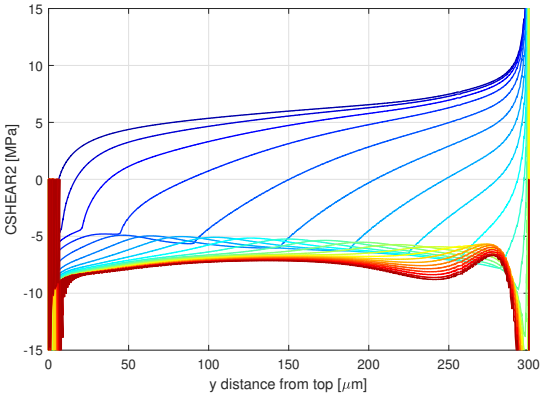


(c) Reloading Step

Figure 116: Shear Stress Along Debond Interface, 25% Packing

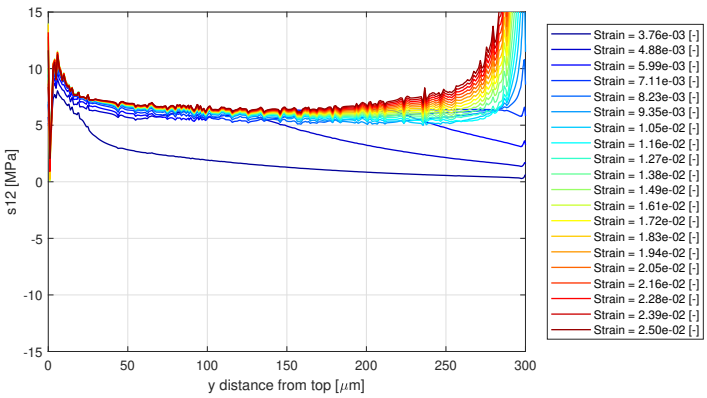


(a) Initial Loading Step

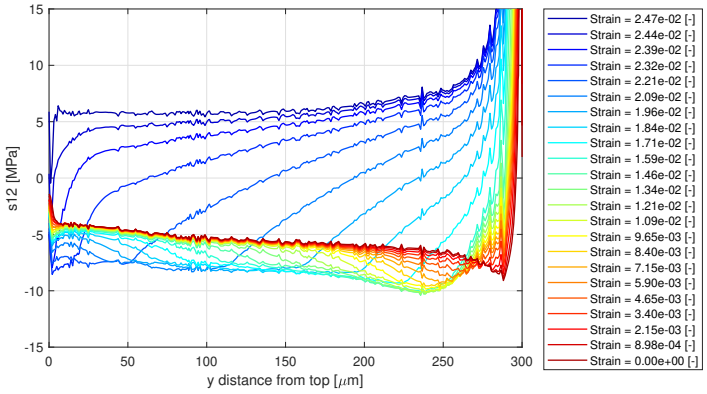


(b) Unloading Step

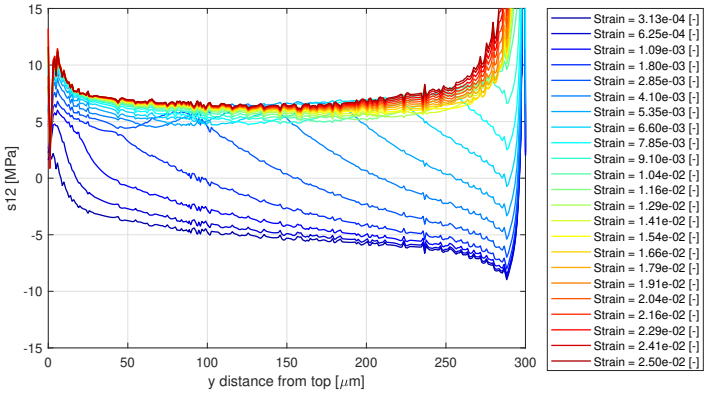


(c) Reloading Step

Figure 117: Broken Fibre Shear Stress Through Outer Path, 25% Packing, Cropped View

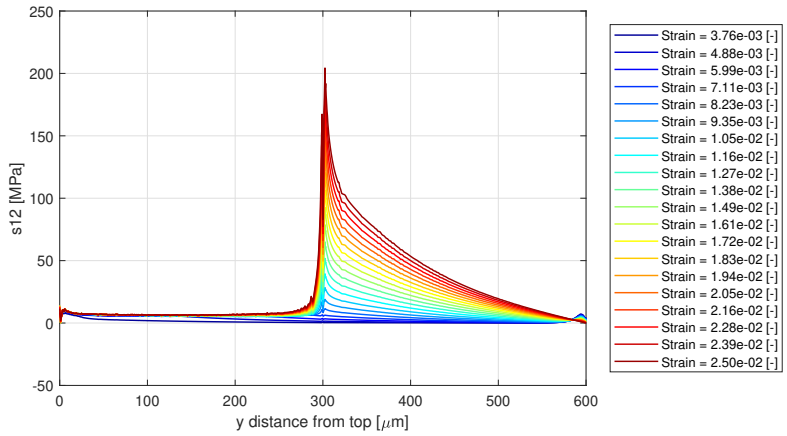


(a) Initial Loading Step

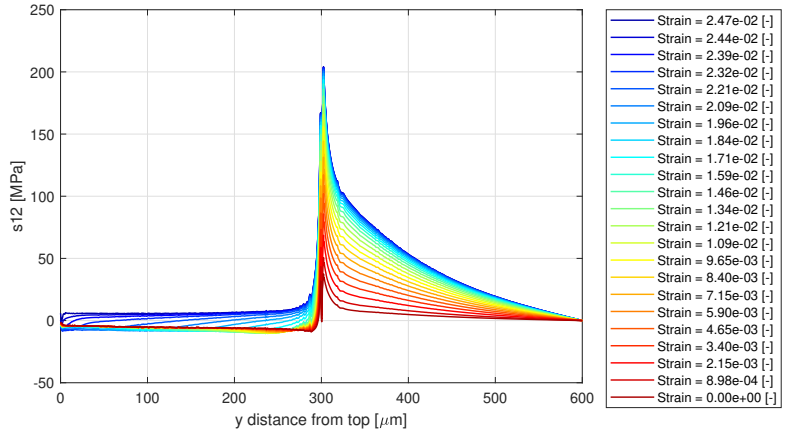


(b) Unloading Step

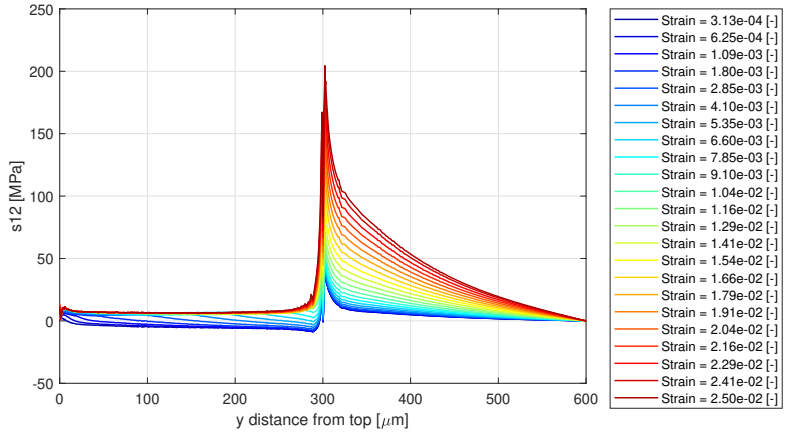


(c) Reloading Step

Figure 118: Broken Fibre Shear Stress Through Outer Path, 25% Packing, Full View

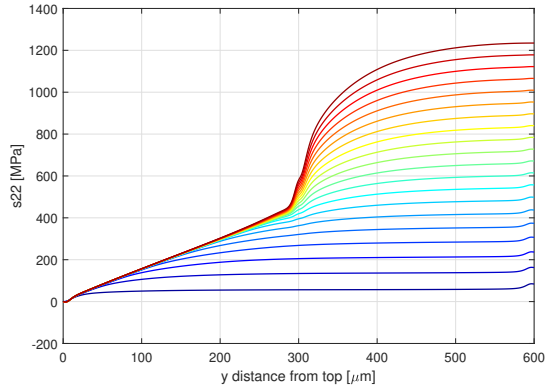


(a) Initial Loading Step

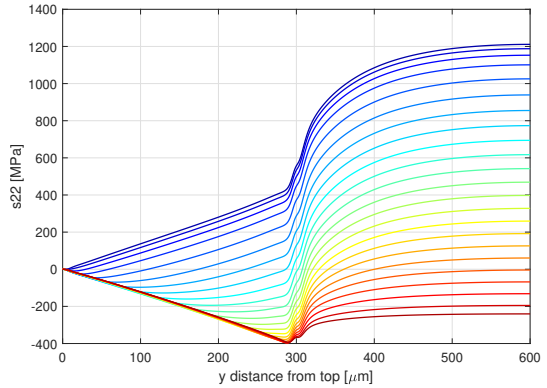


(b) Unloading Step

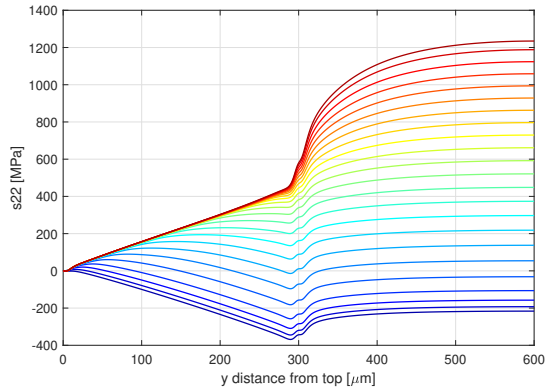


(c) Reloading Step

Figure 119: Broken Fibre S22 Through Centre Path, 25% Packing

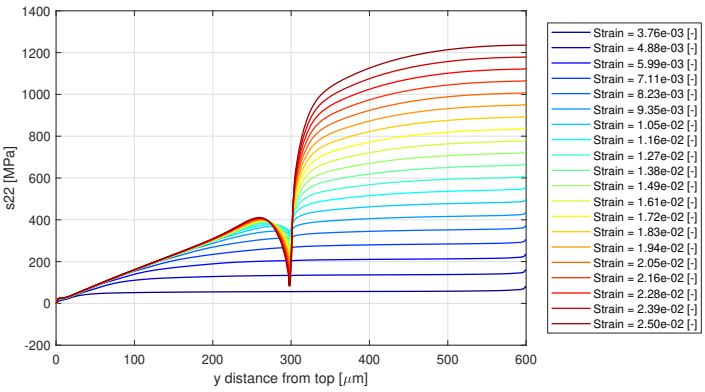


(a) Initial Loading Step

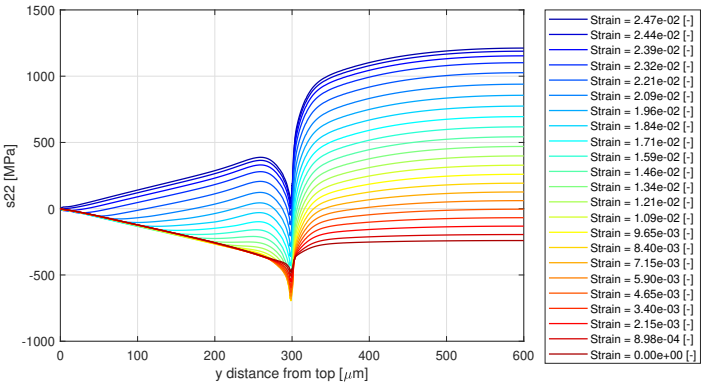


(b) Unloading Step

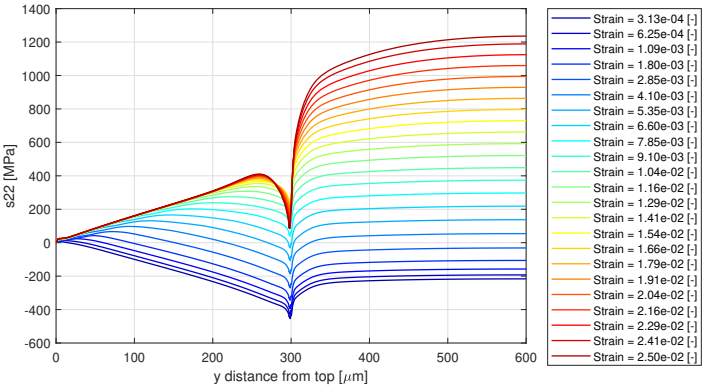


(c) Reloading Step

Figure 120: Broken Fibre S22 Through Outer Path, 25% Packing

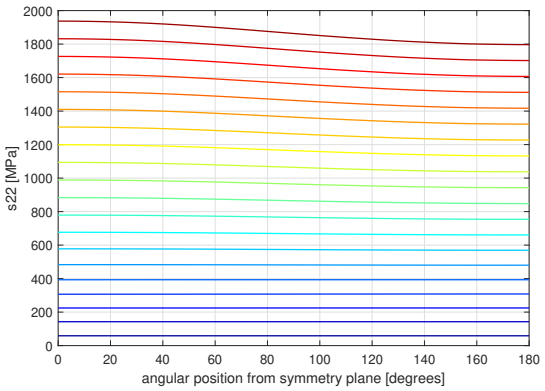


(a) Initial Loading Step

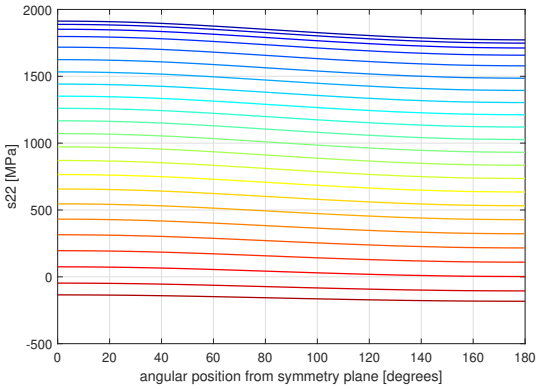


(b) Unloading Step

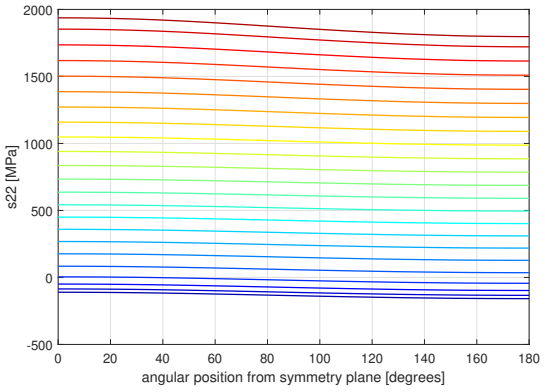


(c) Reloading Step

Figure 121: S22 Along Perimeter of Neighbouring Fibre Cross Section, 25% Packing

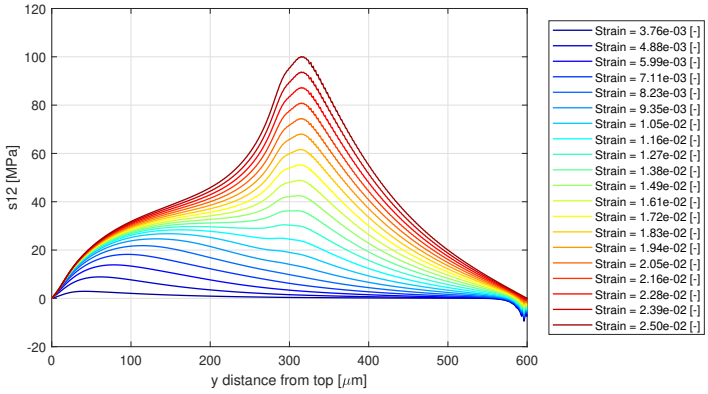


(a) Initial Loading Step

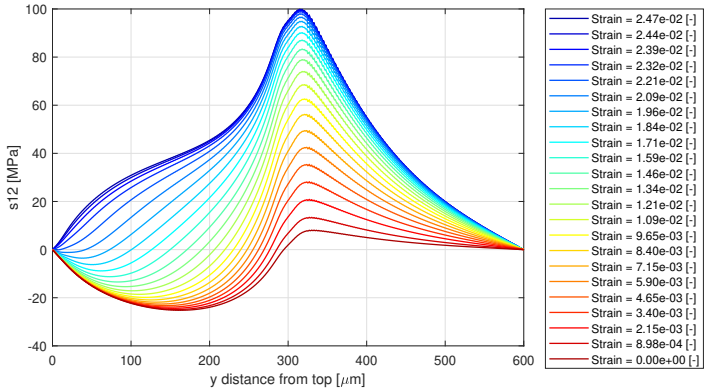


(b) Unloading Step

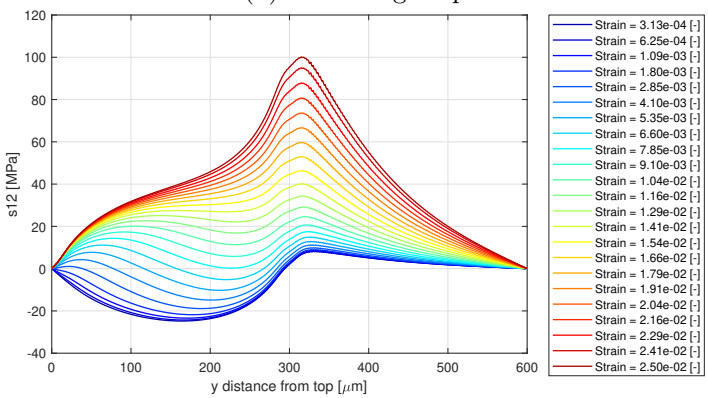


(c) Reloading Step

Figure 122: S12 at Surface of Neighbouring Fibre, 25% Packing

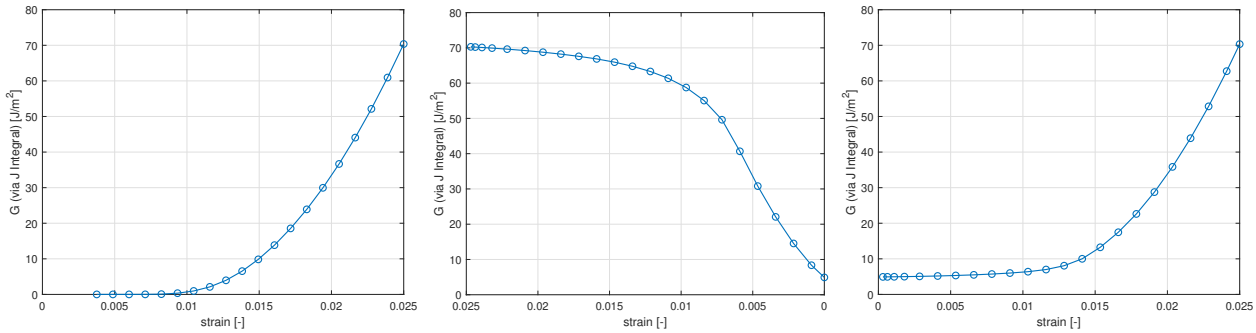


(a) Initial Loading Step (b) Unloading Step (c) Reloading Step

Figure 123: Energy Release Rate vs. Strain, 25% Packing

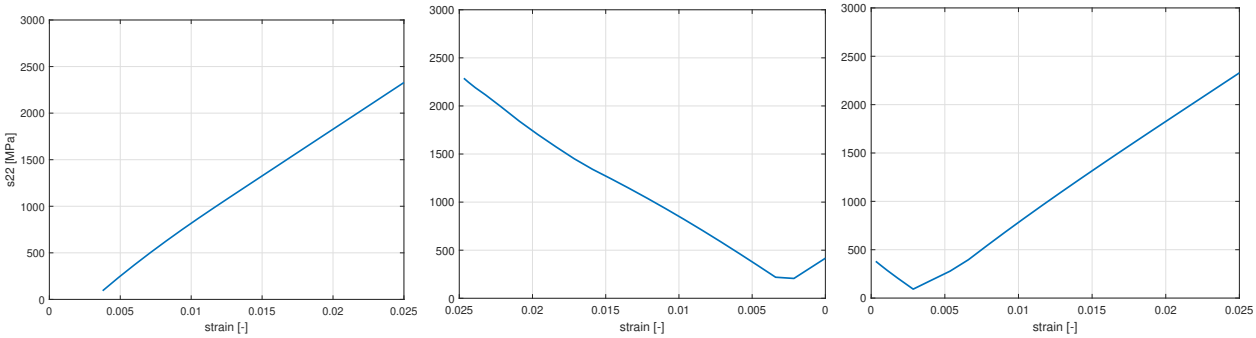


(a) Initial Loading Step (b) Unloading Step (c) Reloading Step

Figure 124: Max. S22 (Absolute Value) in Neighbouring Fibre vs. Strain, 25% Packing

## C.2 40% Packing

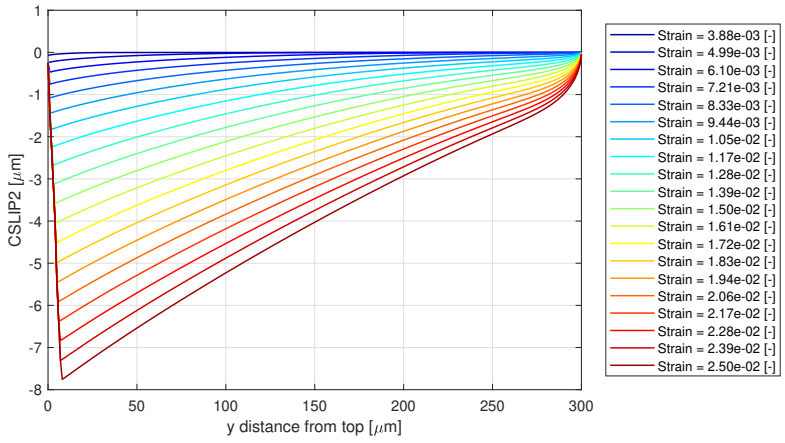


(a) Initial Loading Step

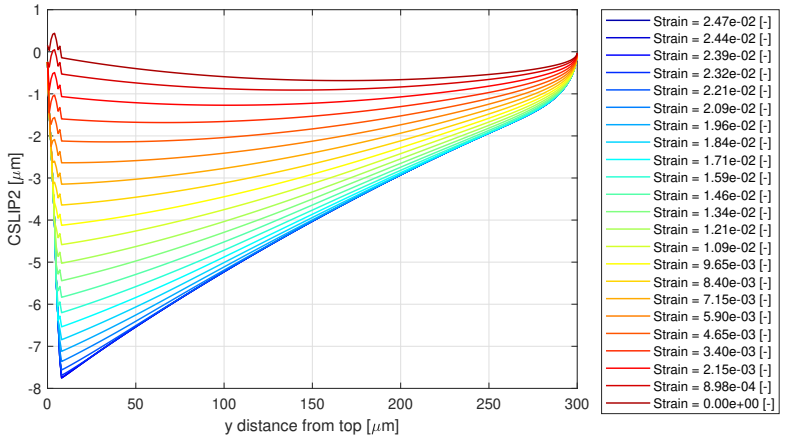


(b) Unloading Step

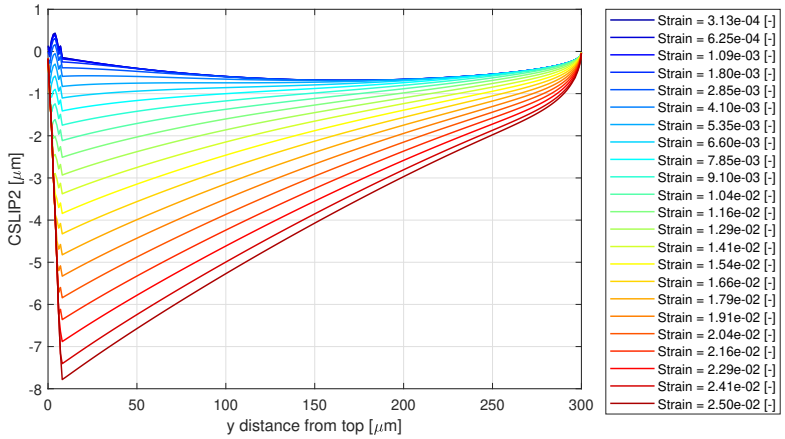


(c) Reloading Step

Figure 125: Interfacial Slipping Along Debond Interface, 40% Packing

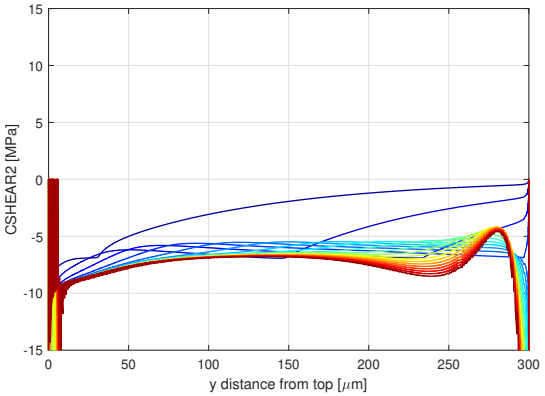


(a) Initial Loading Step

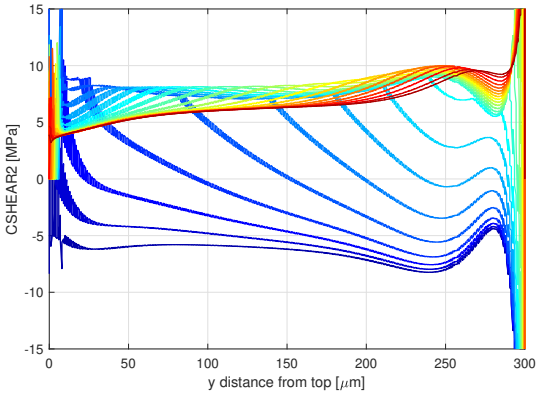


(b) Unloading Step

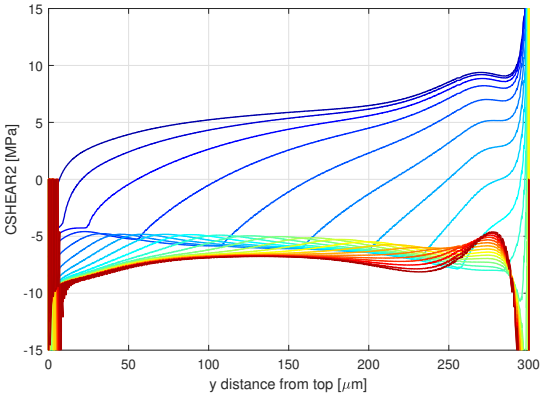


(c) Reloading Step

Figure 126: Shear Stress Along Debond Interface, 40% Packing

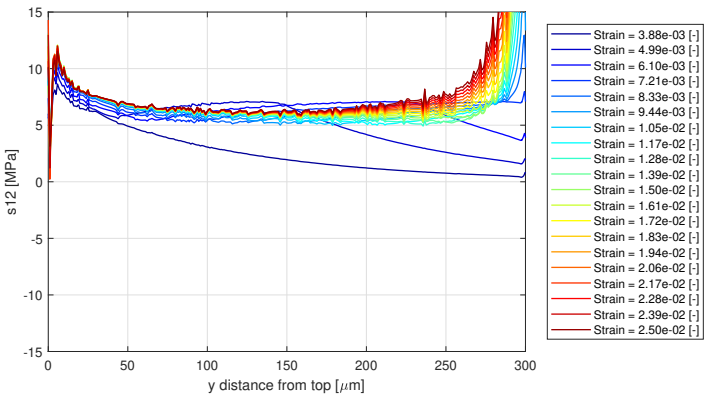


(a) Initial Loading Step

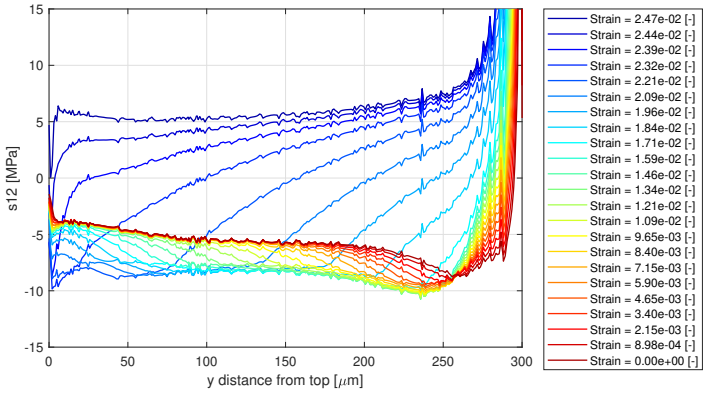


(b) Unloading Step

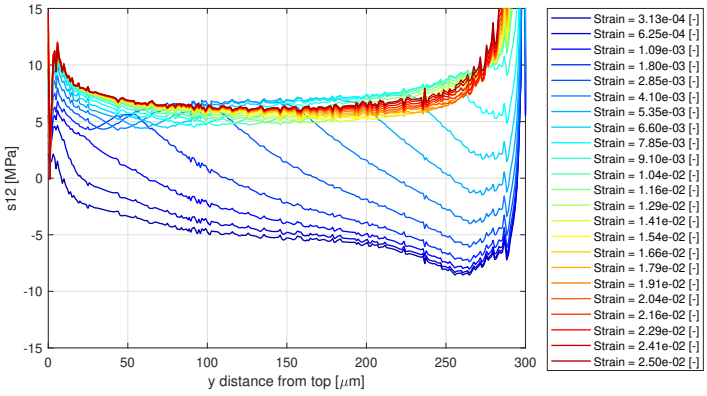


(c) Reloading Step

Figure 127: Broken Fibre Shear Stress Through Outer Path, 40% Packing, Cropped View

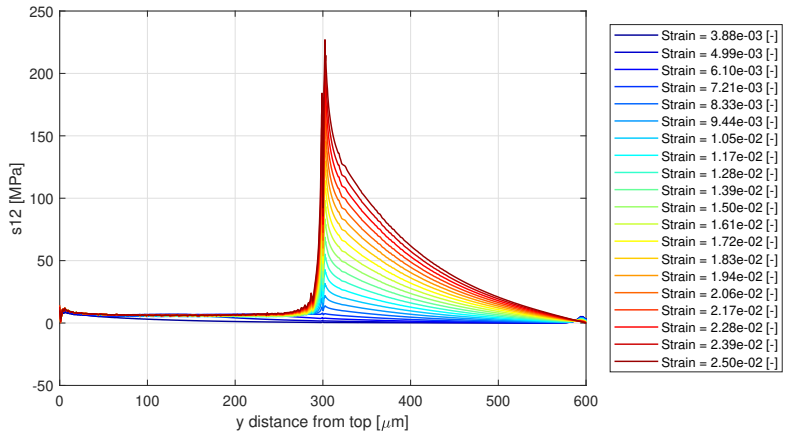


(a) Initial Loading Step

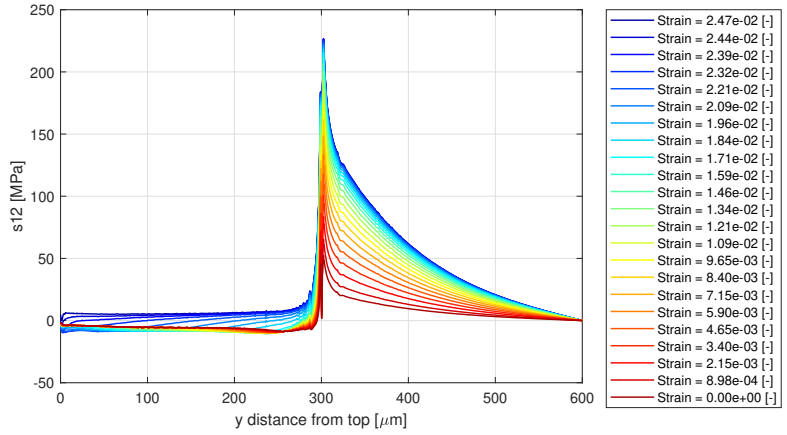


(b) Unloading Step

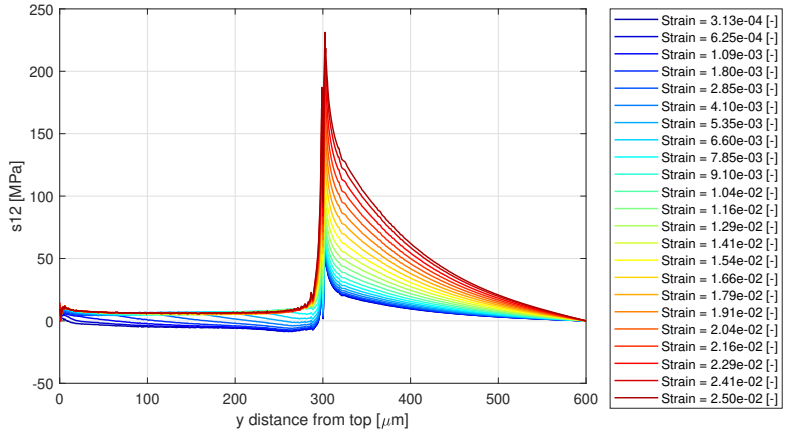


(c) Reloading Step

Figure 128: Broken Fibre Shear Stress Through Outer Path, 40% Packing, Full View

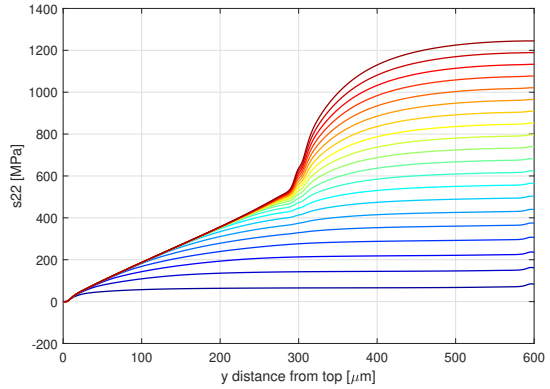


(a) Initial Loading Step

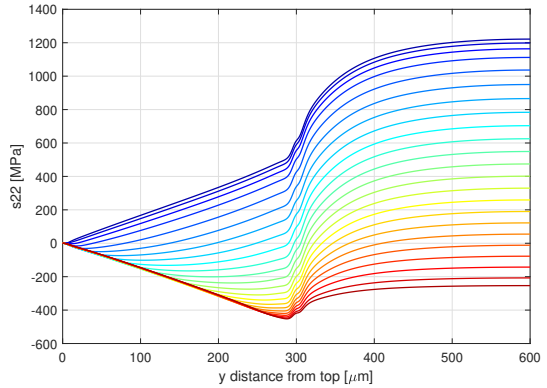


(b) Unloading Step

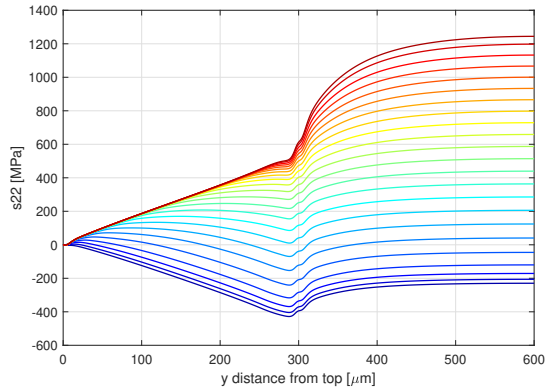


(c) Reloading Step

Figure 129: Broken Fibre S22 Through Centre Path, 40% Packing

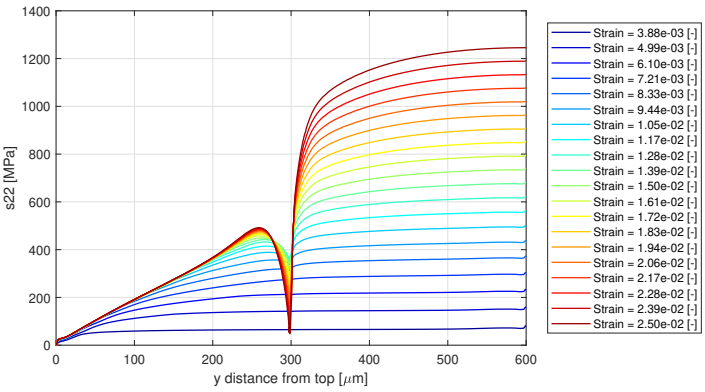


(a) Initial Loading Step

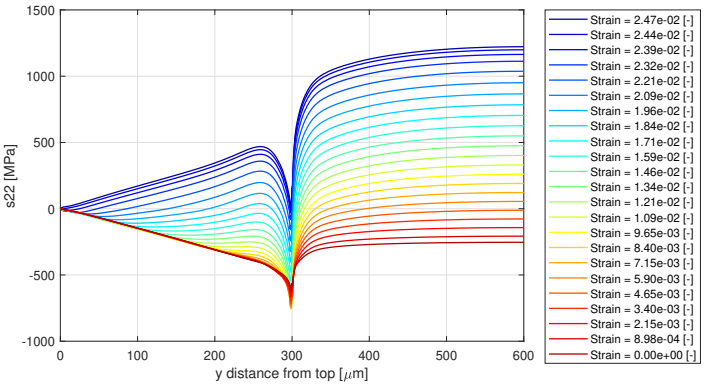


(b) Unloading Step

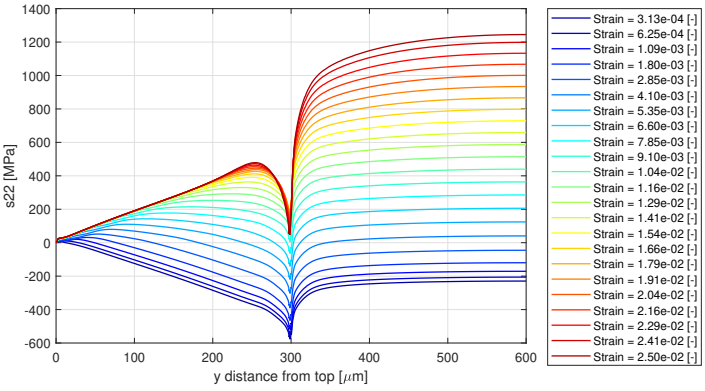


(c) Reloading Step

Figure 130: Broken Fibre S22 Through Outer Path, 40% Packing

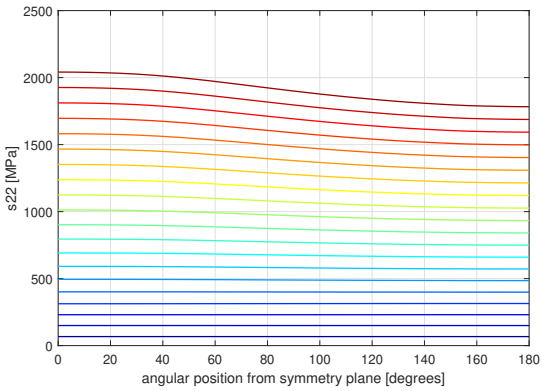


(a) Initial Loading Step

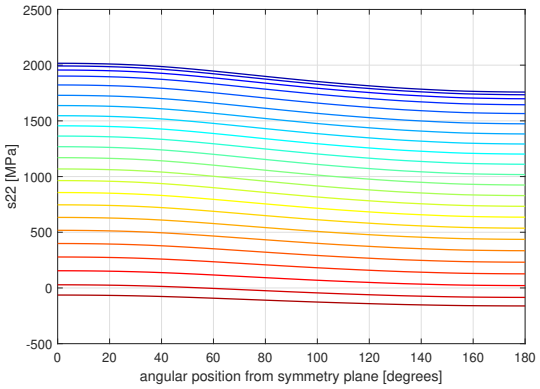


(b) Unloading Step

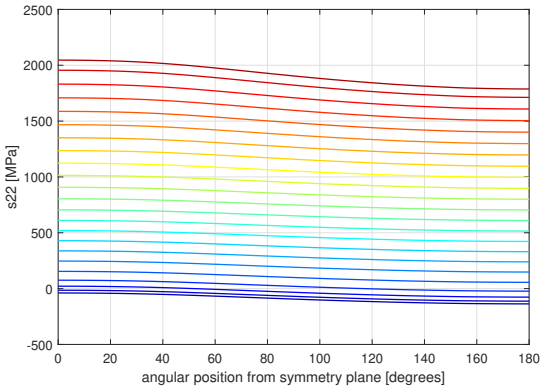


(c) Reloading Step

Figure 131: S22 Along Perimeter of Neighbouring Fibre Cross Section, 40% Packing

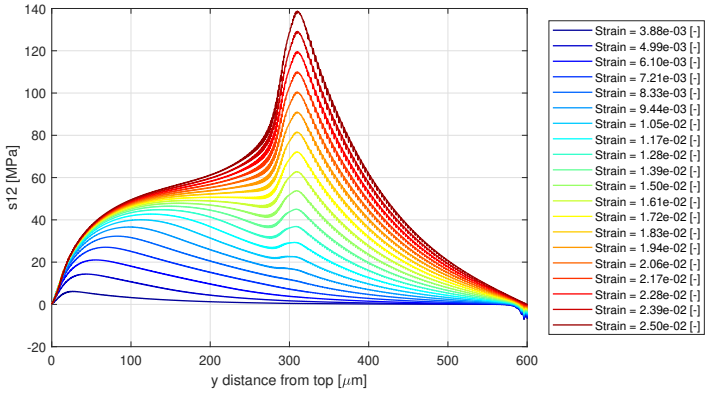


(a) Initial Loading Step

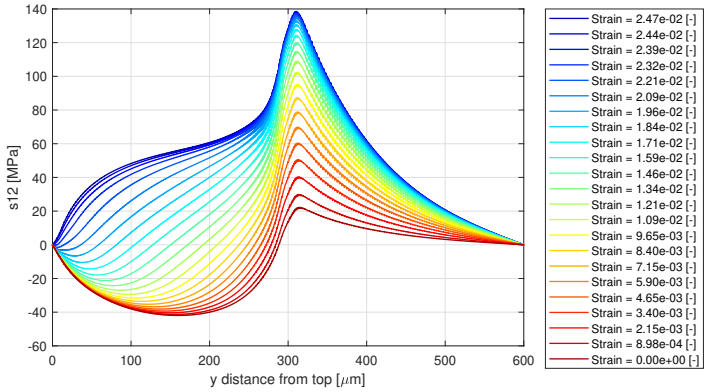


(b) Unloading Step

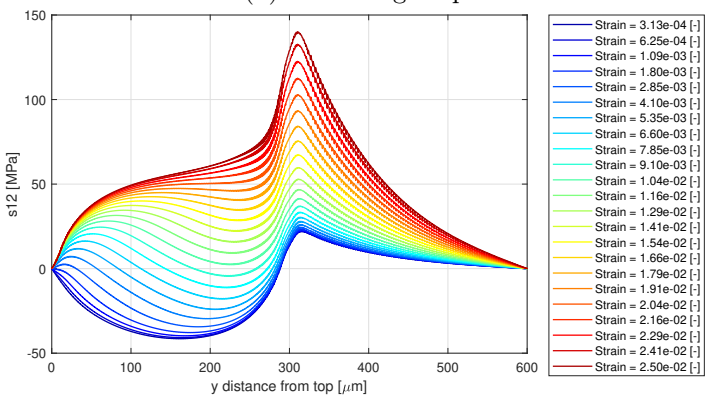


(c) Reloading Step

Figure 132: S12 at Surface of Neighbouring Fibre, 40% Packing

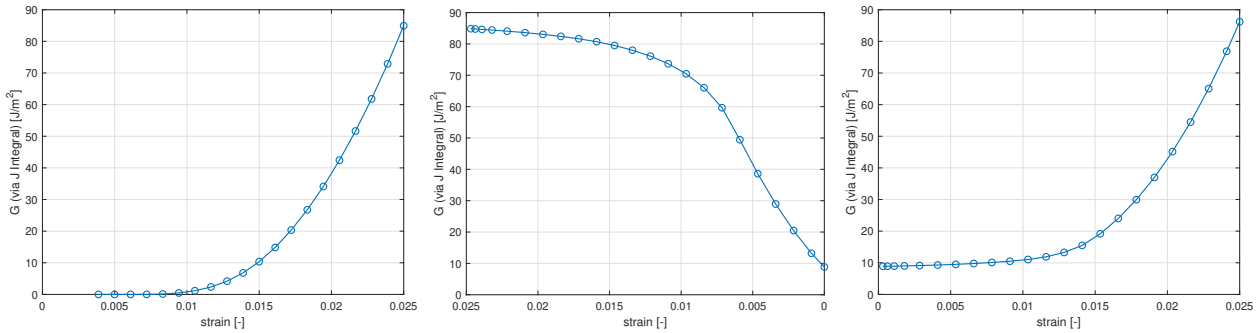


(a) Initial Loading Step (b) Unloading Step (c) Reloading Step

Figure 133: Energy Release Rate vs. Strain, 40% Packing

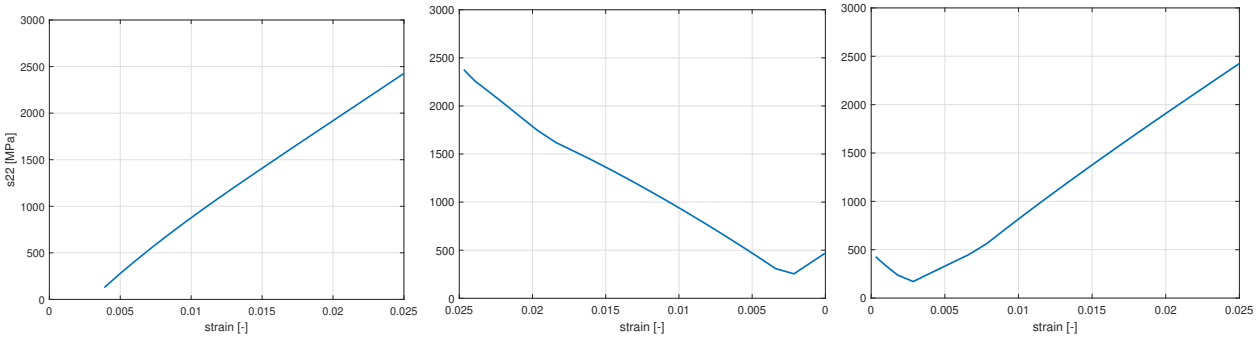


(a) Initial Loading Step (b) Unloading Step (c) Reloading Step

Figure 134: Max. S22 (Absolute Value) in Neighbouring Fibre vs. Strain, 40% Packing

## C.3 70% Packing

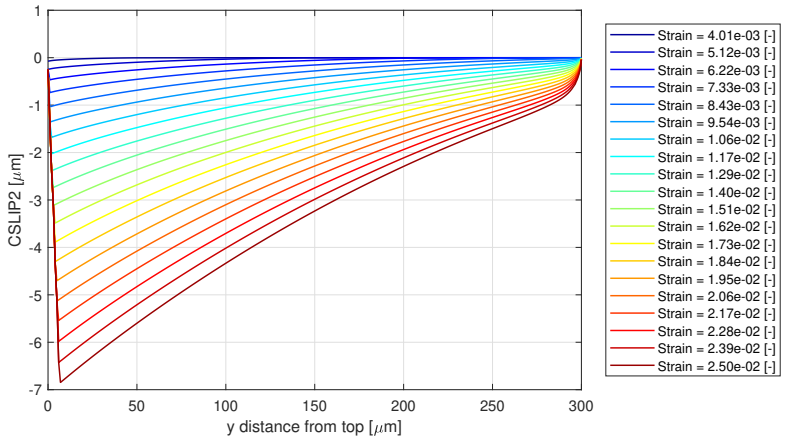


(a) Initial Loading Step

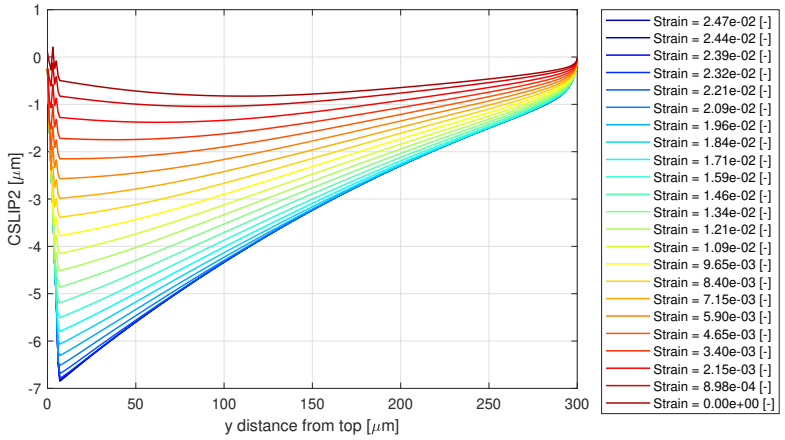


(b) Unloading Step

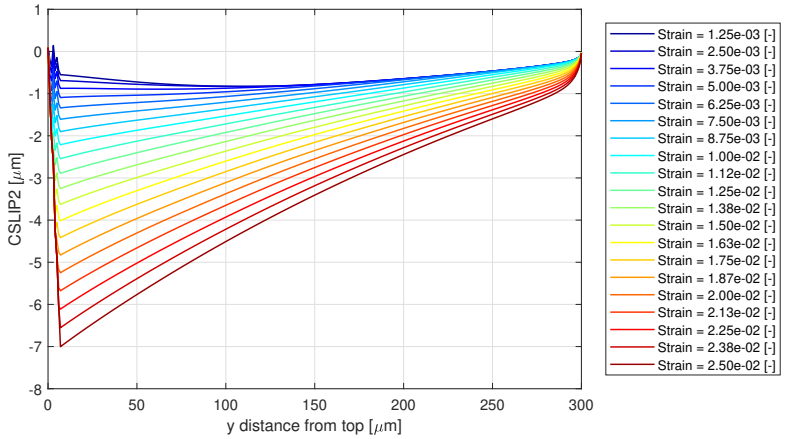


(c) Reloading Step

Figure 135: Interfacial Slipping Along Debond Interface, 70% Packing

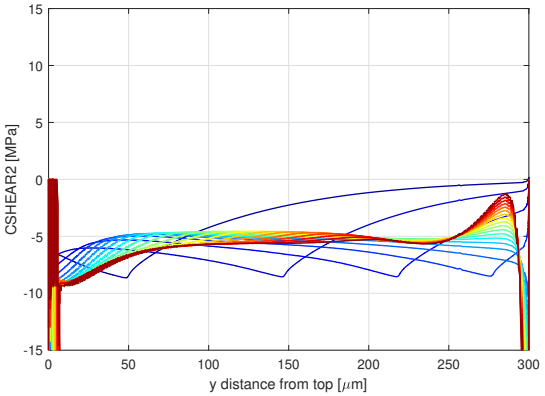


(a) Initial Loading Step

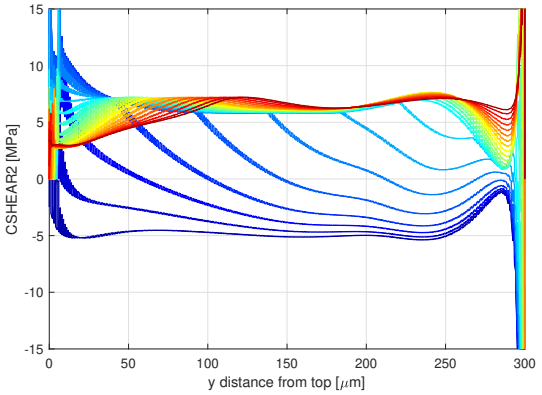


(b) Unloading Step

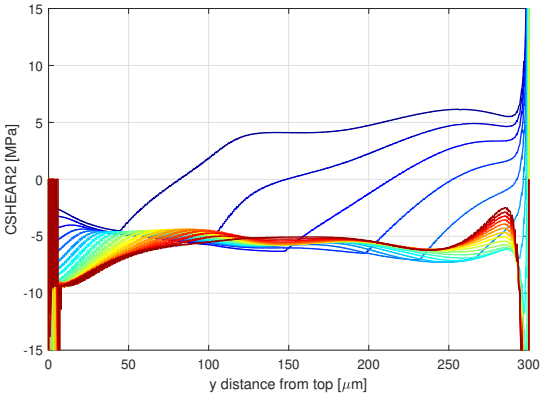


(c) Reloading Step

Figure 136: Shear Stress Along Debond Interface, 70% Packing

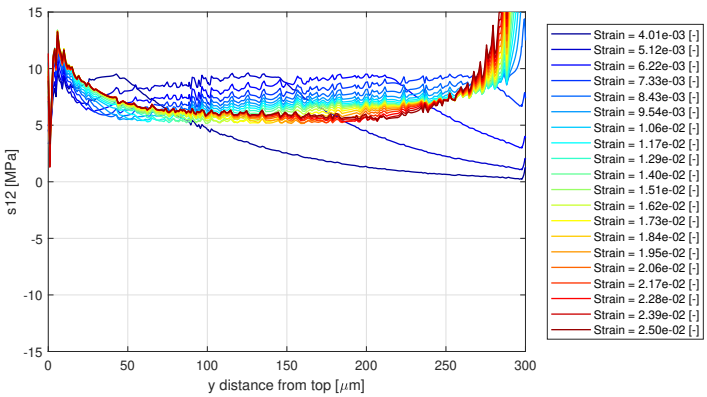


(a) Initial Loading Step

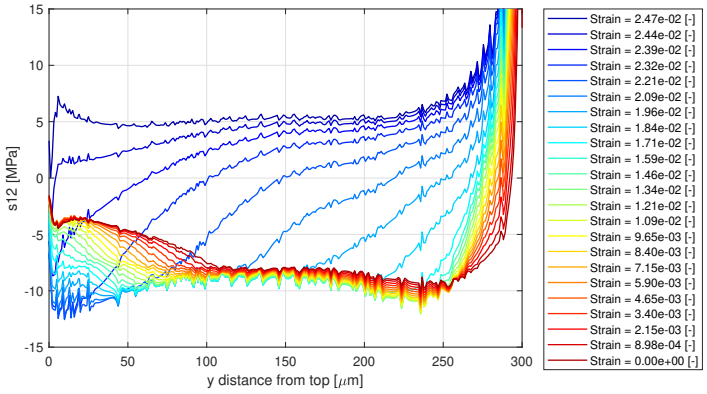


(b) Unloading Step

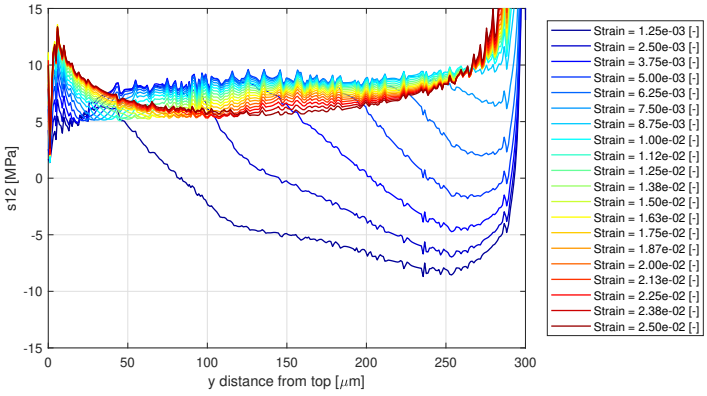


(c) Reloading Step

Figure 137: Broken Fibre Shear Stress Through Outer Path, 70% Packing, Cropped View

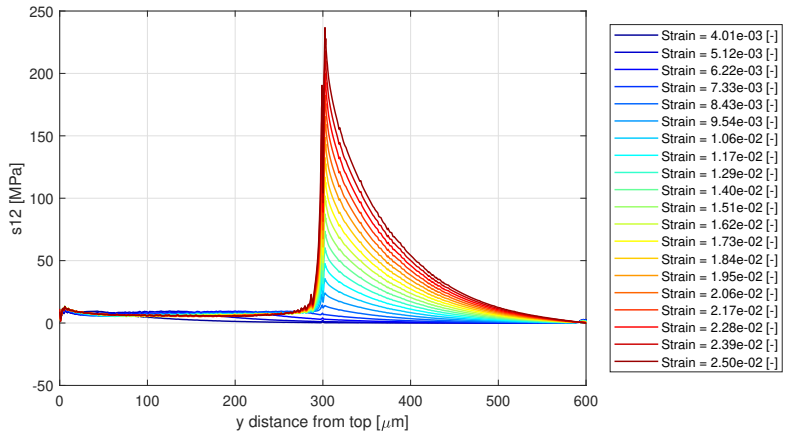


(a) Initial Loading Step

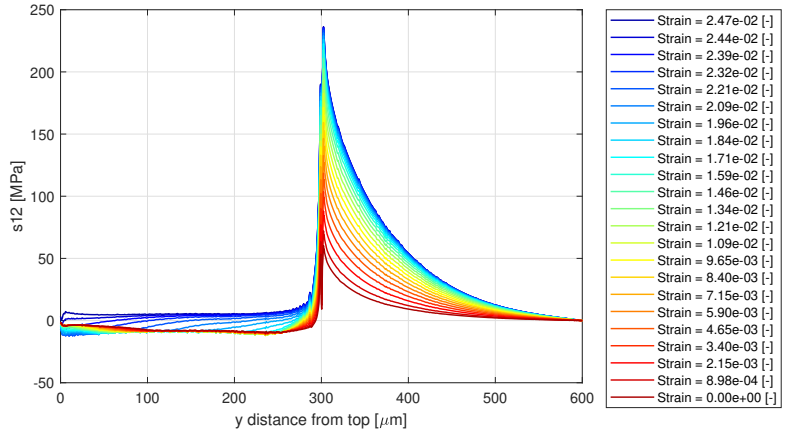


(b) Unloading Step

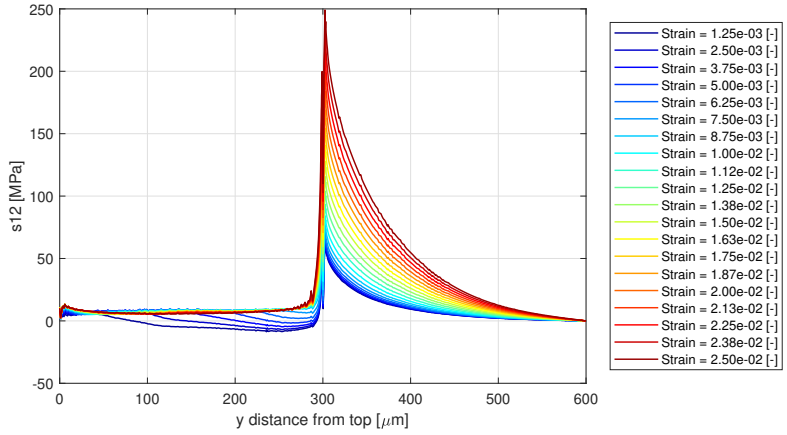


(c) Reloading Step

Figure 138: Broken Fibre Shear Stress Through Outer Path, 70% Packing, Full View

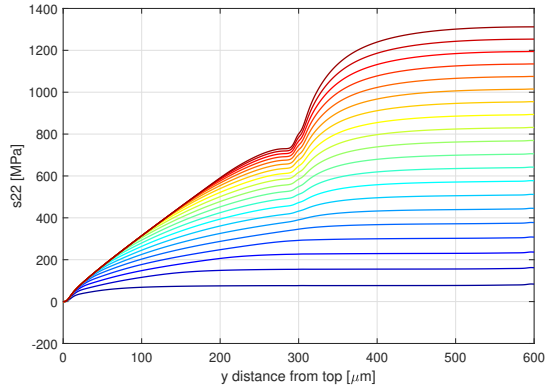


(a) Initial Loading Step

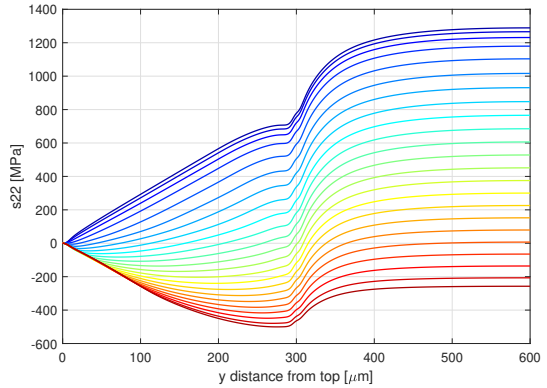


(b) Unloading Step

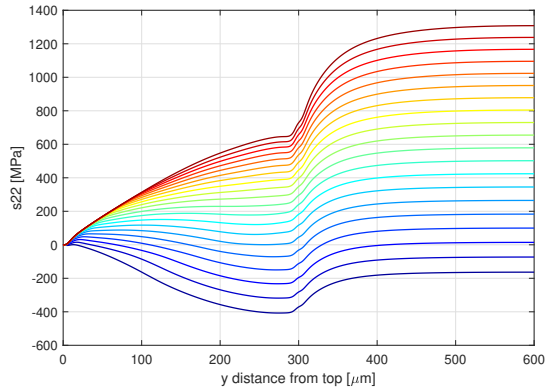


(c) Reloading Step

Figure 139: Broken Fibre S22 Through Centre Path, 70% Packing

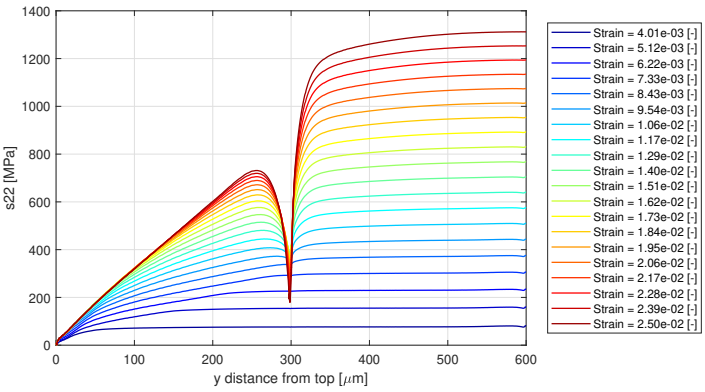


(a) Initial Loading Step

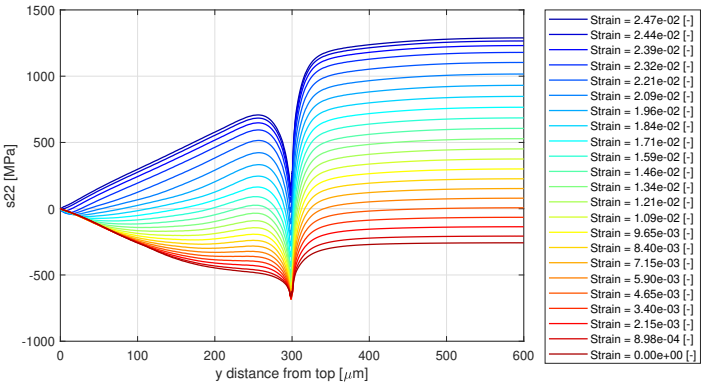


(b) Unloading Step

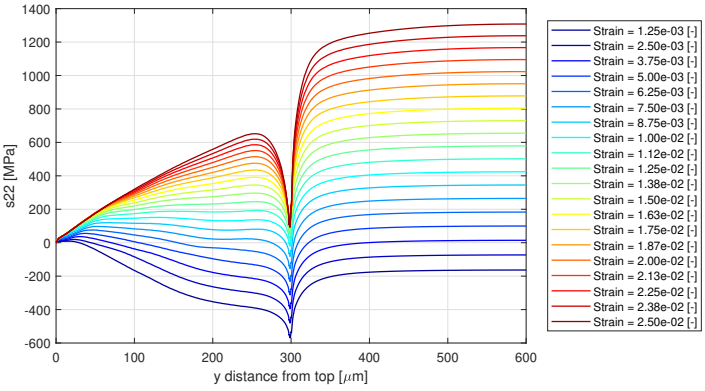


(c) Reloading Step

Figure 140: Broken Fibre S22 Through Outer Path, 70% Packing

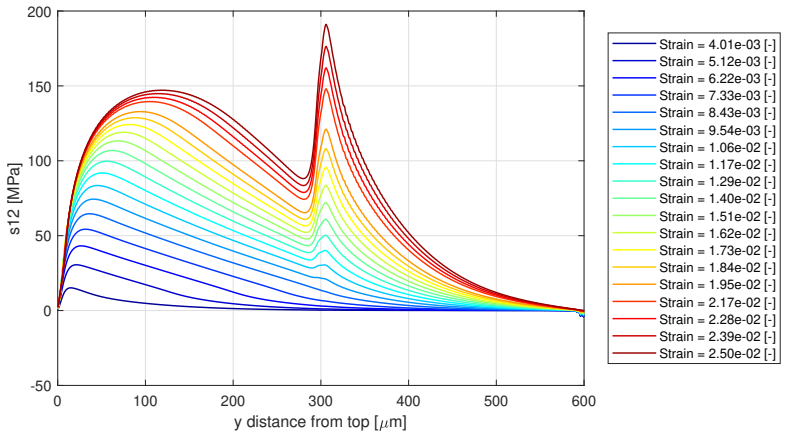


(a) Initial Loading Step

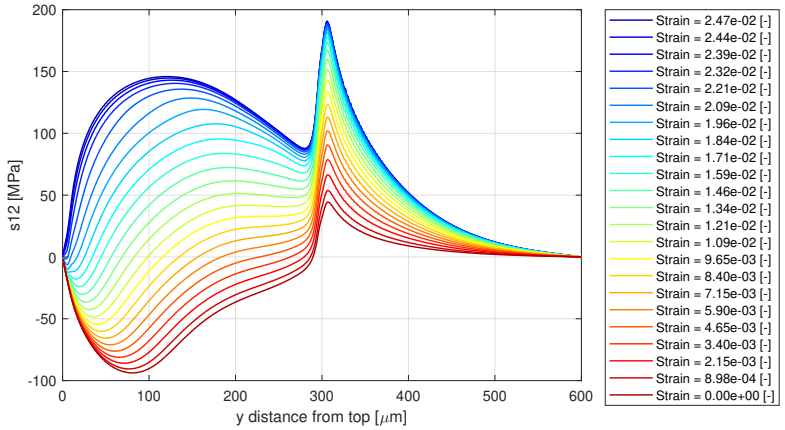


(b) Unloading Step

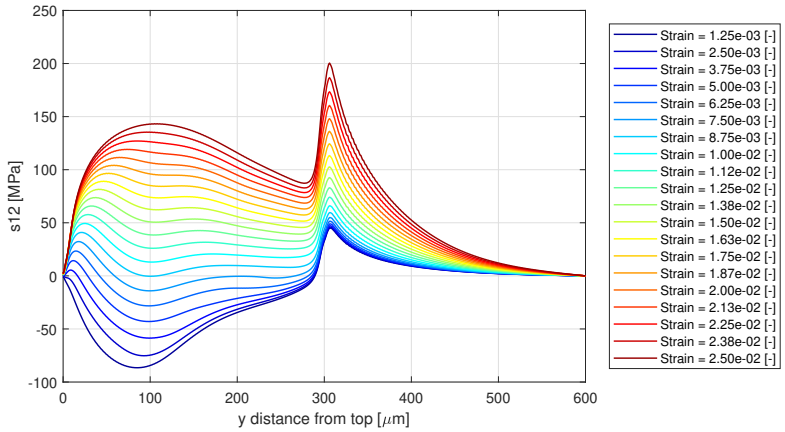


(c) Reloading Step

Figure 141: S12 at Surface of Neighbouring Fibre, 70% Packing

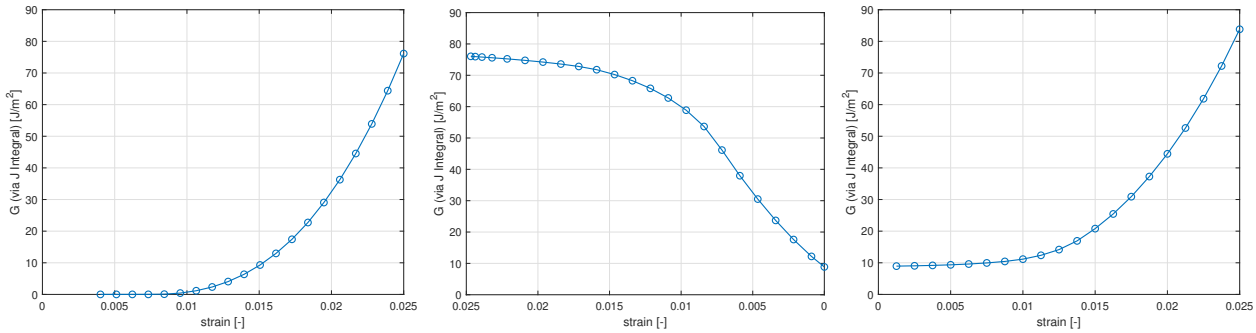


(a) Initial Loading Step (b) Unloading Step (c) Reloading Step

Figure 142: Energy Release Rate vs. Strain, 70% Packing

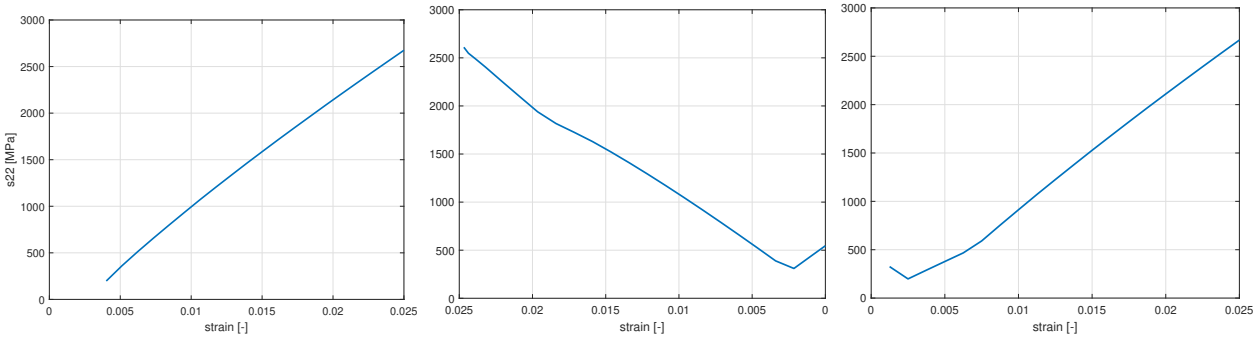


(a) Initial Loading Step (b) Unloading Step (c) Reloading Step

Figure 143: Max. S22 (Absolute Value) in Neighbouring Fibre vs. Strain, 70% Packing